Title
Elementary Steps in Aldol Condensation on Solid Acids: Insights from Experiments and Theory

Author
Herrmann, Stanley Thomas

Publication Date
2016

Peer reviewed|Thesis/dissertation

Elementary Steps in Aldol Condensation on Solid Acids: Insights from Experiments and Theory

by

Stanley Thomas Herrmann

A dissertation submitted in partial satisfaction of the
requirements for the degree of

Doctor of Philosophy

in

Chemical Engineering

in the

Graduate Division

of the

University of California, Berkeley

Committee in charge:

Professor Enrique Iglesia, Chair
Professor Alexander Katz
Professor T. Don Tilley

Summer 2016

Elementary Steps in Aldol Condensation on Solid Acids:
Insights from Experiments and Theory

by

Stanley Thomas Herrmann

Abstract

Elementary Steps in Aldol Condensation on Solid Acids:
Insights from Experiments and Theory

by

Stanley Thomas Herrmann

Doctor of Philosophy in Chemical Engineering

University of California, Berkeley

Professor Enrique Iglesia, Chair

The efficient conversion of oxygen-rich feedstocks derived from biomass to valuable chemicals and fuels requires an understanding of the oxygenate chemistry that can lengthen carbon chains and decrease oxygen content. Aldol condensation of alkanones and alkanals provides a pathway to form new C-C bonds, while also removing O-atoms as H_2O. In this study, condensation reactions are investigated experimentally, through spectroscopic, H/D isotopic, and kinetic measurements, in combination with theoretical treatments (density functional theory (DFT) and coupled cluster methods (CCSD)) for a diverse range of solid Brønsted acid catalysts. These acids include H-Al-FER, H-Al-TON, H-M-MFI (M = Al, Ga, Fe, or B at framework locations), H-Al-BEA, H-Al-FAU, and H-Al-MCM-41. Condensation rates on these solid acid catalysts decrease rapidly with time on stream as a result of secondary reactions of the quasi-equilibrated pool of unstable dimer intermediates, leading to the formation of large, unsaturated (C_{9+}) products that block active sites. A hydrogenation metal function, present as a separate component in physical (extracrystalline) mixtures or within the solid acids (intracrystalline), effectively scavenges these unsaturated species. In doing so, it (i) essentially eliminates deactivation; (ii) removes thermodynamic bottlenecks in C-C bond formation; (iii) avoids secondary β-scission reactions that decrease C-chain length; and (iv) allows rigorous mechanistic studies and the elucidation of the consequences of acid strength and confinement within zeolite voids on the kinetically-relevant rate constants and transition states.

The selective titration of protons by non-coordinating bases (2,6-di-*tert*-butyl-pyridine) during acetone condensation, together with infrared (IR) spectra also collected during acetone condensation, indicate that condensation reactions (453-483 K, 0.1-10 kPa acetone) occur on protons nearly saturated with H-bonded acetone without detectable contributions to condensation rates from Lewis acid sites. These results are consistent with DFT-simulated energies and frequencies of reaction intermediates and transition states (T12-site, Al-MFI unit cell, VASP, RPBE, D3BJ). Such theoretical treatments suggest strong acetone binding at reaction temperatures (ΔG = -80 kJ mol^{-1}, 473 K) present as H-bonded species and confirm the measured shift in the

infrared spectra of the acidic O-H stretch in zeolites upon addition of acetone (0.4 kPa acetone, 473 K) from 3600 cm^{-1} to 2440 cm^{-1}. Measured condensation turnover rates are proportional to acetone pressure on all samples, and the resulting first-order rate constant reflects the free energy differences between bimolecular C-C bond-formation transition states and protons saturated with H-bonded acetone and gaseous acetone. The kinetic relevance of C-C bond formation is consistent with the DFT-derived free energy barrier of this step, which lies at the highest value along the reaction coordinate at T12 sites in H-Al-MFI structures.

These first-order condensation rate constants can be compared on solid Brønsted acids with different acid strength and confining environments to determine their consequences on the stability of the kinetically-relevant transition states and their relevant precursors. The effects of acid strength are evident from comparisons among catalysts with different acid strength (Al-, Ga-, Fe-, B- framework heteroatoms) and similar void structure (MFI). Here, rate constants increase exponentially with decreasing deprotonation energy (DPE), a theoretically-accessible measure of catalyst acid strength. These measured effects of acid strength on rate constants reflect the stability of the conjugate anion, which influences the stability of the ion-pair transition states more strongly than for the less charged H-bonded acetone precursors.

Microporous aluminosilicates with different framework structures provide protons of similar local composition and local coordination (acid strength), but very diverse confining void environments. Measured condensation rate constants reach a maximum value for voids similar in size to the C-C bond formation transition states (MFI, BEA); these frameworks contain voids that preferentially stabilize these transition states over smaller H-bonded acetone precursors through van der Waals interactions. The relative size and shape of these species and their strong effects on reactivity require theoretical methods that accurately account for attractive dispersion forces in energy minimizations and that can assess, posteriori, the quantum mechanical and dispersion components of DFT-derived Gibbs free energies (VASP, RPBE + D3(BJ)). These treatments are supplemented by computational screening methods developed here, which use Lennard-Jones potentials to determine interaction energies between each framework oxygen atom and all atoms in the organic moieties, thus rigorously capturing the consequences of both the size and the shape of the relevant organic moieties and the inorganic frameworks surrounding the proton. These interaction energies are then ensemble-averaged for each transition state and precursor species over all crystallographically-distinct proton locations within each microporous framework. The resulting energies act as rigorous descriptors of the "fit" for the kinetically-relevant species in a manner that accounts for the most favorable placement of all structures within the accessible confining void environments. These descriptors extend those based only on the independent properties of the species (proton affinities) and the catalyst (DPE) and their ability to reorganize charge to include parameters that describe how organic and inorganic components in transition state and precursors interact, which depends on the size and shape of both the organic and the inorganic moieties.

We have also addressed the enduring challenge of deactivation and secondary reactions that break C-C bonds in metal-free solid acids. All solid acids show significant selectivities to isobutene (C_4) and acetic acid (formed in equimolar amounts), which form via β-scission of the species from the quasi-equilibrated C_6-product pool (diacetone alcohol, mesityl oxide, and isomesityl oxide, for acetone reactants). These secondary reactions depend strongly on the size of

the void environment and are most effectively catalyzed in MFI. These reactions require the presence of protons (mesityl oxide/isomesityl oxide/H_2O mixtures do not react on Si-MFI (SIL-1)), but β-scission selectivities at a given acetone conversion increase sharply as Al (and proton) densities decrease, even though acetone condensation turnover rates remained unchanged. These counterintuitive trends, where lower densities of the purported active sites preferentially enhance secondary reactions, cannot reflect diffusional constraints and require the concurrent presence of protons and a vicinal confining environment that, even without active sites, can convert highly reactive intermediates into more stable β-scission products. A detailed examination of the effects of H_2O, which determines the relative concentrations of mesityl oxide/isomesityl oxide and their ketol precursors, shows that two β-scission routes with different site requirements are involved. One route involves the β-scission of ketol species (diacetone alcohol); it occurs on all zeolites and is exclusively catalyzed by protons. A second and previously unrecognized route involves β-scission events of mesityl oxide/isomesityl oxide or their tautomer C_6-alkenol products. These pathways involve the formation of an initial product on protons and its subsequent reaction within vicinal confined spaces that provide stabilization for chain propagation transition states, even in the absence of a proton. In this manner, β-scission rates become proportional to both the number of initiation sites (protons) and of propagating locations (voids), a dependence that cannot be described by conventional bifunctional catalytic formalisms. Such physical catalysis by voids free of active sites was recently shown to account for the reactivity of pure-silica zeolites in reactions of molecules with radical character; its plausible involvement here is consistent with coupled cluster (CCSD) calculations of the free energy of formation of potential chain initiators and radical propagators from mesityl oxide/isomesityl oxide and their C_6-alkenol analogs.

Dedication

I dedicate this dissertation to my brothers: Stephen and Stuart.

The past five years have been filled with ups and downs for me, but all along the way I always knew that I had my two best friends there if I needed them. They have kept me grounded and motivated to be the best person I could be, whether it was in a swimming pool, at a scouting camp, or in a classroom.

I love you guys.

Table of Contents

Acknowledgements

I would like to thank Professor Enrique Iglesia for his persistence, patience, and passion in understanding any problem, for teaching me how to become a better problem-solver (in and out of the laboratory), and for creating a culture in his research group where everyone strives for excellence but not at the cost of others. My time in the Iglesia group has been a wonderful experience where I have grown as a scientist and a person. I would like to thank all of the Iglesia group members over the past 5 years: the members that were here when I arrived, who were willing to show me the ropes and give me something to aspire to become (Raj Gounder, Brett Loveless, Rob Carr, Dave Flaherty, and Andrew Jones); those that have been here with me enjoying the ride (Will Knaeble, Allie Landry, Michele Sarazen, Gina Noh, David Hibbitts, and Elif Gurbuz); and the new members who have brought energy and curiosity back to a jaded 5th year graduate student (Sam Leung, Haefa Mansour, Ari Fischer, and Marianne Sleiman). I would especially like to thank Michele Sarazen; without her help in every aspect of my research, I would not be where I am today.

My family has been an amazing support structure for me along this journey providing me company in the form of phone calls on my walks to and from lab and allowing me to end the conversation once I got to my destination, planning escapes to east coast beaches in the summer where I could take long walks with Pops and forget about my research for a few precious days, and flying across the country to see where I live and explore California. They have made the 2500 miles between us seem small (so small that I am not ready to leave California yet!).

I was also lucky enough to find my other half; a person that brings out my adventurous side, a person that has a way of making me excited for everything (even running), and a person that I could not imagine being without—Allie Landry. After we met 1st year, I could rest assured knowing that if all else failed in graduate school I would still have her by my side. I cannot wait to see where life takes us!

Chapter 1

Introduction to Aldol Condensation on Solid Brønsted Acid Catalysts

Efficient conversion of oxygen-rich, biomass-derived molecules to valuable chemicals and fuels requires an understanding of oxygenate chemistry to increase energy density and decrease oxygen content [1]. Aldol condensation provides such reaction pathways by forming of a carbon-carbon bond between two carbonyl-containing molecules and removing oxygen via subsequent dehydration of aldol intermediates (Scheme 1). Condensation reactions have been studied since the late 19th century on liquid acids and bases [2, 3]. Heterogeneous catalysts are better suited for industrial applications offering economic and ecological advantages such as catalyst separation and reusability. Aldol condensations have been reported on a range of heterogeneous catalysts including metal oxides [4-6], metals [7], and solid acid catalysts [8, 9]. Solid acids catalysts are of particular interest because of their ability to catalyze two key steps in aldol condensations: carbon-carbon bond formation and dehydration.

Scheme 1: Aldol condensation reaction pathways (-R_i = C_nH_{2n+1}(alkyl) or H, i = 1-4).

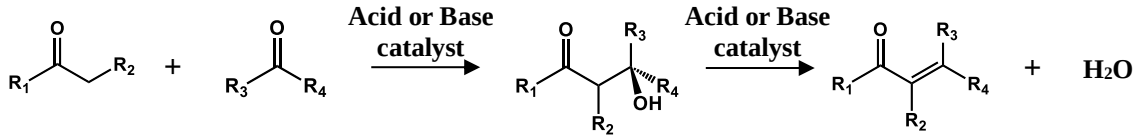

Solid Brønsted acid catalysts, specifically zeolites, are used as model catalysts to study these reactions [10, 11]. Zeolites are microporous, solid Brønsted acids with a known crystal structure [12]. The crystalline framework of these materials is composed of tetrahedrally-coordinated $[SiO_4]^{4-}$ containing microporous voids (channels, intersections, and cages) of molecular dimension ($\leq$ 1 nm); such voids allow the diffusion of molecules in one-, two-, or three dimensions of the framework depending on void connectivity [13]. Brønsted acid sites are introduced to zeolite frameworks during synthesis by isomorphous substitution of trivalent M-atoms (M^{3+}; M = Al, Fe, Ga, B) for tetravalent Si-atoms. The resulting charge imbalance is compensated by a proton (H^+), which form the Brønsted acid site (acid function, Scheme 2). Active protons in solid acid catalysts are characterized by two intrinsic properties: acid strength and confinement. The acid strength of a proton depends on the stability of its conjugate anion, which is dictated by the composition and local coordination of the acid site. All Brønsted acid sites in zeolites have similar local coordination (acid function, Scheme 2), and thus, the acid strength of the proton depends only on the chemical composition of the acid site, specifically the identity of the trivalent metal atom [14, 15]. Confinement, the effects of the void environment surrounding the proton, confers unique reactivity and selectivity to the proton by preferentially stabilizing transition states or intermediates based on their size and shape of the species and how it fits in the void [16]. The molecular size of zeolite channels, also, restrict the molecules that can diffuse through the zeolite framework to active protons based on the size of the molecules. The effects of acid strength and confinement on acid-catalyzed aldol condensation have not been discussed in the literature and are one of the key focuses of this work.

Solid acids also catalyze undesirable reactions of the aldol condensation products (secondary reactions, Scheme 2): (1) condensations to larger unsaturated products (1,3,5-trimethylbenzene), which are precursors to catalyst deactivation [11, 17]; and (2) β-scission to isobutene and acetic acid, which decreases the length of the carbon backbone [18]. This unselective nature of Brønsted acid catalysts has limited the research and industrial application of aldol condensation on solid acids. Several stabilization strategies for aldol condensation on zeolites have been discussed previously in the literature including: decreasing the size of the zeolite crystal size [19], introducing hydrogenation pathways via ion-exchange of Pt into the zeolite crystals [20, 21], or a combination of both techniques [22]. All of these strategies aim to minimize the extent of secondary reactions of C_6 species. The first strategy decreases the distance required to egress from the zeolite crystal; this does not, however, preclude reactions in subsequent zeolite crystals in the catalyst bed, which is apparent from rapid deactivation of even nano-scale zeolite crystals (30 nm) [23]. Addition of a hydrogenation function decreases the concentration of reactive C_6 intermediate by converting them into stable alkanones (methyl isobutyl ketone, Scheme 2), but applications of this method have not yielded a stable catalyst due attempts to limit the hydrogenation of the reactant by using low H_2 pressures (1:3 H_2:acetone molar ratios) [20, 21]. Here, we used this method of adding a hydrogenation function to perform a rigorous mechanistic study of aldol condensation on solid acid catalysts (Chapter 2); we used Pt and excess H_2 (10:1 H_2:acetone molar ratios) to scavenge the reactive C_6 intermediates (Scheme 2) stabilizing condensation rates where they are confidently extrapolated to initial time on stream. Such measurements and analysis treatments at low acetone conversion (< 5%) provide assessments the intrinsic reactivity of protons in each zeolite sample.

In this work (Chapter 2), we use a combination of kinetic, spectroscopic, and isotopic experiments together with theoretical assessments (density functional theory (DFT), Vienna Ab initio Simulation Package (VASP)) to investigate the elementary steps of acetone condensation and assess the kinetic relevance of these steps in developing an understanding of the mechanism on solid acids. We use samples of different acid strength (Al-, Fe-, Ga-, B-MFI isomorphously-substituted samples) and of different void environments (FER, TON, MFI, BEA, FAU, MCM-41; Scheme 3) to elucidate the catalytic consequences of key solid acid properties, acid strength and confinement. These solid acids were stabilized by the addition of hydrogenation pathways, feeding H_2 and adding Pt as physical mixtures of supported catalysts (Pt/SiO_2) or ion-exchanged into zeolite pores, shown in Scheme 2. The stability brought forth by this hydrogenation function allows rigorous mechanistic investigation of aldol condensation on these solid acids including site determination via selectivity titration with a non-coordinating base (2,6-di-*tert*-butyl-pyridine), pressure and temperature dependencies of the condensation rate. Rigorous mechanistic analysis and chemical interpretation of measured rates allows comparisons between experiments measurements and theoretical calculations, where quantum mechanical calculations of enthalpies combine with statistical mechanical treatments of entropies provide estimations of Gibbs free energy barriers.

Scheme 2: Approach for increasing stability and selectivity to C_6 products on solid acid catalysts for acetone condensation reaction by adding hydrogenation pathways*

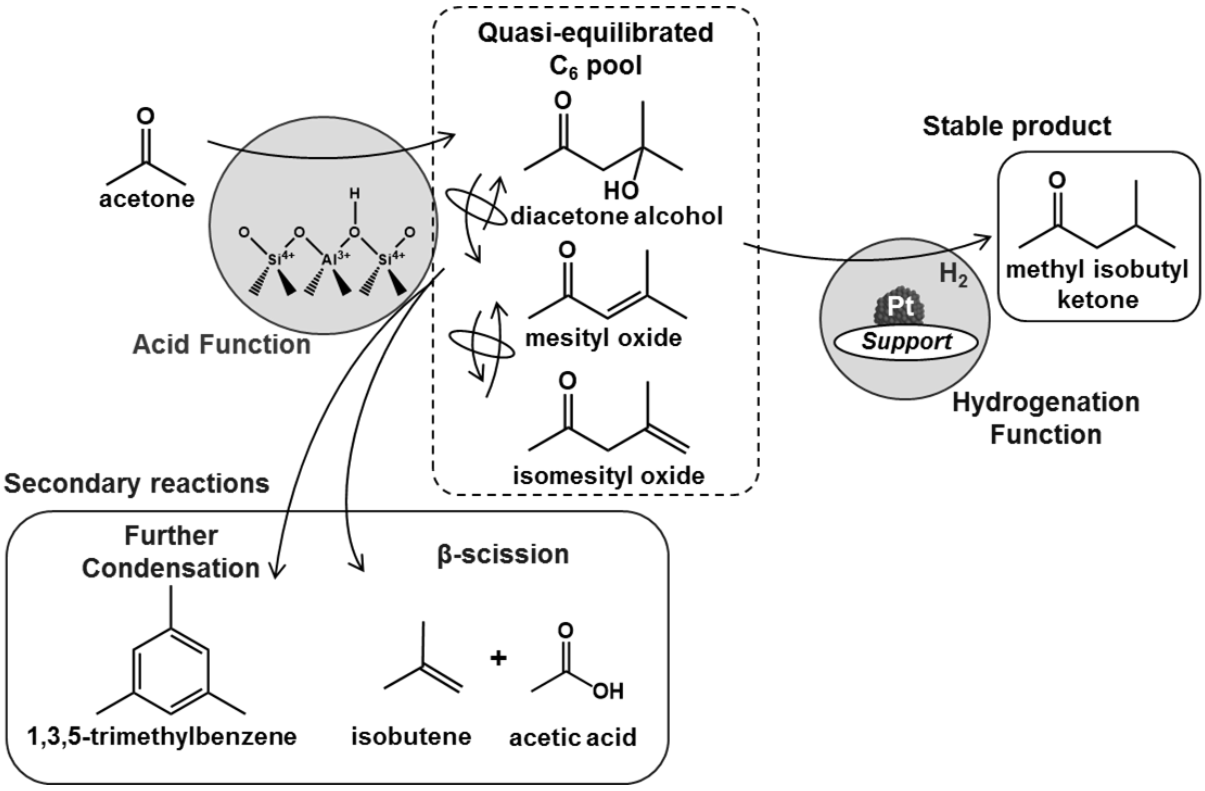

*Quasi-equilibrated steps are indicated by a circle over the double arrows.

The mechanistic interpretations of measured reactivities, established here, and theoretical simulations which account for dispersive interactions between the organic moiety (intermediates and transition states) and the inorganic framework, established previously [24, 25], provided the necessary tools for the development of a method to quantify the effects of confinement on measured reactivities (Chapter 2). Here, we built on methods previously proposed to quantify interactions between the O-atoms of the framework and the relevant organic moieties [16]. We develop an algorithm to sample configurations of the organic moiety at each distinct location in the zeolite crystal (unique T-sites) and use two-atom Lennard-Jones potentials to quantify the fit of the organic moiety as a van der Waals stabilization energy. Benchmarking these calculations against current techniques to estimate dispersive interactions demonstrates the effectiveness of the method developed which, which is much more efficient because this method does not require full DFT-simulations. Measured reactivities trend exponentially with calculated van der Waals stabilization energies, which is expected from rate constants that depend exponentially on free energy barriers. These van der Waals stabilization energies provide insight into the stabilities of transition states and precursors in zeolite voids, which can be leveraged to chosen a known zeolite framework that better stabilizes the transition state and thus has increased reactivity. The method developed here can also be used for any acid catalyzed reaction where the structures of the transition state(s) and precursor(s) are known.

Scheme 3: Pore-limiting diameter (darker gray) and largest cavity diameter (lighter gray) accessible to acetone in aluminosilicate frameworks [26]. Schematic depictions represent the framework channels and their intersections portraying the void environment surrounding protons in these frameworks.

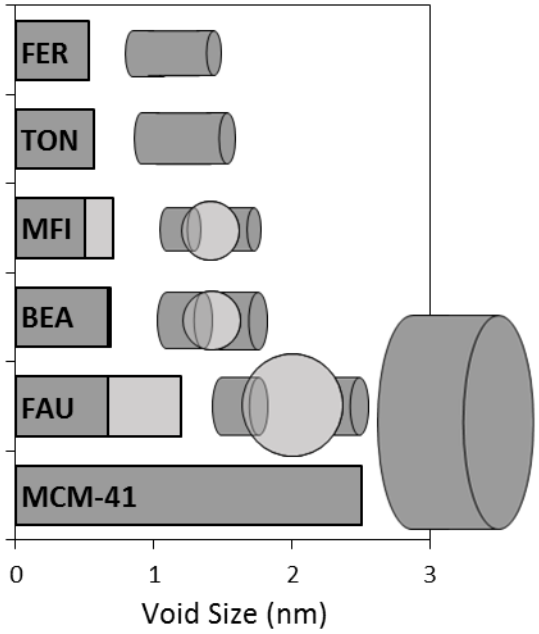

Here, we also studied the selectivity of protons within solid acid catalysts, specifically selectivities to subsequent products (further condensation and β-scission, Scheme 2), using solid acids without the presence of a hydrogenation function (Chapter 3). This study provides a mechanistic understanding of catalyst deactivation and of β-scission reaction pathways through the investigation of effects of acetone conversion, reaction temperature, acetone pressure, H2O pressure, and proton density (Si/Al ratio). The methods developed allow rigorous comparisons of selectivities measured on different aluminosilicate samples and at different reaction conditions. We find that the MFI framework has unique selectivity toward β-scission products presumably due to the preferential stabilization of the transition states that mediate these reaction pathways. Using a set of MFI samples of different proton densities, we address conflicting reports in the literature pertaining β-scission (C_4) selectivity during acetone condensation including: the identity of the precursor to β-scission, the site that catalyzes β-scission, the effect of H_2O on catalyst stability, and the effect of proton density. The last point has been somewhat surprising where we find decreasing proton density (the proposed active site) increased C_4 selectivity; an effect that has been reported but not explained in the literature [27, 28]. We have determined, through kinetic measurements at low acetone conversions, that two parallel β-scission pathways occur on microporous solid acids (Scheme 4): the acid-catalyzed β-scission of ketol species and the free-radical β-scission of C_6-alkenone/C_6-alk-diene-ol species. The proposed radical pathway is the dominate pathway for C_4 formation in dry conditions (0 kPa H_2O added) and provides an explanation to the increasing C_4 selectivity with decreased proton density, where empty voids stabilize transition states that mediate the propagation of radicals forming isobutene. Radical reaction pathways are the only mechanism consistent with the kinetic dependencies measured for

these C_4 selectivities, where the rate clearly depends on the product of two sites (protons and empty void space). Here, we also rely on theoretical calculations of gaseous species and radicals (coupled cluster methods (CCSD), Gaussian 09) to support the plausibility of the occurrence of these pathways.

Scheme 4: Acid-catalyzed [29] and free-radical [30] β-scission reaction pathways that result in similar product species*

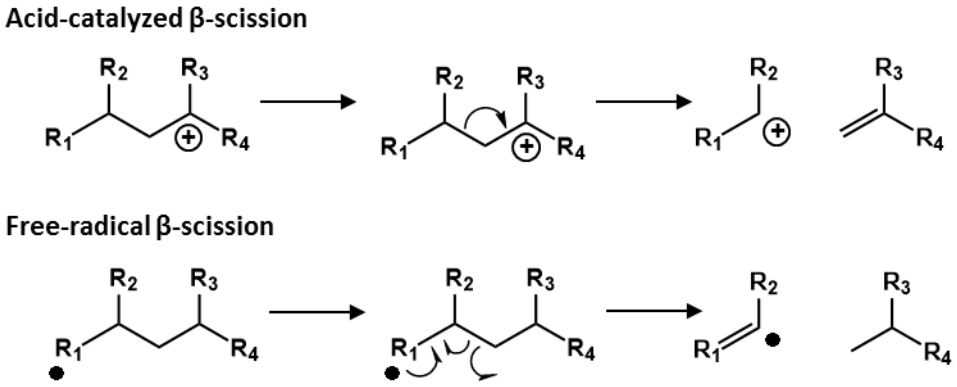

* Location of positive charge and of the unpaired electron are denoted, res with a black circle.

This dissertation discusses the mechanism of acetone condensation by measuring intrinsic reactivities and selectivities of protons located within microporous voids. The mechanistic interpretations of these measurements have provided significant contributions in understanding catalyst deactivation during acetone condensation and determining techniques to inhibit deactivation. This work also demonstrates the importance of effectively using a combination of experimental techniques and theoretical calculations to develop an understanding of the catalytic consequences of fundamental catalyst properties (acid strength and confinement). The insights provided from the theoretical treatments of the effects of acid strength [31-33] and confinement (Chapter 2) extend the general understanding of solid acid catalysis and aid in selecting the most reactive or most selective zeolite for a given chemical conversion.

1. References

1. Taarning, E., et al., *Zeolite-catalyzed biomass conversion to fuels and chemicals.* Energy & Environmental Science, 2011. **4**(3): p. 793-793.
2. Schinzer, D. and R. Mahrwald, *Modern Aldol reactions. Vol. 1: Enolates, Organocatalysis, Biocatalysis and Natural Product Synthesis*. Vol. 1. 2004: Wiley-VCH.
3. Wurtz, C.-A., *Sur un aldéhyde-alcool.* Bulletin de la Société Chimque, 1872. **17**: p. 436-442.
4. Di Cosimo, J.I. and C.R. Apesteguía, *Study of the catalyst deactivation in the base-catalyzed oligomerization of acetone.* Journal of Molecular Catalysis A: Chemical, 1998. **130**(1-2): p. 177-185.
5. Luo, S. and J.L. Falconer, *Aldol condensation of acetaldehyde to form high molecular weight compounds on TiO2.* Catalysis letters, 1999. **57**: p. 89-93.
6. Wang, S., K. Goulas, and E. Iglesia, *Condensation and esterification reactions of alkanals, alkanones, and alkanols on TiO_2: Elementary steps, site requirements, and synergistic effects of bifunctional strategies.* Journal of Catalysis, 2016. **340**: p. 302-320.
7. Sad, M.E., M. Neurock, and E. Iglesia, *Formation of C-C and C-O bonds and oxygen removal in reactions of alkanediols, alkanols, and alkanals on copper catalysts.* Journal of the American Chemical Society, 2011. **133**(50): p. 20384-98.
8. Biaglow, A.I., et al., *A 13C NMR Study of the Condensation Chemistry of Acetone and Acetaldehyde Adsorbed at the Brønsted Acid Sites in H-ZSM-5.* Journal of Catalysis, 1995. **151**(2): p. 373-384.
9. Lin, F. and Y.-H.C. Chin, *Mechanism of intra- and inter-molecular CC bond formation of propanal on Brønsted acid sites contained within MFI zeolites.* Journal of Catalysis, 2014. **311**: p. 244-256.
10. Chang, C.D. and A.J. Silvestri, *The Conversion of Methanol and Other O-Compounds to Hydrocarbons over Zeolite Catalysts.* Journal of Catalysis, 1977. **259**(47): p. 249-259.
11. Salvapati, G.S., K.V. Ramanamurty, and M. Janardanarao, *Selective catalytic self-condensation of acetone.* Journal of Molecular Catalysis, 1989. **54**(1): p. 9-30.
12. Weitkamp, J. and M. Hunger, *Acid and base catalysis on zeolites*, J. Cejka, et al., Editors. 2007. p. 787-835.
13. Baerlocher, C. and L.B. McCusker. *Database of Zeolite Structures*. February 6, 2016]; Available from: http://www.iza-structure.org/databases/.
14. Gounder, R. and E. Iglesia, *The catalytic diversity of zeolites: confinement and solvation effects within voids of molecular dimensions.* Chemical communications (Cambridge, England), 2013. **49**(34): p. 3491-509.
15. Jones, A.J. and E. Iglesia, *The Strength of Brønsted Acid Sites in Microporous Aluminosilicates.* ACS Catalysis, 2015. **5**(10): p. 5741-5755.
16. Jones, A.J., S.I. Zones, and E. Iglesia, *Implications of Transition State Confinement within Small Voids for Acid Catalysis.* The Journal of Physical Chemistry …, 2014. **118**(31): p. 17787-17800.
17. Kubelková, L., et al., *Acetone Conversion and Deactivation of Zeolites*, in *Studies in Surface Science and Catalysis*, P.A. Jacobs and R.A.v. Santen, Editors. 1989, Elsevier. p. 1203-1212.
18. Hutchings, G., et al., *Acetone conversion to isobutene in high selectivity using zeolite β catalyst.* Catalysis letters, 1993. **21**(1-2): p. 49-53.

19. Konno, H., et al., *Characterization and catalytic performance of modified nano-scale ZSM-5 for the acetone-to-olefins reaction.* Applied Catalysis A: General, 2014. **475**: p. 127-133.
20. Melo, L., et al., *Effect of the metallic/acid site (nPt/nA) ratio on the transformation of acetone towards methyl isobutyl ketone.* Catalysis letters, 1997. **44**: p. 201-204.
21. Melo, L., et al., *Synthesis of methyl isobutyl ketone using Pt–H ZSM5 bifunctional catalysts. III. Effect of the nPt/nA parameter on the xPt–H ZSM5 (y) catalysts.* Catalysis letters, 1998. **51**: p. 207-212.
22. Yang, P., et al., *One-step synthesis of methyl isobutyl ketone from acetone over Pd/MCM-22 zeolites.* Journal of Molecular Catalysis A: Chemical, 2007. **272**(1-2): p. 75-83.
23. Tago, T., et al., *Selective synthesis for light olefins from acetone over ZSM-5 zeolites with nano- and macro-crystal sizes.* Applied Catalysis A: General, 2011. **403**(1-2): p. 183-191.
24. Grimme, S., S. Ehrlich, and L. Goerigk, *Effect of the Damping Function in Dispersion Corrected Density Functional Theory.* Journal of computational chemistry, 2011. **32**(7): p. 1456-1465.
25. Grimme, S., et al., *A consistent and accurate ab initio parametrization of density functional dispersion correction (DFT-D) for the 94 elements H-Pu.* The Journal of Chemical Physics, 2010. **132**(15): p. 154104.
26. First, E.L., et al., *Computational characterization of zeolite porous networks: an automated approach.* Physical chemistry chemical physics : PCCP, 2011. **13**(38): p. 17339-58.
27. Cejka, J. and J. Pavel, *Influence of water on activity, selectivity and deactivation of zeolites in acetone transformation.* Collection of Czechoslovak Chemical Communications, 1989. **54**(11): p. 2998-3002.
28. Veloso, C.O., J.L.F. Monteiro, and E.F. Sousa-Aguiar, *Aldol condensation of acetone over alkali cation exchanged zeolites.* Studies in Surface Science and Catalysis, 1994. **84**: p. 1913-1920.
29. Tiong Sie, S., *Acid-catalyzed cracking of paraffinic hydrocarbons. 1. Discussion of existing mechanisms and proposal of a new mechanism.* Industrial and Engineering Chemistry Research, 1992. **31**(8): p. 1881-1889.
30. Gilbert, K.E. and J.J. Gajewski, *Coal liquefaction model studies: free radical chain decomposition of diphenylpropane, dibenzyl ether, and phenethyl phenyl ether via β-scission reactions.* The Journal of Organic Chemistry, 1982. **47**(25): p. 4899-4902.
31. Macht, J., R.T. Carr, and E. Iglesia, *Consequences of Acid Strength for Isomerization and Elimination Catalysis on Solid Acids.* Journal of the American Chemical Society, 2009. **131**: p. 6554-6565.
32. Jones, A.J., et al., *Acid strength and solvation in catalysis by MFI zeolites and effects of the identity, concentration and location of framework heteroatoms.* Journal of Catalysis, 2014. **312**: p. 58-68.
33. Carr, R.T., M. Neurock, and E. Iglesia, *Catalytic consequences of acid strength in the conversion of methanl to dimethyl ether.* Journal of Catalysis, 2011. **278**: p. 78-93.

Chapter 2

Elementary steps in acetone condensation reactions catalyzed by solid Brønsted acids with diverse void structures

Abstract

The study of aldol condensation on solid acid catalysts has been plagued by the unselective nature of the Brønsted acid site (H^+) leading to the formation of undesired side products and rapid catalyst deactivation. These issues stem from the highly reactive, equilibrated pool of unsaturated dimer intermediates and have prevented mechanistic studies on these catalysts. Here, rates on solid acids are stabilized through the addition of a hydrogenation function (H_2 and Pt clusters) that converts the reactive, unsaturated intermediates into stable, saturated alkanones. Kinetic, isotopic, and spectroscopic data supported by theoretical simulations are used to rigorously determine the mechanism of aldol condensation on microporous and mesoporous aluminosilicates of different void sizes (FER, TON, MFI, BEA, FAU, and MCM-41) and MFI samples of different acid strength (isomorphously-substituted Al-, Fe-, Ga-, B-MFI). Titrations with 2,6-di-*tert*-butyl pyridine, during acetone condensation catalysis, are consistent with H^+ being the only kinetically-relevant site. Infrared spectra measured during catalysis indicate that all H^+ are saturated with H-bonded acetone at all conditions studied, which is consistent with frequencies and binding energies calculated using density functional theory (DFT). Acetone condensation turnover rates (normalized per accessible H^+) are first-order with acetone pressure (0.1-5 kPa acetone, 463-483 K) and show no H/D kinetic isotope effect when flowing acetone-d_6/D_2. These data together with DFT-simulations suggest a kinetically-relevant C-C bond formation transition state. The measured first-order condensation rate constant (k_{cond}) reflects the difference in Gibbs free energy between the condensation transition state and its relevant precursors—acetone H-bonding with H^+ and gaseous acetone. k_{cond} values, measured on the range of solid acid materials studied, depend on the size and shape of the void around the H^+ and the acid strength of the H^+. The effects of confinement are accurately assessed by a descriptor of these void environment where interactions between framework oxygens and the atoms of the organic moiety are described by additive contributions of Lennard-Jones potentials. The effects of acid strength on the intrinsic reactivity of protons are characterized by catalyst deprotonation energy (DPE), a theoretical probe, that describes the stability of the conjugate anion.

2.1 Introduction

The conversion of biomass-derived oxygenates to more valuable chemicals and fuels requires precise mechanistic details of surface reactions that remove O-atoms and form new C-C bonds [1]. These oxygenates are derived from biomass via hydrolysis [2], pyrolysis [3], or fermentation [4] processes; they differ, often significantly, from the desired fuels and chemicals in their boiling ranges and oxygen content. Aldol condensation reactions, such as those depicted in Scheme 1, form new C-C bonds and reject O-atoms as H_2O, thus increasing the energy density and the boiling point range of biomass-derived oxygenates [1].

Scheme 1: Aldol condensation reaction pathways on acid or base catalysts (-R_i = C_nH_{2n+1}(alkyl) or H, i = 1-4).

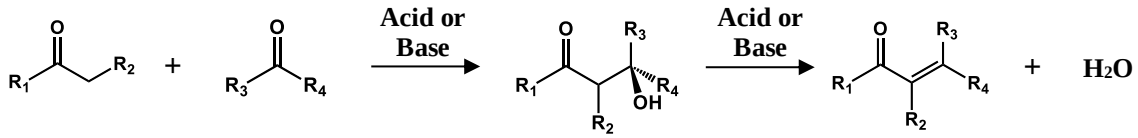

Solid catalysts, such as metal oxides [5-7], metals [8], and Brønsted acids [9, 10], allow facile separations of products from catalysts, but are prone to fast deactivation, inhibition by products, and yield losses via secondary reactions. Microporous Brønsted acids provide confining voids of molecular dimensions surrounding acidic protons; such voids can confer unique reactivity and selectivity to these protons, in spite of the similar acid strength of aluminosilicates [11, 12], through selective diffusion of certain reactants and products or preferential van der Waals stabilization of specific intermediates and transition states. Several zeolites have been reported to catalyze aldol condensations (MFI [9, 10, 13-18], BEA [19, 20], MWW [21], and FAU [13, 18, 22]), but ubiquitous deactivation and inhibition by co-products have precluded unequivocal mechanistic conclusions, making it difficult to assess even the active sites involved in condensation reactions: acidic protons, non-framework Al acting as Lewis acid centers, or both types of acid sites acting in concert [9, 18, 23].

Sequential condensations reactions of α,β-unsaturated products form arenes [24, 25] (e.g. 1,3,5-trimethylbenzene from acetone condensation) that bind strongly to Brønsted acid active sites, thus preventing those sites from undergoing additional turnovers [13, 26]. The presence of an intracrystalline Pt function [21, 26-29] has been reported to inhibit the formation of such arenes by hydrogenating these species to their saturated alkanone analogs. The practical implementation of these bifunctional strategies seeks to limit concurrent undesired acetone hydrogenation reactions by using Pt, which favors C=C over C=O hydrogenation [30, 31], and low partial pressures of H_2; this, however, leads to only partial inhibition of deactivation processes [21, 26-29] and precludes kinetic measurements and rigorous assessment of intrinsic reactivities, which require stable catalysts. Such kinetic measurements require higher partial pressures of H_2 with concomitant acetone losses to propane via sequential hydrogenation-dehydration-hydrogenation reactions of acetone. Acetone losses, however, do not create significant axial acetone concentration gradients along the catalyst bed at the low conversions in the present study. Here, these bifunctional strategies use excess H_2 (10-100 H_2/acetone molar ratio), extracrystalline Pt (mixed physically as Pt/SiO_2 with aluminosilicates), and, in some instances, intracrystalline Pt (exchanged into aluminosilicate crystals) to allow stable rates during kinetic, isotopic, and infrared measurements.

This study reports kinetic, spectroscopic, isotopic, and theoretical evidence for the identity and kinetic relevance of the elementary steps that mediate acetone condensation on acidic forms of solid Brønsted acid catalysts with diverse confining environments (FER, TON, MFI, BEA, FAU, MCM-41) and diverse acid strength (isomorphously-substituted Al-, Fe-, Ga-, and B-MFI).

Turnover rates, determined by rigorous assessments of the number and type of acid sites via titrations with organic bases, allow comparisons of intrinsic reactivity among these solid acids. Condensation reactions occur exclusively on protons without detectable contributions from Lewis acid sites. Infrared spectra during catalysis show that protons are covered with H-bonded acetone at saturation coverages, and measured effects of acetone pressure on rates and theoretical treatments are consistent with a sequence involving kinetically-relevant C-C bond formation mediated by a bimolecular transition state consisting of a C_3-alkenol and a protonated acetone molecule. The interpretation of turnover rates (per proton) in terms of rate constants for elementary steps allow the benchmarking of measured free energy and enthalpy barriers against density functional theory (DFT) estimates; these DFT methods exploit the recent development of functionals that account for dispersion forces [32, 33], essential to describe the stabilization of reactants and transition states by confinement within aluminosilicates with diverse frameworks.

The different reactivities of these aluminosilicates reflect differences in Gibbs free energy barriers, which are influenced by the void environment surrounding protons. We show the correlation between condensation rate constants and a geometric descriptor of void size, largest cavity diameter, which qualitatively shows that rate constants are largest when the void size approaches the size of the transition state (TS). This geometric descriptor, however, fails to describe the significant difference in rate constants on MFI and BEA; two frameworks that have similar largest cavity diameters (0.70 and 0.69 nm, respectively [34]).

Void environments stabilize the relevant organic moieties, TS and adsorbed species, through van der Waals interactions based on the size and the shape of both the void environment and the organic moiety. Here, we present a method to determine the van der Waals stabilization energy (E_{vdW}) by enumerating the interactions between the O-atoms of the framework and the atoms of the organic moiety (DFT-optimized structures at the T12 site in MFI) using two-atom Lennard-Jones potentials and sampling several orientations ($> 10^3$) of the organic moiety at each distinct T-site location in each framework. The difference in the resulting E_{vdW} values of the TS and its precursors at each T-site location are then ensemble-averaged ($\langle \Delta E_{\mathrm{vdW}} \rangle$) over all T-sites a given framework (FER, TON, MFI, BEA, FAU) to describe the observed effects of void environment on condensation turnover rates. Such approaches rigorously account for the diversity of void environments in each framework, and $\langle \Delta E_{\mathrm{vdW}} \rangle$ values accurately describe differences in measured rate constants on the different aluminosilicates used. This method of estimating $\langle \Delta E_{\mathrm{vdW}} \rangle$ values provides a general descriptor of the catalytic consequences of microporous void environments and is applicable to any reaction for which there are reasonable estimations of the kinetically-relevant organic moieties and their structures.

Acid-catalyzed reactions are mediated by ion-pair transition states, which require a separation of charge [35-39]. The C-C bond formation transition state for acetone condensation is an ion-pair and the relevant precursors (H-bonded acetone and gaseous acetone) exhibit negligible charge separation; thus, the free energy barrier required for condensation reactions is sensitive to

the acid strength of the catalyst—the ability of the conjugate anion to accept charge. Deprotonation energy (DPE) is the energy required to heterolytically cleave the proton from the conjugate anion and to separate the charged species to a distance they no longer interact. DPE is a rigorous probe of acid strength and independent of effects of zeolite void structure. These energies are theoretically-accessible and DPE values for the different heteroatoms (Al, Fe, Ga, and B) have been used from the literature [36]. Acetone condensation rates increase exponentially with decreasing DPE-values (increasing catalyst acid strength) consistent with an ion-pair transition formed from uncharged precursors, which agrees with the DFT-simulations performed here. Similar experiments using isomorphously-substituted MFI samples (Al, Fe, Ga, B) to elucidate the effects of acid strength on acetone condensation have been reported previously [23, 26]; the conclusions of these studies, however, were obscured by artifacts of rapid catalyst deactivation precluding assessments of intrinsic reactivities by these studies, which highlights the importance of understanding and preventing catalyst deactivation before assessing the catalytic effects of catalyst properties.

2.2 Methods

2.2.1 Catalyst synthesis protocols

NH_4^+-MFI (Zeolyst, Si/Al_{tot} = 16.6, 29.2, 43.8, and 168.3), NH_4^+-BEA (Zeolyst, Si/Al_{tot} = 11.8 and 43.3), NH_4^+-FER (Zeolyst, Si/Al_{tot} = 10.3), NH_4^+-TON (BP p.l.c., Si/Al_{tot} = 40.0), NH_4^+-MCM-41 (Sigma-Aldrich, 643653, Si/Al_{tot} = 37.8), NH_4^+-Fe-MFI (BP p.l.c., Si/Al_{tot} = 26.0), NH_4^+-Ga-MFI (BP p.l.c., Si/Al_{tot} = 45.0), NH_4^+-B-MFI (BP p.l.c., Si/Al_{tot} = 43.0), and SiO_2 (Davison Chemical, Chromatographic Silica, Media, CAS no. 112926-00-8, 280 $m^2\ g^{-1}$, 0.57 $cm^3\ g^{-1}$ pore volume) materials were treated in flowing dry air (1.5 $cm^3\ g^{-1}\ s^{-1}$, zero grade, Praxair) by heating to 823 K (at 0.025 K s^{-1}) and holding for 5 h. Dealuminated H-FAU (FAU, Si/Al_{tot} = 7.5) was prepared using methods reported in the LZ-210 patent for the selective extraction of non-framework Al [40, 41]. Si, Al, and Na contents were measured by inductively-coupled plasma atomic emission spectroscopy (ICP-AES; Galbraith Laboratories). The nomenclature and provenance of the samples used and their Si/Al, Al/unit cell, and H^+/Al ratios are listed in Table 1. The largest inscribed sphere (largest cavity diameter) and the largest sphere that can traverse each framework (pore-limiting diameter) derived from crystallographic data [34] are also shown in Table 1.

Pt/SiO_2 (2.0% wt Pt) was prepared by incipient wetness impregnation of SiO_2 (Davison Chemical, Chromatographic Silica, Media, CAS no. 112926-00-8, 280 $m^2\ g^{-1}$, 0.57 $cm^3\ g^{-1}$ pore volume) with aqueous hexacholoroplatinic acid ($H_2PtCl_6 \cdot (H_2O)_6$, Aldrich, CAS #16941-12-1). The impregnated powders were treated in dry air (1.5 $cm^3\ g^{-1}\ s^{-1}$, zero grade, Praxair) by heating to 383 K (at 0.033 K s^{-1}; 3 h hold) and then to 873 K (at 0.033 K s^{-1}; 5 h hold) and cooled to ambient temperature. Samples were then exposed to 10% H_2/He (0.8 $cm^3\ g^{-1}\ s^{-1}$, certified standard,

Praxair) and heated to 873 K (at 0.083 K s^{-1}; 2 h hold), cooled to ambient temperature in He (0.8 cm^3 g^{-1} s^{-1}, UHP, Praxair), and then contacted with 1% O_2/He (0.8 cm^3 g^{-1} s^{-1}, certified standard, Praxair) at ambient temperature for 0.5 h to passivate the samples before exposure to ambient air.

Pt was exchanged into H-BEA zeolite (Pt/BEA-1) by dropwise addition of a tetraammineplatinum(II) nitrate solution (0.025 M, $[Pt(NH_3)_4](NO_3)_2$, Sigma-Aldrich, CAS #20634-12-2) to an aqueous suspension of zeolite crystals (100 cm^3 H_2O (g zeolite)$^{-1}$) to achieve a Pt content of 1.0% wt; the suspension was stirred at ambient temperature for 12 h. Solids were recovered by vacuum filtration, rinsed with deionized water (>17.6 Ω cm resistivity, 1000 cm^3 H_2O (g zeolite)$^{-1}$) and treated in dry air (1.5 cm^3 g^{-1} s^{-1}, zero grade, Praxair) by heating to 383 K (at 0.033 K s^{-1}; 3 h hold) and then to 723 K (at 0.025 K s^{-1}; 4 h hold). These samples were then cooled to 573 K and held for 3h in flowing 10% H_2/He (0.8 cm^3 g^{-1} s^{-1}, certified standard, Praxair) before cooling to ambient temperature and exposing the samples for 0.5 h to flowing 1% O_2/He (0.8 cm^3 g^{-1} s^{-1}, certified standard, Praxair).

Table 1: Zeolite and mesoporous aluminosilicate sample information

Zeolite	Provenance	Si/Al ratio[a]	Al/ unit cell[b]	H^+/Al	H^+/Al[e]	d_{LCD}[f] (nm)	d_{PLD}[g] (nm)
MFI-1	Zeolyst	16.6	5.47	0.65[c]	0.52	0.70	0.50
MFI-2	Zeolyst	29.2	3.18	0.77[c]	0.72	0.70	0.50
MFI-3	Zeolyst	43.8	2.14	1.03[c]	0.89	0.70	0.50
MFI-4	Zeolyst	168.3	0.58	0.70[c]	0.62	0.70	0.50
BEA-1	Zeolyst	11.8	4.98	0.22[d]	0.39	0.69	0.67
BEA-2	Zeolyst	43.3	1.44	1.04[d]	1.30	0.69	0.67
FER	Zeolyst	9.5	3.19	0.35[c]	0.73	0.70	0.53
FAU	[37]	7.5	17.45	0.38[d]	0.64	1.19	0.67
MCM-41	Sigma-Aldrich	37.8	--	0.42[d]	--	2.50[h]	2.50[h]
TON	BP p.l.c.	40.0	0.59	--	0.88[*]	0.57	0.57
Fe-MFI	BP p.l.c.	26.0	3.56	--	0.15	0.70	0.50
Ga-MFI	BP p.l.c.	45.0	2.09	--	0.75	0.70	0.50
B-MFI	BP p.l.c.	43.0	2.18	--	0.70	0.70	0.50

[a] elemental analysis (ICP-AES; Galbraith Laboratories).
[b] from Si/Al ratio and framework crystal structure [42].
[c] from pyridine titrations during CH_3OH dehydration at 433 K [36].
[d] from 2,6-di-*tert*-butylpyridine titrations during acetone condensation at 473 K (Figure 3, methods in Section 2.2.3).
[e] from the amount of NH_3 evolved from NH_4^+-exchanged samples [43], *TON [44], **Fe-, Ga-, B-MFI samples (this work).
[f] largest-cavity diameter [34].
[g] pore-limiting diameter [34].
[h] channel diameter reported by Sigma-Aldrich.

2.2.2 Catalytic rate and selectivity measurements

Condensation rates were measured at 463-483 K and low acetone conversion (< 5%) to maintain differential reaction conditions. Samples containing extracrystalline Pt as physical mixtures (e.g. MFI-1 + Pt/SiO_2) were prepared by crushing the mixture of aluminosilicate crystals and Pt/SiO_2 into small aggregates (< 180 μm) with a mortar and pestle for 0.25 h. Powders were pressed into wafers (690 bar, 0.1 h), crushed, and sieved to retain 180-250 μm aggregates. These aggregates (0.020-0.200 g) were held within a tubular quartz reactor (7.0 mm i.d.) and kept at constant temperature using a three-zone resistively-heated furnace (Applied Test Systems Inc., model number 3210) controlled by three independent temperature controllers (Watlow Series 988); temperatures were measured using a K-type thermocouple (Omega) in contact with the outer surface of the quartz reactor at the midpoint along the catalyst bed.

Solid acid catalysts (Table 1) were treated in flowing dry air (83.3 $cm^3\ g^{-1}\ s^{-1}$, Extra dry, Praxair) by heating to 818 K (at 0.025 K s^{-1}; 2 h hold) and then cooled to reaction temperatures. Solid acids were separately treated at similar conditions before mixing with Pt/SiO_2. Pt-containing samples—physical mixtures and Pt-exchanged mixtures—were exposed to 10% H_2/He (83.3 $cm^3\ g^{-1}\ s^{-1}$, certified standard, Praxair) and heated to 623 K (at 0.025 K s^{-1}; 2 h hold) and then cooled to reaction temperatures before condensation rate measurements.

Catalyst deactivation was described using first-order deactivation kinetics [45]:

$$r(t) = r(0) \cdot \exp(-k_d t) \quad (1)$$

where r is the condensation rate per Al-atom, t is the time on stream, and k_d is the effective first-order deactivation rate constant. Such process require that sites deactivate at rates independent of the prevalent concentration of reactants and products. Here, we consider rates to have reached constant values when first-order deactivation constants (k_d) are smaller than 0.05 ks^{-1}.

Acetone (≥ 99.9%, Sigma-Aldrich) was introduced into He (UHP, Praxair) and H_2 (UHP, Praxair) streams using a liquid syringe pump (Legato 100, KD Scientific) and vaporized in transfer lines kept at 403 K. Inlet and effluent streams were analyzed by gas chromatography (GC; Agilent 6890A) using flame ionization detection (FID) after chromatographic separation (HP-1 column, Agilent). Molecular speciation was confirmed using mass spectrometry (MKS Spectra Minilab) and known standards. Retention times and response factors were determined from known concentrations of these compounds: acetone (≥ 99.9%, Sigma-Aldrich), diacetone alcohol (≥ 98%, Santa Cruz Biotechnology), mesityl oxide (98%, Spectrum Chemical), isobutene (99.0%, Praxair), acetic acid (≥ 99.99%, Sigma Aldrich), and 1,3,5-trimethylbenze (98%, Sigma-Aldrich), methyl isobutyl ketone (99.5%, ACROS Organics). Isotopic experiments, using acetone-d_6 (99.9%, Sigma-Aldrich) and D_2 (99.8%, Specialty Gases of America), were performed to measure H/D kinetic isotope effects (*KIE*):

$$KIE = \frac{k_H}{k_D} \quad (2)$$

where k_H and k_D denote the first-order condensation rate constants for undeuterated and perdeuterated acetone in the presence of H_2 and D_2, respectively.

Diacetone alcohol (DA), the initial acetone condensation product, was not detected among reaction products because its fast dehydration and favorable thermodynamics to mesityl oxide (MO) and H_2O lead to DA concentrations below chromatographic detection limits (3.5×10^{-13}-5.6×10^{-9} Pa DA, Supporting Information 2.6.1; 0.05 Pa DA detection limit).

2.2.3 Infrared spectra collected during catalysis

Infrared spectra were measured in transmission mode using a Nicolet NEXUS 670 spectrometer equipped with a Hg-Cd-Te (MCT) detector by averaging 64 scans in the 4000-400 cm^{-1} spectral range with 2 cm^{-1} resolution. Samples (5-15 mg) were pressed (690 bar, 0.1 h) into self-supporting wafers (3.2 cm^2) and held within a quartz vacuum cell equipped with NaCl windows. Wafers were heated to 818 K (at 0.025 K s^{-1}; 2 h hold) in dry air (83.3 cm^3 g^{-1} s^{-1}, zero grade, Praxair) and cooled to reaction temperature. Acetone (0.04-2 kPa) was injected into a He stream at 403 K using a liquid syringe pump (KDS-100, KD Scientific). All spectra were normalized by the intensity of the Si-O-Si bands (2100-1750 cm^{-1}).

2.2.4 Measurements of the number and type of active site by titrations with probe molecules during catalysis

The number of accessible protons on BEA-1, BEA-2, FAU, and MCM-41 samples were measured by titration with 2,6-di-*tert*-butyl pyridine (DTBP; >97%, Sigma-Aldrich) during acetone condensation on Pt-containing samples. DTBP (0.1-1 Pa) was introduced after condensation rates reached steady-state values (Section 2.2.2). DTBP concentrations in the effluent were measured by the chromatographic protocols described above and the number of protons were determined by assuming a 1:1 DTBP:H^+ ratio. Proton counts on MFI and TON were determined by NH_3 evolution from their NH_4-exchanged forms, because DTBP cannot access intracrystalline protons via diffusion through the microporous channels [43, 44]. The proton counts on FER were determined by titration with pyridine (99.8%, Sigma-Aldrich) [36], in order to titrate only protons in the 0.53 nm straight channels [34], which are accessible to acetone (0.50 nm, kinetic diameter [46]), but not those in the 0.70 nm cages [34], which are inaccessible to acetone reactants because these cages can only be accessed via 0.33 nm [47]. All proton locations in the FER framework are accessible to NH_3 and are counted when using NH_3 evolution from NH_4-exchanged FER (Table 1). The proton counts from pyridine titration and NH_3 evolution from NH_4-exchanged samples are similar on MFI (Table 1) because both methods are accurate for determining the number of protons on MFI.

2.2.5 Theoretical treatments of species and their reactions in confined environments

The structures and energies of MFI aluminosilicates, gaseous and bound species, and transition states were calculated using periodic plane-wave DFT methods, as implemented in the Vienna *ab initio* simulation package (VASP 5.35) [48-51]. Valence electronic states were described using planewaves with an energy cutoff of 396 eV. Projector augmented-wave potentials (PAW5) [52, 53] were used to describe interactions among valence electrons and atom cores. Exchange and correlation energies were described by the revised Perdew-Burke-Ernzerhof (RPBE) form of the generalized gradient approximation (GGA) [54, 55] with an empirical dispersive energy correction (DFT-D3) and Becke-Johnson (BJ) damping incorporated at each optimization iteration [32, 33] in order to account for van der Waals forces that influence the stability of confined species. Calculations were also performed using the vdW-DF2 functional [56-59], which also incorporates van der Waals interactions into the structure optimization. A (1 x 1 x 1) γ-centered *k*-point mesh was used to sample the first Brillouin zone. Electronic wavefunctions were optimized until changes in energy between successive iterations were $\leq 1 \times 10^{-6}$ eV, and the structures were relaxed until the forces on all unconstrained atoms were ≤ 0.05 eV $Å^{-1}$. Atomic coordinates and unit cell parameters (2.0022 x 1.9899 x 1.3383 nm^3 and $\alpha = \beta = \gamma = 90°$) for MFI structure were obtained from crystallographic data (319 Si/Al, 0.32 Al/unit cell) [60]. Brønsted acid sites were introduced into the model of the solids by replacing a Si-atom with an Al-atom at the channel intersection (T12 Scheme 2, numbered according to convention [61]) [36, 43] to give a model solid with a Si/Al ratio of 95 (1.0 Al/unit cell). All molecular structures depicted here used an open-source software package for geometric representation (Visualization for Electronic and Structural Analysis; VESTA [62]).

Scheme 2: Structure of H-bonded acetone at T12-site of MFI.

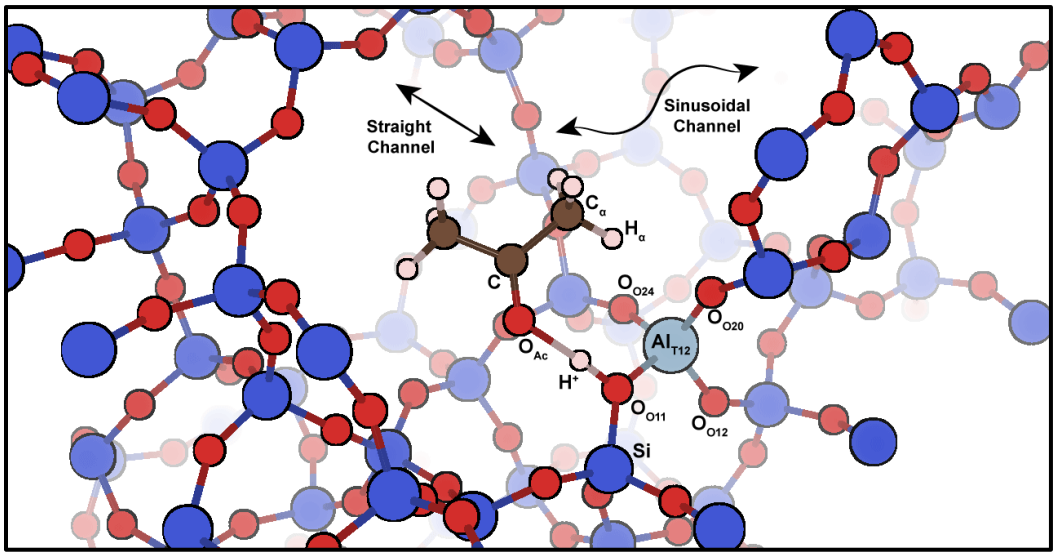

Nudged elastic band (NEB) methods [63] were used to determine the minimum energy paths between reactants and products for each elementary step; structures near the maximum energy along the reaction coordinate were used to isolate transition states using Henkelman dimer methods [64]. Electronic energy changes in NEB calculations were converged to < 1 x 10^{-4} eV and forces on each unconstrained atom were minimized to < 0.3 eV $Å^{-1}$. Dimer calculations of all TS structures used the same convergence criteria as those in the optimization simulations described above.

Frequency calculations were performed on all optimized structures to determine zero-point vibrational energies (*ZPVE*), vibrational enthalpies and free energies (H_{vib} and G_{vib}), and, in the case of gaseous molecules, translational and rotational enthalpies (H_{trans} and H_{rot}) and free energies (G_{trans} and G_{rot}). Low-frequency modes (<150 cm^{-1}) of weakly-bound intermediates and transition states lead to significant errors in vibrational free energies [65]; these modes were replaced by translational and rotational free energies assumed to retain a fraction (0.70) of the translational and rotational free energies of their gaseous analogs, as suggested by adsorption entropy measurements on oxide surfaces [66]. These corrections for zero-point vibrational energies, translations, rotations, and vibrations were added to the VASP-derived electronic energies (E_0) to calculate enthalpies:

$$H = E_0 + ZPVE + H_{vib} + H_{trans} + H_{rot} \tag{3}$$

and free energies:

$$G = E_0 + ZPVE + G_{vib} + G_{trans} + G_{rot} \tag{4}$$

The Gibbs free energies for transition states ($G^{‡}$) and their relevant precursors (G^{p}) were calculated at the T12 site of MFI to estimate free energy barriers ($\Delta G^{‡}_{T12}$):

$$\Delta G^{‡}_{T12} = G^{‡}_{\mathrm{T12}} - \sum_{p} G^{p}_{\mathrm{T12}} \tag{5}$$

Ensemble (exponential) averaging of DFT-estimated free energy barriers was used to account for the distinct binding locations at each of the four vicinal framework O-atoms when structures contain covalent bonds to the framework. The ensemble-averaged Gibbs free energy barrier ($\langle \Delta G \rangle$) was calculated using (derivation provided in Supporting Information, 2.6.2):

$$\langle \Delta G \rangle = -k_B T \ln \left(\sum_{i=1}^{N_{\mathrm{site}}} \exp\left(-\frac{\Delta G_i}{k_B T} \right) \mathrm{P}_{\mathrm{site},i} \right) \tag{6}$$

where k_B is the Boltzmann constant, N_{site} is the number of distinct sites (e.g. for the proton H-bonding to acetone N_{site} = 4, four vicinal O-atoms to the Al), and $P_{site,i}$ is the probability of each site occurring. These probabilities, when calculating free energy barriers for condensation, were calculated by a Boltzmann average of the free energy of the bound species at each site (G^p):

$$P_{site,i} = \frac{\exp\left(-\frac{G_i^p}{k_B T}\right)}{\sum_{j=1}^{N_{site}} \exp\left(-\frac{G_j^p}{k_B T}\right)} \quad (7)$$

which is used with the assumption that all protons are occupied by acetone (discussed in Section 2.3.3) and bound acetone species are equilibrated across the framework O-atoms. Such ensemble averaging is required for a rigorous evaluation of the Gibbs free energy barriers for reaction and adsorption, which are used to calculate, respectively, rate constants (k_{T12}) [67, 68]:

$$k_{T12} = \frac{k_B T}{h} \exp\left(-\frac{\langle \Delta G_{T12}^{\ddagger} \rangle}{k_B T}\right) \quad (8)$$

where h is Planck's constant, and adsorption constants (e.g. acetone adsorption constant (K_{Ac})):

$$K_{Ac} = \exp\left(-\frac{\langle \Delta G_{Ac*} \rangle}{k_B T}\right) \quad (9)$$

These acetone adsorption constants are then used to calculate the fraction of the protons occupied by acetone (θ_{Ac}):

$$\theta_{Ac} = \frac{K_{Ac}(Ac)}{1 + K_{Ac}(Ac)} \quad (10)$$

These DFT-estimated kinetic and thermodynamic constants, as well as free energy and enthalpy barriers, required for acetone condensation at the T12 site in MFI are compared to their corresponding measured values on MFI samples to distinguish plausible mechanism for acetone condensation. These theoretical treatments also provide estimates of the structures for transition states and relevant precursors, which provide the size and shape of these species. Comparisons of these DFT-calculated barriers with measured condensation free energy barriers on a range of aluminosilicates of diverse void environments require an understanding of how the size and shape of these frameworks influence the reaction barrier. Here, we present two methods to estimate the catalytic consequences of the confining void. A geometric method which reduces each species and framework to one dimension, respectively, the characteristic diameter based on the van der Waals volume of the species (Section 2.3.4) and the diameter of the largest accessible cavity diameter (Table 1); and a method based on van der Waals stabilization energies which estimates the fit of

the species in each void environment using Lennard-Jones potentials [69, 70] dependent on both the size and shape of the species and the void. The later method requires that the structures of the transition state and the relevant precursor are placed within each confining environment, which is the subject of the next section.

2.2.6 Placement of intermediates and transition states within confining voids

The DFT-optimized structures for the C-C bond formation transition state and H-bonded acetone at the T12 site of MFI (VASP, RPBE + D3(BJ)) were placed at each crystallographically distinct T-site location in FER, TON, MFI, BEA, and FAU frameworks. The unit cell parameters and crystal structures of FER (a = 1.9018, b = 1.4303, c = 0.7541 nm, and $\alpha = \beta = \gamma$ = 90.0°), TON (a = 1.4105, b = 1.7842, c = 0.5256 nm, and $\alpha = \beta = \gamma$ = 90.0°), BEA (a = 1.2632, b = 1.2632, c = 2.6186 nm, and $\alpha = \beta = \gamma$ = 90.0°), and FAU (a = 2.4345, b = 2.4345, c = 2.4345 nm, and $\alpha = \beta = \gamma$ = 90.0°) were taken from values reported on the International Zeolite Association (IZA) web site [42]. The unit cell parameters and crystal structure used for MFI are provided in Section 2.2.5.

The DFT-derived C-C bond formation transition state consists of an ion-pair (MFI, Al T12 site, VASP, RPBE + D3(BJ)), and the charge at each atom was determined using Löwdin population analyses [71] after transformation of the wavefunctions into localized quasiatomic orbitals (QUAMBO) [72-75]. These charges were used to calculate the center of charge (*CoC*) in the cationic transition state and in the anionic framework, which is located at the [x,y,z]-coordinates given by:

$$CoC = \left[\frac{\sum_i^N C_i x_i}{N}, \frac{\sum_i^N C_i y_i}{N}, \frac{\sum_i^N C_i z_i}{N}\right] \tag{11}$$

where each moiety consists of N atoms, with each atom, i, having a charge (C_i) and a location [x_i, y_i, z_i]. The *CoC* of the transition state moiety was used as the central node (n_{central}) for placing the transition state at each T-site. The *CoC* of the anionic framework was located at the Al-atom for the DFT-optimized transition state structure and the distance between the two *CoC* points (n_{central} and Al-atom) was 0.427 nm at this transition state (MFI, Al T12 site). This distance was assumed not to vary among T-site locations and frameworks due to the strong energetic penalty of separating charge.

The DFT-derived structure of H-bonded acetone maintains the covalent bond between the proton (considered part of organic moiety) and the framework oxygen (MFI, VASP, RPBE + D3(BJ)). This covalent O_{zeolite}-H bond does not vary among DFT-derived structures of H-bonded acetone on MFI at each distinct O-atom vicinal to the T12 site (0.110 $\pm$ 0.002 nm, T12 site, VASP, RPBE + D3(BJ)); the proton of the H-bonded acetone moiety was used as the n_{central} and was placed at this mean distance for each of the crystallography unique framework oxygens of FER, TON, MFI, BEA, and FAU frameworks.

The internal angles and atomic distances of the DFT-derived structures of the organic moieties (transition state and H-bonded acetone; MFI, Al T12 site) were held constant, and these structures were placed at every crystallographically distinct location in each framework using three nodes: (1) the framework atom ($Z_{zeolite}$: Al-atom or O-atom for the transition state or H-bonded acetone, respectively), (2) the central node ($n_{central}$: *CoC* or proton for the transition state or H-bonded acetone, respectively), and (3) the farthest node ($n_{farthest}$), which is the location of the atom in the organic moiety the farthest distance from $n_{central}$. The placement of $n_{central}$ forms a sampling sphere centered at each $Z_{zeolite}$ with a radius equal to the distance described above and a node spacing of 0.032 nm [76]; effects of these parameters are the subject of a later study. The organic moiety was then rotated about $n_{central}$ by varying the angle between the atom of the organic moiety located at $n_{farthest}$ ($X_{farthest}$), $n_{central}$, and $n_{farthest}$ ($X_{farthest}$-$n_{central}$-$n_{farthest}$ angle) by increments of 5° (0°, 5°, 10°, etc.) and by varying the orthogonal dihedral angle with respect to the $n_{farthest}$-$n_{central}$-$Z_{zeolite}$ plane by increments of 10° (0°, 10°, 20°, etc.); such rotations result in sampling 242 orientations of the organic moiety for each central node location (angle -25° to 25° and 155° to 205°, dihedral angle -50° to 50°).

2.3 Results and Discussion

2.3.1 Effects of H_2 and Pt hydrogenation function on catalyst stability and selectivity

Mechanistic studies using kinetic, isotopic, and spectroscopic methods require stable catalysts; such stability has remained elusive for condensation reactions on solid acids, even in the presence of a hydrogenation metal function and H_2 [26-29]. Here, we used H_2 partial pressures (10: H_2/acetone molar ratio) that led to significant selectivity of acetone conversion to propane via sequential hydrogenation-dehydration-hydrogenation pathways in efforts to increase the stability of condensation rates; this selectivity to propane, however, did not affect the mechanistic conclusions for condensation presented here for three reasons. (1) Condensation rates were measured at differential acetone conversions (< 5%), which prevents significant depletion of acetone concentrations. (2) Condensation rates, reported here (shown in Section 2.3.3), were extrapolated to zero residence time (initial conversions) from rates measured at different acetone residence times (demonstrated in Section 2.6.5, SI), which precludes the effects of product concentrations on the rate. (3) Condensation rates measured at initial time on stream are unaffected by H_2O pressure (a by-product from propane formation from acetone) as shown in Supporting Information Section 2.6.5 when gaseous H_2O was added to the reactant stream at partial pressures ($\leq$ 3 kPa H_2O, 1 kPa acetone, MFI-3 + Pt/SiO_2, 473 K) much greater than those produced during catalysis ($\leq$ 0.03 kPa H_2O). These measurements and treatments of condensation rates allow rigorous mechanistic interpretation of condensation rates on these aluminosilicates despite the significant selectivity to propane due to the addition of a hydrogenation function.

Acetone condensation rates on MFI-3 and BEA-1 decreased with time on stream (Fig. 1) with first-order deactivation constants (k_d, Eq. 1) that became smaller as deactivation occurred with increasing time. The curvature evident in the semilogarithmic plot in Figure 1 (MFI-3, BEA-1) is consistent with products of subsequent reactions blocking active sites, where the concentrations of precursors for these subsequent reactions decrease as the catalyst deactivates [77, 78]. Measured condensation rates on MFI-3 (shown in Figure 1a) produced equilibrated mixtures of C_6-alkenones, mesityl and isomesityl oxides (MO; experimental and theoretical evidence in Section 2.6.3, SI), and equimolar amounts of isobutene and acetic acid (C_4 and C_2, respectively; Section 2.6.4, SI). The proportional increase in C_4/C_6 molar ratios with increasing acetone conversion (Fig. 2a, MFI-3) is consistent with a serial reaction pathway where C_4 species form from reactions of C_6 products.

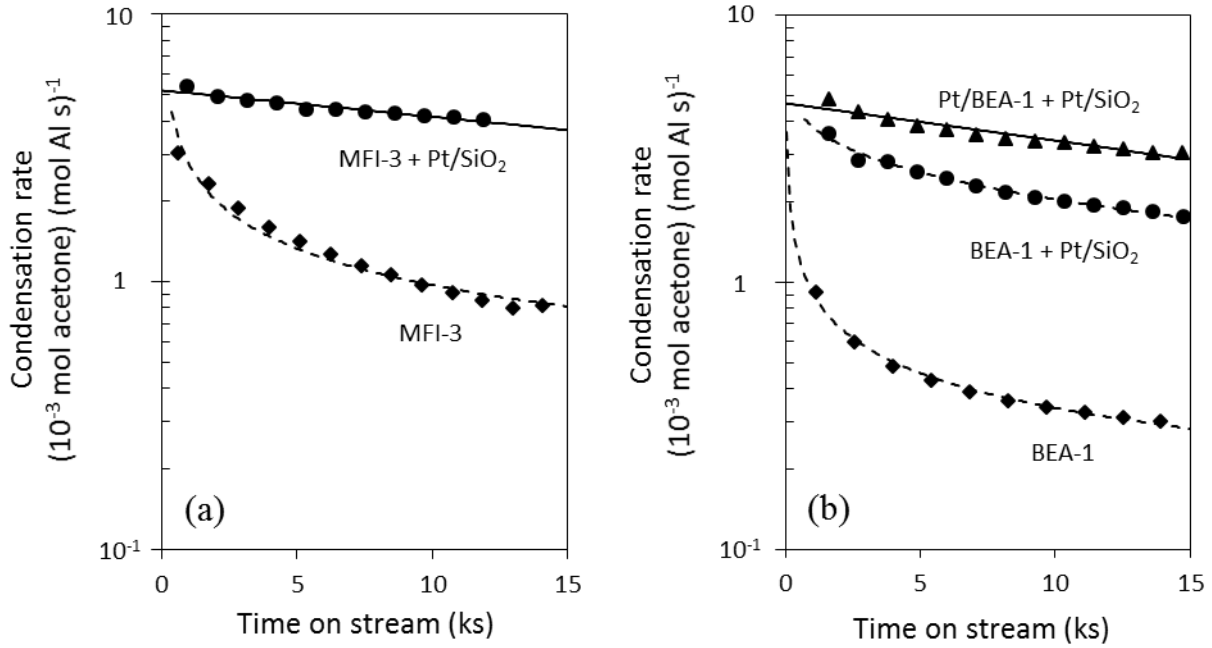

Figure 1: Acetone condensation rate as a function of time on stream on (a) MFI-3 (diamonds) and MFI-3 + Pt/SiO_2 (1% wt. extracrystalline Pt) (circles) and (b) BEA-1 (diamonds), BEA-1 + Pt/SiO_2 (1.3% wt. extracrystalline Pt) (circles), Pt/BEA-1 + Pt/SiO_2 (1% wt. extracrystalline Pt and 1% wt. intracrystalline Pt) (triangles) (473 K, 2.0 kPa acetone, 27 kPa H_2, balance He). Dashed lines represent trends and solid lines are regressed linear fits of the data to the form of Eq. 1.

A Pt function, present as a physical mixture with MFI-3, inhibited deactivation (Fig. 1a, MFI-3 + Pt/SiO_2) and led to much smaller C_4/C_6 product ratios (Fig. 2a). The trace levels of C_4 and C_2 products formed, when Pt is present only outside of the MFI crystals, shows that secondary β-scission reactions seldom occur within a given crystal before primary products enter the extracrystalline fluid phase, where the Pt is located in these samples. The hydrogenation of MO products to less reactive methyl isobutyl ketone (MIBK) prevents subsequent condensation and β-scission reactions of MO or its precursors on acid sites. Initial condensation rates on MFI-3

mixtures with Pt/SiO_2 are similar to those on MFI-3 (Fig 1a), consistent with kinetically-relevant condensation steps that only require the acid function in MFI. These data also show that acetone conversion to MO and H_2O is far from equilibrium, because MO conversion to MIBK on the Pt function would have increased measured rates by scavenging the primary condensation product. The linear trend of condensation rates with time on stream on MFI-3 physically mixed with Pt/SiO_2 (Fig. 1a) allows an accurate assessment of initial condensation rates (Eq. 1), a measure of the intrinsic reactivity of each sample. The initial condensation rate is $5.2 \pm 0.2 \times 10^{-3}$ $(Al\ s)^{-1}$ and the first-order deactivation rate constant (k_d; Eq. 1) is 0.023 ± 0.006 ks^{-1} on MFI-3 physically mixed with Pt/SiO_2 (473 K, 2.0 kPa acetone, 27 kPa H_2), where uncertainties represent the 95% confidence interval of the fitted parameter.

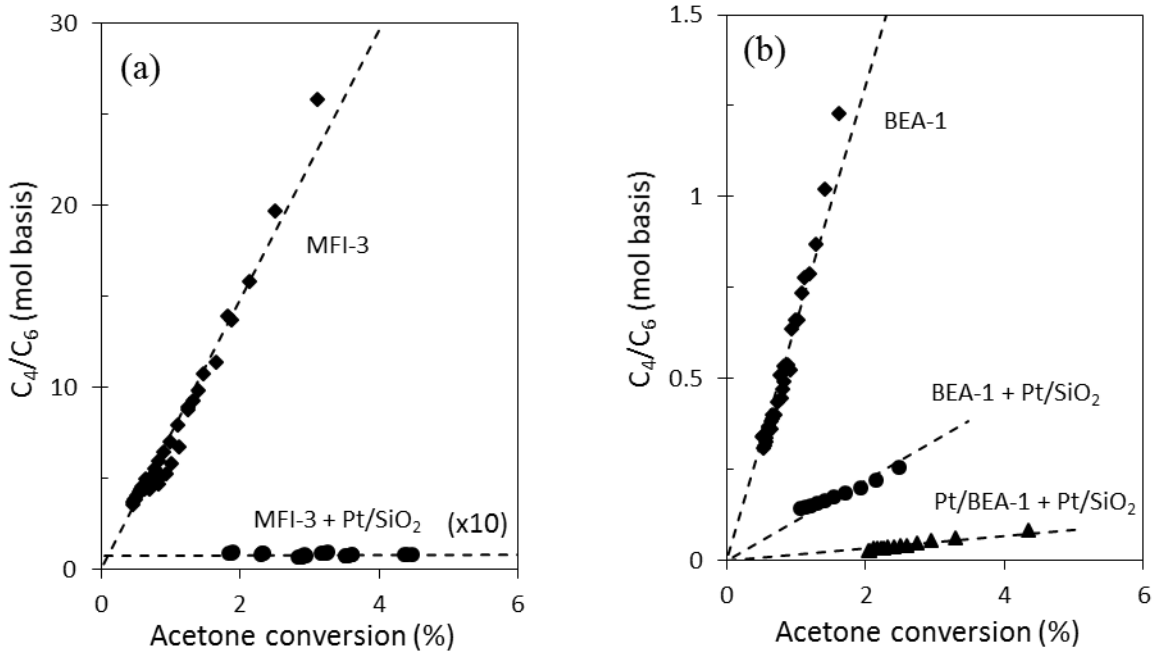

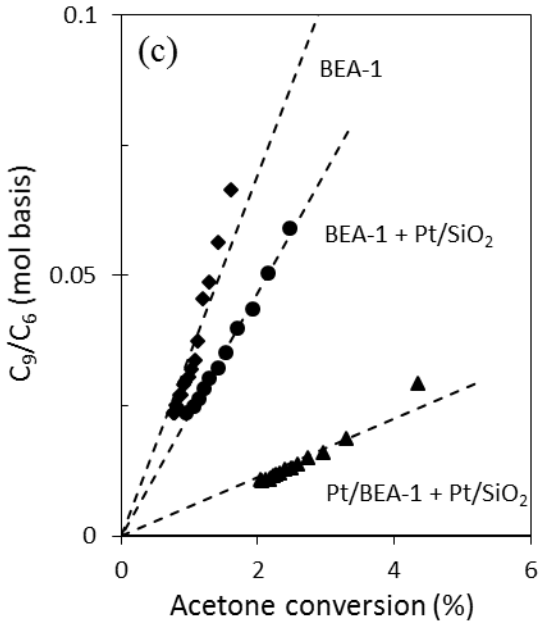

Figure 2: Effect of acetone conversion on C_4/C_6 and C_9/C_6 molar ratios in products on (a) MFI-3 (diamonds) and MFI-3 + Pt/SiO_2 (1% wt. extracrystalline Pt) (circles) and (b and c) BEA-1 (diamonds), BEA-1 + Pt/SiO_2 (1.3% wt. extracrystalline Pt) (circles), Pt/BEA-1 + Pt/SiO_2 (1% wt. intracrystalline Pt and 1% wt. extracrystalline Pt) (triangles) (473 K, 2.0 kPa acetone, 27 kPa H_2, balance He). C_4, C_6, and C_9 denote, respectively, the combined number of moles produced of isobutene and isobutane, MO and MIBK, and TMB. MIBK and isobutane were only detected with Pt present. Dashed lines are regressed linear fits of the data through the origin, except MFI-3 + Pt/SiO_2 where the dashed line represents average C_4/C_6 value.

Extracrystalline Pt function was less effective in stabilizing rates on BEA-1 (Fig. 1b, BEA-1 + Pt/SiO_2) than on MFI-3 (Fig. 1a, MFI-3 + Pt/SiO_2); extracrystalline Pt also led to larger amounts of C_4 and C_9 (1,3,5-trimethylbenzene (TMB)) products (Fig. 2b and 2c, BEA-1 + Pt/SiO_2) than on MFI samples (Fig. 2a, MFI-3 + Pt/SiO_2). These data indicate that extracrystalline Pt/SiO_2 is insufficient in converting MO into MIBK before the MO undergoes subsequent acid catalyzed reactions, which is unexpected given that the larger channels of the BEA (0.67 nm; Table 1) compared to MFI (0.50 nm; Table 1) would provide for more rapid egression of MO from BEA crystals compared to MFI; although, the intrinsic reactivity of active sites within BEA could be higher than those within MFI, for these subsequent reactions, due to differences in the shape of the confining voids present in the BEA and MFI frameworks (discussed in Section 2.3.6). The presence of intracrystalline Pt clusters, introduced via ion exchange of Pt cations onto BEA (synthesis protocols provided in Section 2.2.1), led to more stable rates (Fig. 1b, Pt/BEA-1 + Pt/SiO_2) and to lower C_4 and C_9 selectivities (Fig. 2b and 2c) than on BEA with only an extracrystalline Pt function. As in the case of MFI-3, initial condensation rates on BEA were not influenced by the presence and location of the Pt function (Fig. 1b). The condensation rates on Pt/BEA-1 + Pt/SiO_2 (473 K, 2.0 kPa acetone, 27 kPa H_2) decreased over time with a first-order

deactivation rate constant (k_d, Eq. 1) of 0.034 $\pm$ 0.007 ks^{-1} and an initial condensation rate of 4.8 $\pm$ 0.3 x 10^{-3} $(Al\ s)^{-1}$.

These initial condensation rates determined for aluminosilicate samples allow rigorous assessments of intrinsic reactivities for condensation on aluminosilicates for the first time. Comparisons of intrinsic reactivities and evaluations of the catalytic consequences of the confining framework require: (1) normalization of the rate by the number of active sites responsible for condensation rates (turnover rates), (2) that measured rates are kinetic and uncorrupted by reactant or product concentrations gradients within aluminosilicate crystals, and (3) assessment of the kinetically-relevant elementary steps for condensation reactions on aluminosilicates of different frameworks to ensure similar mechanistic interpretations of rate constants are applicable.

2.3.2 Titration of protons during acetone condensation and their number and kinetic relevance

The incorporation of Al-atoms within silicate frameworks forms an anionic framework that is charge-balanced by a proton, which acts as a Brønsted acid. Any Al-atoms at non-framework locations act as Lewis acid centers. The H^+/Al ratios in the samples used here are typically slightly smaller than unity (Table 1), leading to the plausible coexistence of Brønsted and Lewis acid centers, both of which have been implicated as active sites in condensation catalysis, either as separate sites or acting in concert to stabilize the relevant transition states [9, 18, 23].

The complete suppression of condensation rates by a selective titrant of Brønsted acid sites, such as a sterically-hindered non-coordinating base (2,6-di-*tert*-butyl pyridine, DTBP), would show that protons are the sole active structures in acetone condensation turnovers. The number of these titrant molecules required to suppress rates would, in turn, give the number of accessible protons during catalysis in each sample [37, 79]. Such titrants can access intracrystalline protons in BEA, FAU, and MCM-41, but not those residing within medium-pore aluminosilicates (MFI, TON, FER), for which alternate titrants or probes are required.

Acetone condensation rates on Pt/BEA-1 + Pt/SiO_2 (1% wt. intracrystalline Pt and 1% wt. extracrystalline Pt), BEA-2 + Pt/SiO_2 (1.3% wt. extracrystalline Pt), and MCM-41 + Pt/SiO_2 (0.66% wt. extracrystalline Pt) decreased monotonically with increasing DTBP uptakes and ultimately reached undetectable rates (Fig. 3). These data show that condensation turnovers occur only on protons without any detectable contributions from any Lewis acid centers that may be present in these samples. These data cannot rule out concerted pathways requiring both types of acid sites, proposed to involve alkenol species bound to non-framework Al sites forming a C-C bond with a protonated species bound at a Brønsted acid site [18, 23]; these concerted pathways require that two Al-atoms are present at close proximity and are inconsistent with measured condensation turnover rates (per proton) that are constant across MFI samples of different proton densities, discussed in Section 2.3.3.

Proton counts from DTBP titrations are similar to those determined from the amount of NH_3 evolved upon heating NH_4-exchanged samples (BEA, FAU; Table 1). This latter method is required to determine proton counts in medium-pore zeolites with channels too small to allow DTBP diffusion (TON, MFI; Table 1). Proton counts of the FER sample were determined by pyridine titration. The FER framework consists of large cage-like structures (0.70 nm diameter, [34]) that are accessible to NH_3 but not acetone (0.50 nm kinetic diameter, [46]) or pyridine. Such cages can only be accessed through small windows (0.33 nm diameter, [47]); as a result only the protons in the channels (0.53 nm diameter, [34]) are accessible to acetone, making pyridine uptakes the appropriate measure of the number of protons in reporting reactivity as turnover rates (FER; Table 1).

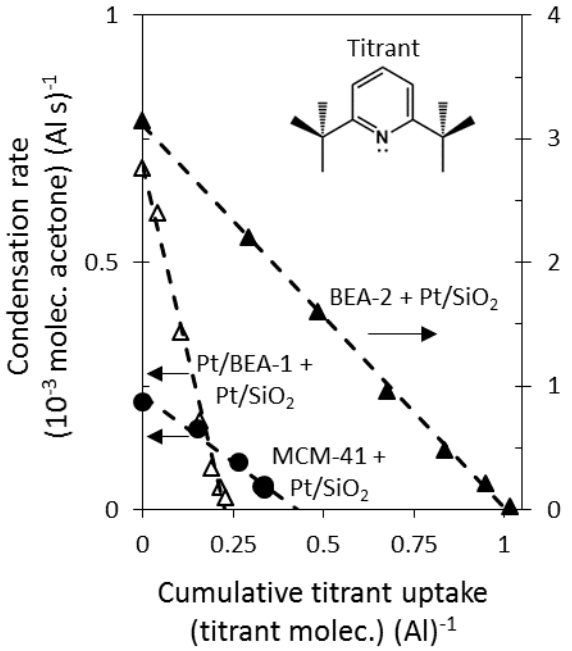

Figure 3: Acetone condensation rates as a function of cumulative 2,6-di-*tert*-butyl pyridine uptakes on Pt/BEA-1 + Pt/SiO_2 (1% wt. intracrystalline Pt and 1% wt. extracrystalline Pt; open triangles), BEA-2 + Pt/SiO_2 (1.3% wt. extracrystalline Pt; closed triangles), and MCM-41 + Pt/SiO_2 (0.66% wt. extracrystalline Pt; closed circles) (473K, 0.3 kPa acetone, 27 kPa H_2, and 0.6-1.2 Pa 2,6-di-*tert*-butyl pyridine). Dashed lines are regressed linear fits of the data.

2.3.3 Mechanistic interpretations of the effects of acetone pressure and reaction temperature on condensation turnover rates

The effects of acetone pressure on condensation turnover rates (per proton) were measured on Pt-containing samples of MFI (MFI-1, MFI-2, MFI-3, and MFI-4), BEA (BEA-1, BEA-2), FAU, MCM-41, FER, and TON; all samples showed first-order deactivation rates constants (k_d, Eq. 1) below 0.05 ks^{-1}. Figure 4 shows these rate data as a function of acetone pressure on MFI-3, BEA-1, and MCM-41 (0.1-5.0 kPa acetone, 473 K). Similar first-order kinetic dependences were observed on the other samples (Fig. S.5, S6, SI) throughout the entire range of acetone pressures

(0.1-5 kPa acetone). Condensation turnover rates (ν) on all catalysts were proportional to acetone pressure (Ac):

$$\nu \equiv \frac{r}{[\mathrm{H^+}]} = k_{eff}(\mathrm{Ac}) \tag{12}$$

with their effective first-order rate constants (k_{eff}) given by the slopes of these linear plots in Figure 4 and Supporting Information, Figure S.5. The k_{eff} values for MFI and BEA samples with a range of intracrystalline proton density are shown in Figure 5.

These k_{eff} values were independent of proton density (0.4-3.5 H^+/unit cell; Table 1), Si/Al ratio (MFI: 17-168, BEA: 12-43; Table 1) or H^+/Al ratio (MFI: 0.65-1.03, BEA: 0.22-1.04; Table 1) for each zeolite framework (MFI and BEA, Fig. 5). These data show that acetone concentrations are uniform throughout zeolite crystals, because any intracrystal gradients would become more severe as the proton density increases causing turnover rates to decrease monotonically with increasing proton density. The constant turnover rates (per proton) on samples with different H^+/Al ratios and thus, relative numbers of Lewis and Brønsted acid sites, indicate that neither Lewis acid sites nor Brønsted-Lewis acid pairs mediate condensation turnovers. Such turnovers are exclusively catalyzed by Brønsted acid sites on these samples. Also, the local void environment around protons in these MFI and BEA samples appears to be independent of Al content, because confinement effects dictated by the local geometric topology of the framework have significant consequences for condensation reactivity, as we describe below (Sections 2.3.5 and 2.3.6).

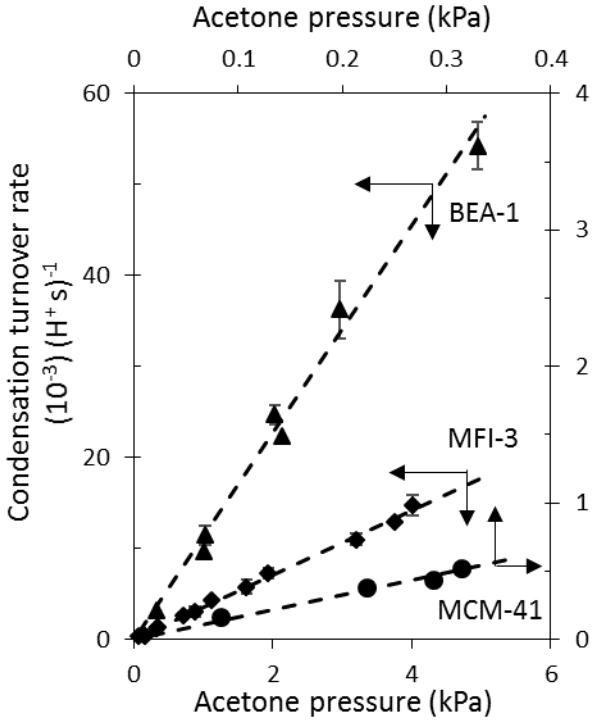

Figure 4: Condensation turnover rate as a function of acetone pressure on Pt/BEA-1 + Pt/SiO_2 (1% wt. intracrystalline Pt and 1% wt. extracrystalline Pt; triangles), MFI-3 + Pt/SiO_2 (1% wt. extracrystalline Pt; diamonds), and MCM-41 + Pt/SiO_2 (0.66% wt. extracrystalline Pt; circles) (473 K, 27 kPa H_2). Dashed lines are regressed fits of rate data to the form of Eq. 12. Bars represent 95% confidence intervals of the extrapolation of rate data to zero conversion.

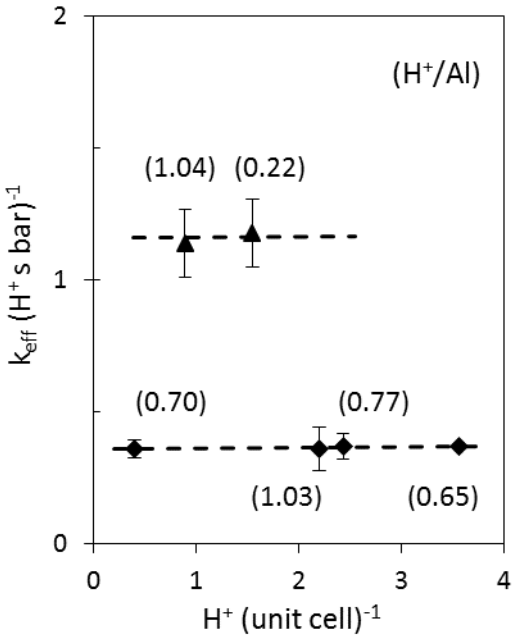

Figure 5: Effective first-order condensation rate constants as a function of proton density (per unit cell) on Pt-containing samples of MFI (diamonds) (MFI-1, MFI-2, MFI-3, MFI-4) and BEA (triangles) (BEA-1, BEA-2) samples (473 K, 0.1-5 kPa acetone, 27 kPa H_2). H^+/Al ratios for all samples are shown in parentheses next to their corresponding rate data point (Table 1). Bars represent 95% confidence intervals of the regressed linear fits of rate data to the form of Eq. 12.

These effects of acetone pressure on condensation turnover rates may reflect two plausible sets of kinetically-relevant transition states and most abundant surface intermediates from the elementary steps shown in (Scheme 3). (1) A kinetically-relevant monomolecular transition state that mediates the activation of acetone bound at low coverages on protons (K_{Ac}(Ac) << 1, Eq. 13); as in the case of DFT treatments that have proposed C_3-alkenol formation as the sole kinetically-relevant step on medium-pore and large-pore aluminosilicates (FER, MFI, MCM-22) [80], which is described by the rate expression:

$$\nu = \frac{k_{taut}(\mathrm{Ac})}{1 + K_{Ac}(\mathrm{Ac})} \approx k_{taut}(\mathrm{Ac}) \tag{13}$$

Here, k_{taut} is the forward kinetic rate constant for Step 3.2 in Scheme 3, and K_{Ac} is the thermodynamic constant for acetone adsorption (Step 3.1, Scheme 3). (2) A kinetically-relevant bimolecular transition state that mediates C-C bond formation via reactions between gaseous acetone and protons saturated with acetone-derived adsorbed species (K_{Ac}(Ac) >> 1, Eq. 14), as shown in Step 3.3 in Scheme 3 with a kinetic rate constant of k_{CC}. This proposal leads to the rate expression:

$$\nu = \frac{k_{CC}K_{taut}K_{Ac}(\mathrm{Ac})^2}{1 + K_{Ac}(\mathrm{Ac})} \approx k_{CC}K_{taut}(\mathrm{Ac}) \tag{14}$$

Scheme 3: Proposed sequence of elementary steps for acetone condensation to C_6-products on Brønsted acid sites

Step		Rate constant*
(3.1)	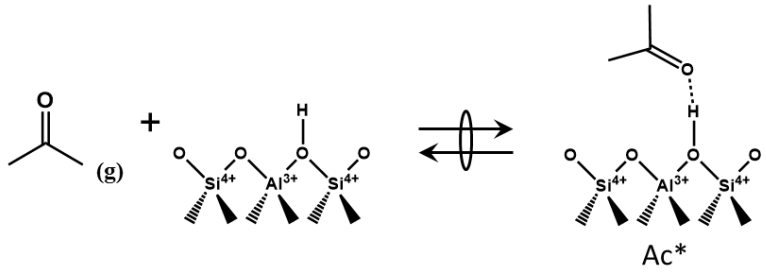	K_{Ac}
(3.2)	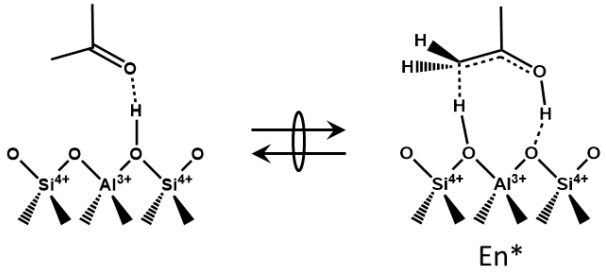	K_{taut}
(3.3)	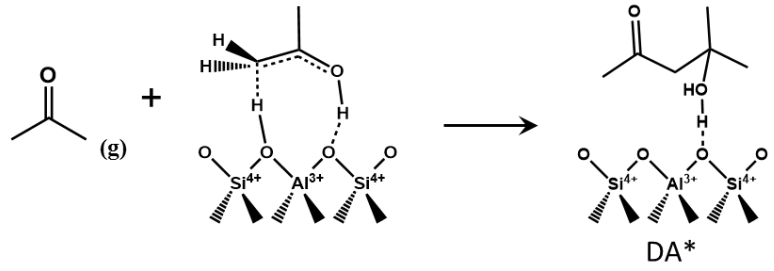	k_{CC}
(3.4)	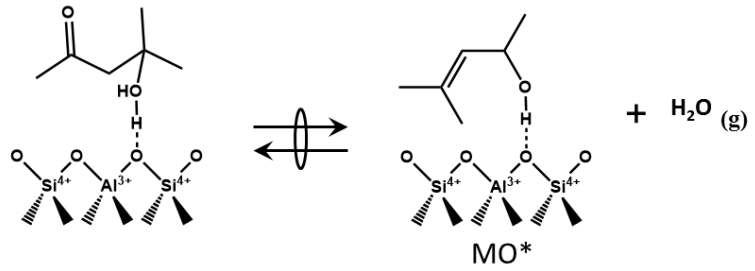	K_{dehyd}

(3.5) 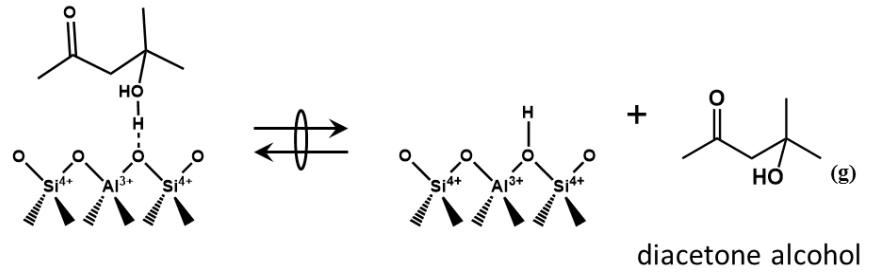 $(K_{DA})^{-1}$

diacetone alcohol

(3.6) 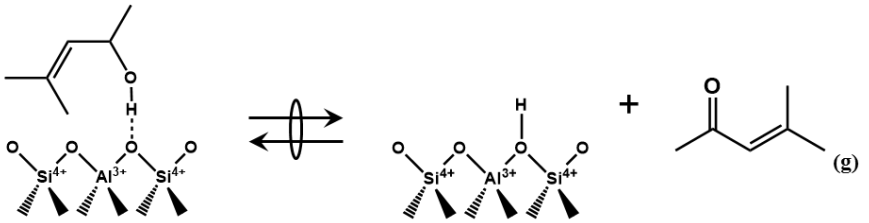 $(K_{MO})^{-1}$

mesityl oxide

(3.7) 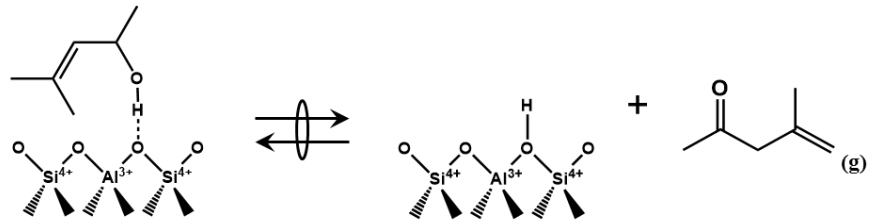 $(K_{IMO})^{-1}$

isomesityl oxide

*k_x and K_x denote kinetic constants for forward steps and equilibrium constants, respectively. Quasi-equilibrated steps are indicated by an open circle over the double arrows.

The infrared spectra of the MFI-3 sample during acetone condensation can be used to probe the coverage of acetone-derived species and the relative contributions of the two plausible most abundant surface intermediates described above. The infrared bands of MFI before condensation reactions (473 K, 100 cm^3 g^{-1} s^{-1} He, UHP, Praxair) showed an O-H stretch at 3600 cm^{-1} (Fig. 6, inset), consistent with DFT-derived frequencies for acidic O-H groups (3440-3660 cm^{-1}, Table 2, VASP, RPBE + D3BJ and vdW-DF2) and with previous studies [81, 82]. The presence of acetone at reaction temperatures (473 K, 0.04 kPa acetone, 100 cm^3 g^{-1} s^{-1} He flow) led to the disappearance of the acidic O-H band and to a new band centered at 2360 cm^{-1} (2110-2650 cm^{-1}; Fig. 6). This new band corresponds to H-bonding interactions that weaken the acidic O-H bond, as shown by DFT-derived frequencies of H-bonded acetone at acidic O-H groups on MFI (2259-2455 cm^{-1}, Table 2, VASP, vdW-DF2) and by previous infrared studies of acetone adsorption on MFI [83, 84]. Contact with acetone also led to new bands at 2800-3000 cm^{-1} (Fig. 6), which correspond to C-H stretches in the CH_3-groups of gaseous acetone [85] and H-bonded acetone molecules. DFT-derived C-H stretching frequencies in H-bonded acetone appeared between 2950 cm^{-1} and 3080 cm^{-1} (Table 2, VASP, vdW-DF2; 2980-3120 cm^{-1}, RPBE + D3(BJ)).

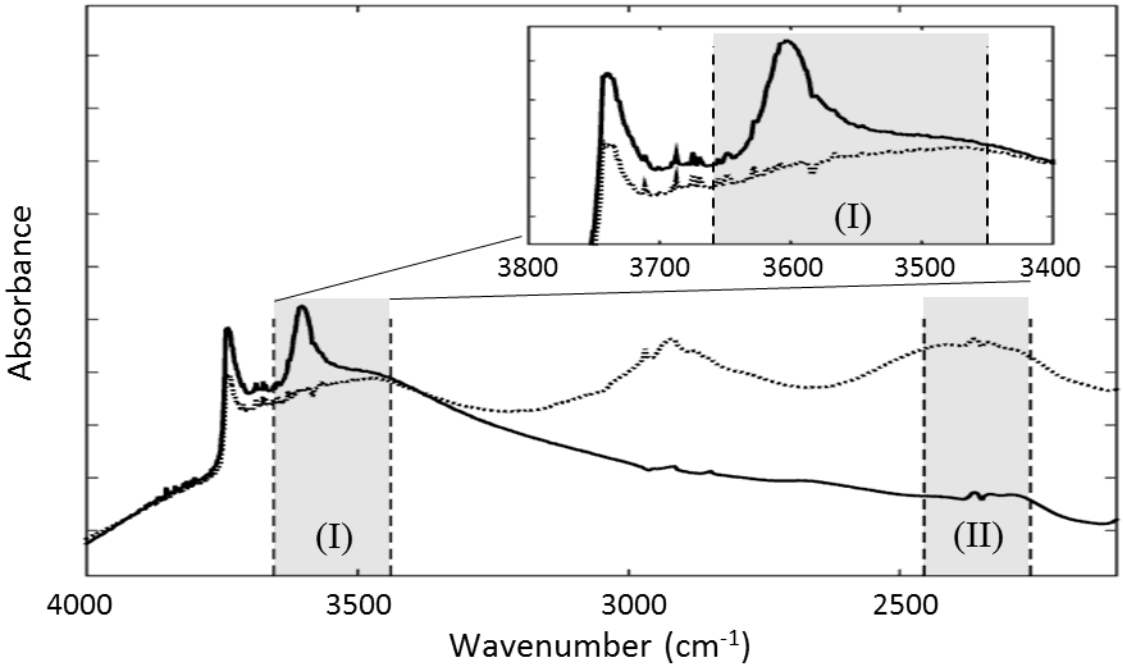

Figure 6: Infrared spectra of MFI-3 before contact with acetone (473 K, 6000 cm^3 g^{-1} s^{-1} He; solid line) and during acetone condensation (473 K, 0.04 kPa acetone, 6000 cm^3 g^{-1} s^{-1} He; dashed line). The shaded regions denote ranges of DFT-calculated frequencies for acidic O-H stretches (I) when unperturbed (3440-3655 cm^{-1}; Table 2) and (II) when H-bonding with acetone (2260-2455 cm^{-1}; Table 2, VASP, vdW-DF2, PAW5).

These spectra and the favorable DFT-derived adsorption free energies ($\langle \Delta G_{H-Ac} \rangle$), ensemble-averaged at the three framework O-atoms ($O_{zeolite}$) vicinal to the T12 site in MFI that are accessible to acetone (-80 and -79 kJ mol^{-1} using RPBE + D3(BJ) and vdW-DF2, respectively; Table 2), show that protons are nearly saturated with H-bonded acetone during condensation catalysis at all conditions (θ_{Ac} = 1.0, 0.04-5 kPa acetone, 463-483 K; Eq. 10). These data are consistent with the interpretation of the rate data by Equation 14 and with K_{Ac}(Ac) values much larger than unity. DFT-derived structures, listed in Table 2, give H-bonded acetone without proton transfer from $O_{zeolite}$. The $O_{zeolite}$-H^+ bonds (0.110 nm; RPBE + D3(BJ), Table 2) are shorter than the O_{Ac}-H^+ bonds (0.136 nm; RPBE + D3(BJ), Table 2) and the $O_{zeolite}$-H^+-O_{Ac} bond angle is almost 180° (174°, Table 2); these geometries are those expected of H-bonding [86] instead of proton transfer.

Table 2: DFT estimates for bond distances (nm), bond angles (degrees), bond stretching frequencies (cm^{-1}), and Gibbs free energies (kJ mol^{-1}) for the bare proton and H-bonded acetone species at each O-atom vicinal to the T12 Al-site in MFI framework

DFT Functional:	**RPBE + D3(BJ)**				**vdW-DF2**			
$(O_{zeolite})$[a] :	O20	O11	O24	O12[b]	O20	O11	O24	O12[b]
bare proton								
$O_{zeolite}$-H^+	0.098	0.097	0.098	0.098	0.098	0.097	0.098	0.099
$\nu(O_{zeolite}$-$H^+)$	3613	3650	3570	3518	3629	3658	3594	3439
$P_{H^+-O_Z}$[c]	0.14	0.66	0.05	0.15	0.16	0.74	0.03	0.07
H-bonded acetone								
$O_{zeolite}$-H^+	0.110	0.110	0.111		0.105	0.104	0.105	
O_{Ac}-H^+	0.136	0.136	0.137		0.153	0.154	0.152	
$O_{zeolite}$-O_{Ac}	0.246	0.248	0.247		0.256	0.258	0.256	
C=O_{Ac}	0.125	0.125	0.125		0.125	0.125	0.125	
∠ $O_{zeolite}$-H^+-O_{Ac}	171.2	175.0	173.3		166.0	171.2	170.7	
∠ C=O_{Ac}-H^+	121.0	121.2	121.2		129.5	128.6	127.5	
$\nu(O_{zeolite}$-$H^+)$	1843	2020	1820		2378	2455	2259	
$\nu(C_{Ac}$-$H_{Ac})$	3120	3119	3116		3067	3076	3068	
	3109	3107	3113		3052	3065	3061	
	3065	3052	3068		3015	3003	3016	
	3056	3039	3047		3007	2993	2996	
	2998	2990	2991		2971	2964	2964	
	2986	2981	2985		2962	2956	2949	
(ΔG_{Ac*})[d]	-78	-83	-80		-82	-75	-90	
$\langle \Delta G_{Ac*} \rangle$[e]	———	-82	———		———	-79	———	
θ_{Ac}[f]	———	1.00	———		———	1.00	———	

[a] Framework O-atoms ($O_{zeolite}$) numbered according to convention [61] (Scheme 2)
[b] H^+-O12 is inaccessible to acetone
[c] Probability of proton at each $O_{zeolite}$ based on Gibbs free energy, Eq. 7 (473 K)
[d] Free energy of acetone binding, Eq. 5 (473 K, standard pressure of acetone)
[e] Ensemble-averaged free energy, Eq. 6. (473 K, standard pressure of acetone)
[f] Acetone coverage, Eq. 10 (473 K, 4 x 10^{-4} bar acetone, conditions as in Fig. 6)

The two proposed rate expressions, listed above (Eq. 13 and 14), are also mediated by transition states that differ in the number of forming and breaking H-bonds; thus, these proposals are expected lead to different H/D kinetic isotope effects (KIE; Eq. 2). Measured rates of acetone-d_0/H_2 and acetone-d_6/D_2 were nearly identical on MFI-3 (0.98 $\pm$ 0.03 KIE, 473K; SI, S7, Fig. S.6). These rate data are inconsistent with the mechanistic interpretation of Equation 13 where the kinetically-relevant step involves proton transfer to the O-atom in acetone and concurrent proton transfer from the CH_3 group in acetone to another framework O-atom (Step 3.2, Scheme 3), which leads to a DFT-derived KIE value of 2.1 for acetone-d_6 (473 K, Al T12 site, MFI, VASP, RPBE +

D3(BJ)). This would be the KIE value from experiments if alkenol formation is the kinetically-relevant step.

These kinetic, spectroscopic, and isotopic data therefore show that C-C bond formation rates are limited by reactions of gaseous acetone with H-bonded acetone species, which are in quasi-equilibrium with gaseous acetone; this elementary step is mediated by a bimolecular transition state that resembles a C_3-alkenol, in quasi-equilibrium with H-bonded acetone, incipiently forming a C-C bond with a protonated acetone (Step 3.3, Scheme 3). Such steps do not involve the formation or cleavage of C-H or O-H bonds and would not therefore exhibit primary isotope effects. The DFT-derived KIE values (1.1 KIE; 473 K, T12 site, MFI, RPBE + D3(BJ)) agree with measured data (0.98 $\pm$ 0.03 KIE; 473K, MFI-3). Consequently, k_{eff} (Eq. 12) reflects the rate constant in Equation 14 for protons saturated with H-bonded acetone during condensation reactions:

$$\nu = (k_{CC}K_{taut})(\mathrm{Ac}) \tag{15}$$

where k_{CC} and K_{taut} are kinetic and thermodynamic constants representing the elementary step for C-C bond formation and acetone tautomerization, respectively (Scheme 3). These constants are in turn related to the free energy barrier of Step 3.3 in Scheme 3 using Equation 8 and the thermodynamic free energy difference between a H-bonded acetone and a H-bonded C_3-akenol using Equation 9:

$$k_{CC}K_{taut} = \frac{k_B T}{h}\exp\left(-\frac{G_{CC}^{\ddagger} - (G_{En*} + G_{Ac})}{k_B T}\right)\exp\left(-\frac{G_{En*} - G_{Ac*}}{k_B T}\right) \tag{16}$$

Here, G_i represents the free energy of each species (i = *CC*, *En**, *Ac**, *Ac* denotes C-C bond formation transition states, H-bonded C_3-alkenol, H-bonded acetone, and gaseous acetone, respectively). This equation can be simplified by combining the exponents to give:

$$k_{CC}K_{taut} = \frac{k_B T}{h}\exp\left(-\frac{G_{CC}^{\ddagger} - (G_{Ac*} + G_{Ac})}{k_B T}\right) \tag{17}$$

Equation 17 shows that the first-order rate constant ($k_{CC}K_{taut}$) reflects differences in Gibbs free energy (ΔG) between the C-C bond formation transition state and its two relevant precursors, a H-bonded and a gaseous acetone. The experimental free energy barrier on MFI-3 is 122 $\pm$ 9 kJ mol^{-1} (Eq. 19, MFI-3 + Pt/SiO_2, Fig. 4) and can be partitioned into its enthalpic (ΔH) and entropic (ΔS) components:

$$k_{CC}K_{taut} = \frac{k_B T}{h}\exp\left(-\frac{\Delta H - T\Delta S}{k_B T}\right) \tag{18}$$

The experimental activation enthalpy and entropy barriers are 20 ± 6 kJ mol^{-1} and -213 ± 10 J (mol K)$^{-1}$, respectively, as obtained by regression of $k_{CC}K_{taut}$ values measured at different reaction temperatures to the form of Equation 19 (463-483 K, MFI-3 + Pt/SiO_2, Fig. 7). The free energy and enthalpy barriers allow further investigation of the kinetic relevance of plausible elementary steps by comparing their values from experiment and theory as discussed in Section 2.3.4.

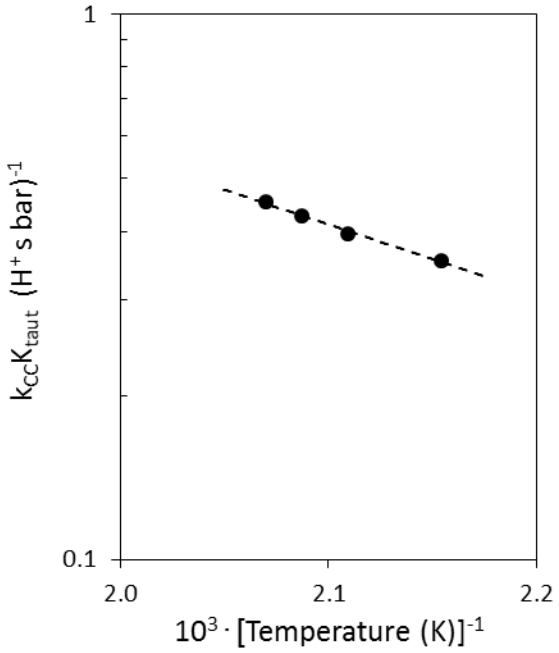

Figure 7: First-order condensation rate constant as a function of reaction temperature on MFI-3 + Pt/SiO_2 (1% wt. extracrystalline Pt; 463-483 K, 0.3-1 kPa acetone, 27 kPa H_2). Dashed line represents regressed fit to the form of Eq. 18.

2.3.4 Theoretical assessment of intermediates and transition states involved in acetone condensation

The reaction coordinate in Figure 8 involves the initial elongation of the α-C-H bond in H-bonded acetone via interactions with framework oxygens vicinal to the proton to form a bound alkenol-like species mediated by TS1 (Fig. 9). The presence of alkenol-type species has been proposed based on ^{1}H-NMR evidence of the exchange of adsorbed acetone-d_6 with acidic OH groups in MFI and of adsorbed ^{13}C-2-acetone with OD groups in MFI [87]. The DFT-derived energies in Figure 8 shows that these species form with barriers (ΔG = 60 kJ mol^{-1} and ΔH = 13 kJ mol^{-1}, Fig. 8) much smaller than measured values (ΔG = 122 ± 9 kJ mol^{-1} and ΔH = 20 ± 6 kJ mol^{-1}) and those DFT-derived for the later steps along the reaction coordinate (Fig. 8). The return of C_3-alkenol species to its H-bonded acetone is nearly barrierless (2 kJ mol^{-1}, Fig. 8) [80] compared to the forward barrier along the reaction coordinate to react with acetone and form TS2 (60 kJ mol^{-1}, Fig. 8), consistent with the C_3-alkenol being quasi-equilibrated with acetone (Step

3.2, Scheme 3). Therefore, C_3-alkenol species represent a kinetically-irrelevant 'ledge' along the climb from the reactants to the kinetically-relevant transition state (TS2, Fig. 8).

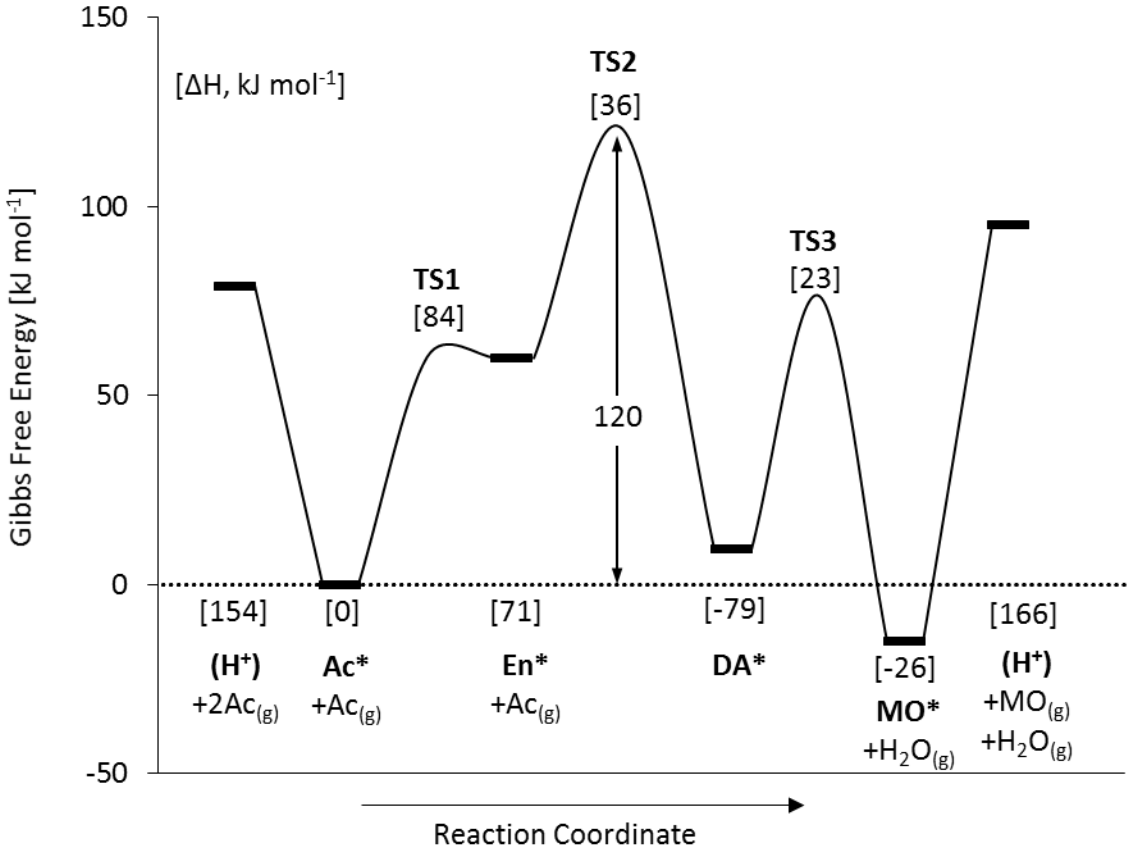

Figure 8: Gibbs free energy diagram for acetone condensation on MFI at 473 K and standard pressure (1 bar) for all gaseous species calculated by DFT, VASP, RPBE+D3(BJ) (methods are described in Section 2.2.5). Enthalpy of each state, referenced to H-bonded acetone and gaseous acetone, shown in square brackets. Labelling corresponds to the notation in Scheme 3.

The formation of the C-C bond (Step 3.3, Scheme 3) is mediated by a bimolecular transition state (TS2, Fig. 9) that resembles a protonated acetone and a C_3-alkenol in quasi-equilibrium with H-bonded acetone. This transition state is an ion-pair requiring the framework to accept 0.83 e^- charge (QUAMBO analysis discussed in Section 2.2.6), and the incipiently-formed C-C bond is much longer (0.257 nm) at TS2 than in the product state (protonated diacetone alcohol; 0.154 nm). The DFT-derived free energy and enthalpy barriers to form TS2 from H-bonded acetone and gaseous acetone are, respectively, 120 kJ mol^{-1} and 36 kJ mol^{-1}, in reasonable agreement with measured barriers ($\Delta G = 122 \pm 9$ kJ mol^{-1} and $\Delta H = 20 \pm 6$ kJ mol^{-1}).

DFT treatments show that the subsequent dehydration of the diacetone alcohol to MO (Step 3.6, Scheme 3) involves proton transfer and occurs via an E1-type elimination route mediated by

a transition state (TS3, Fig. 9) similar to protonated MO and H_2O, where the C-H bond in the CH_3-group of MO is cleaved, forming isomesityl oxide and $[H_3O]^+$. The calculated free energy and enthalpy barriers required to form TS3 from the relevant precursors are 76 kJ mol^{-1} and 23 kJ mol^{-1}, respectively. This free energy barrier to form TS3 is smaller (by 44 kJ mol^{-1}; Fig. 8) than that estimated for TS2, and thus, the reverse barrier for diacetone alcohol to return to acetone is larger than the forward barrier for dehydration, consistent with the quasi-equilibrated dehydration of the diacetone alcohol intermediates to MO.

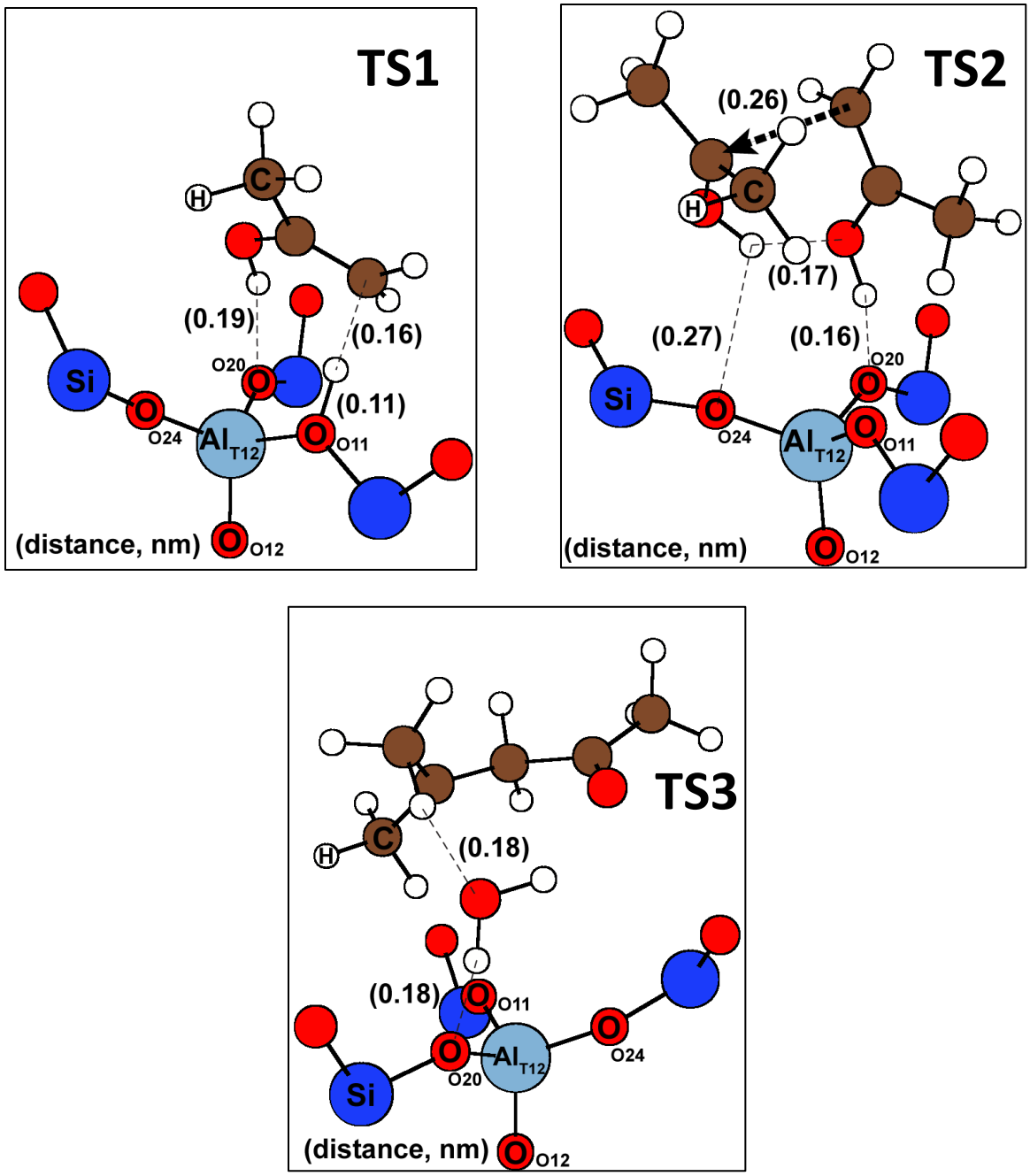

Figure 9: Structures of transition states that mediate enol formation (TS1), C-C bond formation (TS2), and diacetone alcohol dehydration (TS3) on MFI. Transition state labelling corresponds to the notation in Figure 8; atom labelling corresponds to that in Scheme 2. (DFT, VASP, RPBE + D3(BJ)). Dashed lines represent interactions between molecules and the zeolite framework, and distances between atoms involved in these interactions are provided in parentheses (nm). The dashed arrow shown on TS2 represents the forming C-C bond.

These theoretical estimates show that the free energy difference between TS2 and its relevant H-bonded acetone and gaseous acetone precursors represents the only relevant barrier in

determining reactivity (Eq. 17). The mechanistic interpretations of kinetic, isotopic, and spectroscopic data and their confirmation by DFT treatments presented here provide the guidance required to assess the catalytic consequences of the void environment surrounding the active protons. Such environments affect the reaction barrier through van der Waals contacts with the relevant species, TS2 and H-bonded acetone, based on their size and shape.

The catalytic consequences of void size and shape first require a geometric assessment of such properties for H-bonded acetone and TS2; here these properties are determined from the van der Waals atomic diameters and the concomitant molecular volumes (V_{vdW}) of each moiety using an ellipsoidal shape:

$$V_{vdW} = \frac{4}{3}\pi\left(\frac{d_x}{2} + \frac{d_y}{2} + \frac{d_z}{2}\right)^3 \tag{19}$$

where d_i (i = x, y, z) are the largest dimensions across the organic moiety in three orthogonal directions (Fig. 10). This volume is then related to a characteristic molecular diameter (d_C):

$$d_C = 2\left(\frac{3}{4}\pi V_{vdW}\right)^{1/3} \tag{20}$$

given as that of a sphere of volume V_{vdW}. The V_{vdW} and the d_C values for DFT-derived structures (MFI, Al T12 site, VASP, RPBE + D3(BJ)) are, respectively, 0.182 nm^3 and 0.704 nm for TS2, and smaller (0.085 nm^3 and 0.545 nm; Fig. 10) for H-bonded acetone. Such differences in size are expected to influence the stabilization of these organic moieties by van der Waals interactions as confining voids approach these molecular dimensions.

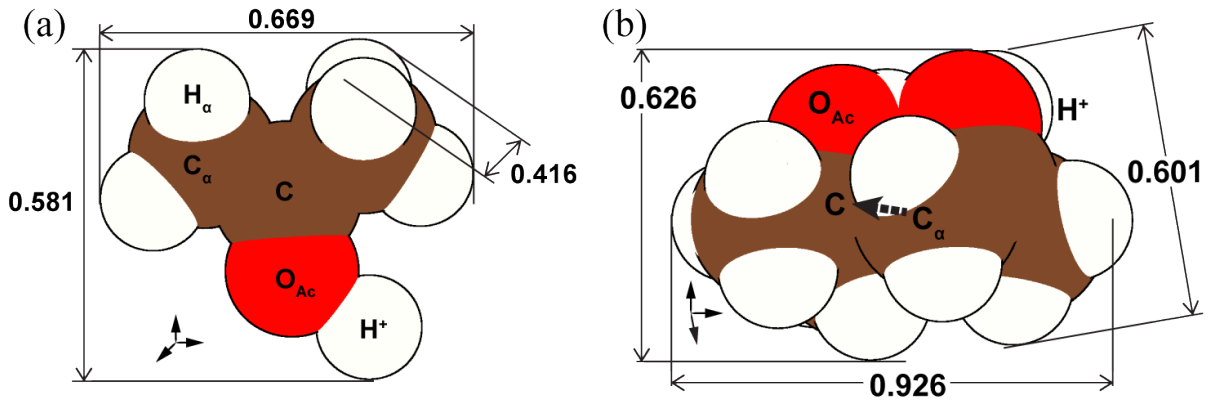

Figure 10: DFT-estimated size of (a) H-bonded acetone (Scheme 2) and (b) the C-C bond formation transition state (TS2, Fig. 9), distances are provided in nm (MFI, Al T12 site, VASP, RPBE + D3(BJ)) atom labelling corresponds to that in Scheme 2. Atom sizes reflect their respective van der Waals radii [88]. The dashed arrow in (b) denotes the forming C-C bond.

2.3.5 Effects of local void environment on acetone condensation turnover rates

Measured condensation turnover rates (per accessible proton) increased linearly with increasing acetone pressure on all aluminosilicates (Fig. 4: MFI, BEA, MCM-41; SI, S6 Fig. S.5: FER, TON, FAU) suggesting that kinetically-relevant steps and the chemical interpretation of the rate constants ($k_{CC}K_{taut}$; Eq. 15) are similar on these aluminosilicates. These rate constants are determined by free energy barriers (Eq. 17 and Fig. 8) that are sensitive to the nature of the active protons, reflecting the ability of the local coordination environment to distribute charge (acid strength) and any van der Waals stabilization conferred by confinement. Reactivity reflects such properties specifically because the charge and size of TS2 differ significantly from those of its relevant H-bonded acetone precursor. The strength of a Brønsted acid reflects the stability of the conjugate anion formed upon deprotonation; the extent of deprotonation, and thus the actual charge on the conjugate anion, differ in TS2 and H-bonded acetone, leading to their different sensitivity on acid strength, (discussed in Section 2.3.7). The conjugate anion stability in the fully-deprotonated acid depends, in turn, on composition and local coordination, making acid sites in all aluminosilicates exhibit similar strength [12]. Aluminosilicates vary quite significantly, however, in the nature of the void environment surrounding protons and thus surrounding transition states and intermediates (Fig. 11).

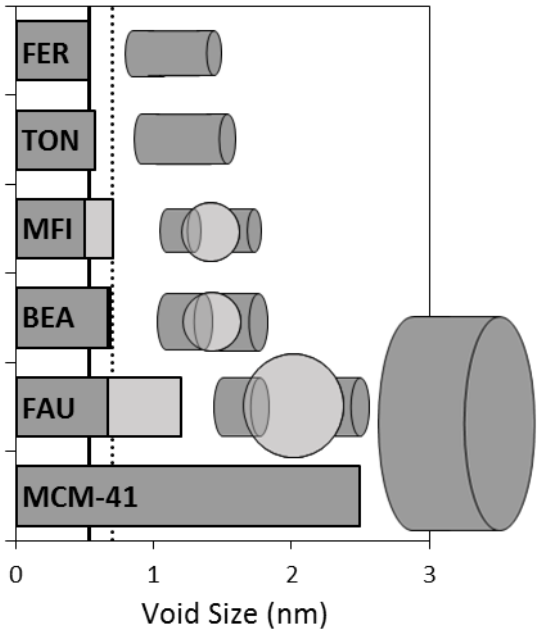

Figure 11: Channel (darker gray) and intersection (lighter gray) void sizes accesible to acetone for aluminosilicate frameworks (Table 1). Vertical lines represent the DFT-estimated diameters (d_C; Eq. 20) of H-bonded acetone (solid) and TS2 (dotted; MFI, Al T12, VASP, RPBE + D3(BJ); Fig. 10). Schematic depictions of framework sizes are provided to the right of each bar, where cylinders represent the framework channels (pore-limiting diameter) and spheres (largest cavity diameter) represent their intersections (Table 1).

$k_{CC}K_{taut}$ values, determined from the slope of the rate data shown in Figures 4 and S.5 (SI, S6), on MCM-41 and FAU are similar (Fig. 12), indicating that their void environments are much larger than TS2 and H-bonded acetone and therefore stabilize the organic moieties (TS2 and H-bonded acetone) to the same extent. $k_{CC}K_{taut}$ values increased as the size of the confining voids became similar those of TS2 (BEA, MFI; Fig. 12), reflecting the preferential stabilization of TS2 relative to its smaller H-bonded acetone precursors (Fig. 10) and the concomitant decrease in the relevant free energy barriers. $k_{CC}K_{taut}$ values decreased sharply as the voids became smaller than those in BEA and MFI (TON, FER; Fig. 12). Such small voids increase free energies through the preferential stabilization of H-bonded acetone over larger TS2 (discussed in Section 2.3.6).

The kinetic constants ($k_{CC}K_{taut}$) determined for aluminosilicates with different void environments, taken together with the DFT-simulated sizes of the kinetically-relevant species and transition states (Fig. 12) shows that void size accurately describes the consequences of confinement on Gibbs free energy barriers. The significant residual differences in the $k_{CC}K_{taut}$ values for voids of similar size as their size approaches those of TS2 (BEA, MFI; Fig. 12), however, illustrates the incomplete nature of the largest accessible cavity diameter, used here to account for void size, as a descriptor of stabilization by confinement. The frameworks used here contain diverse and asymmetric voids (Table 1); such as the MFI and FER frameworks that have larger voids connected via smaller channels as shown by comparisons of their largest cavity diameter and their pore limiting diameter (Table 1). These diverse void environments present in each framework interact differently with the transition state and H-bonded acetone, and thus require more than a single framework dimension to describe the consequences of van der Waals stabilization on reactivity.

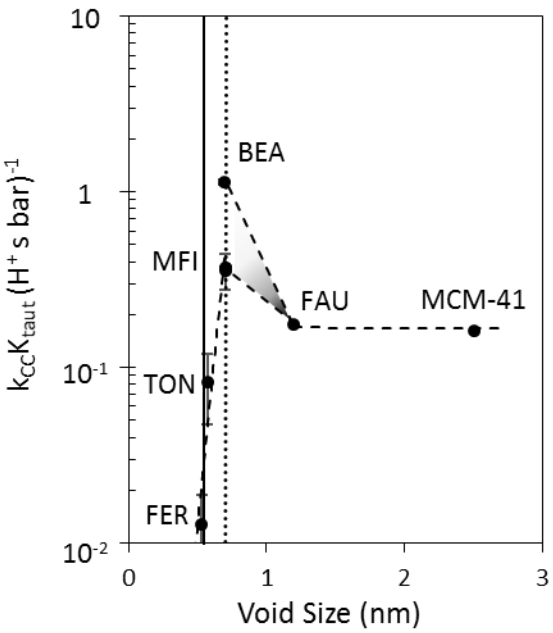

Figure 12: First-order acetone condensation rate constants (473 K, 0.1-5 kPa acetone, 27 kPa H_2) as a function of aluminosilicate void size (largest accessible cavity diameter; Table 1). All samples contain Pt (amount and location of Pt provided in Fig. 4 for MFI, BEA, MCM-41 and SI, 2.6.7 for FER, TON, and FAU). Bars represent 95% confidence intervals of the regressed linear fits of rate data to the form of Eq. 12. Vertical lines represent the DFT-estimated diameters (d_C; Eq. 20) of H-bonded acetone (solid) and TS2 (dotted) (MFI, Al T12, VASP, RPBE + D3(BJ); Fig. 10). Dashed lines through data points are connecting data points.

2.3.6 New and more complete descriptors of confinement stabilization within voids of molecular dimensions

A more accurate description of van der Waals interactions requires the enumeration of the distances between each framework atom and each atom in the confined organic moieties [43]. Here, a thermochemical cycle (Scheme 4) is first used to dissect the components of each energy into their convenient energetic contributions; the hypothetical steps are arbitrary, because of the path-independent properties of thermodynamic state functions and the thermodynamic underpinnings of transition state theory [35, 39]. The Born-Haber cycle in Scheme 4 describes the apparent energy barrier (ΔE^{TS2}), corrected for zero-point energy and thermal contributions, as:

$$\Delta E^{TS2} = \left(-E_{\text{int}}^{Ac*}\right) + \Delta E_{\text{prot}}^{TS2} + E_{\text{int}}^{TS2} \tag{21}$$

Here, E_{int}^{Ac*} and E_{int}^{TS2} represent the interaction energies of H-bonded acetone and TS2 with the conjugate anion and the surrounding void environment, respectively, and $\Delta E_{\text{prot}}^{TS2}$ represents the energy gained by allowing the gaseous analogue of H-bonded acetone to react with a gaseous acetone to form TS2 as a gaseous molecule (Scheme 4).

Scheme 4: A thermochemical cycle depicting the activation barrier to form TS2 from H-bonded acetone and gaseous acetone (ΔE^{TS2}) as the reverse of the interaction energy of H-bonded acetone with the conjugate anion ($-E_{\text{int}}^{Ac*}$), the energy required to form a gaseous TS2 cation from gaseous acetone and gaseous H-bonded acetone cation ($\Delta E_{\text{prot}}^{TS2}$), and the interaction energy of TS2 cation with the conjugate anion (E_{int}^{TS2}).[a]

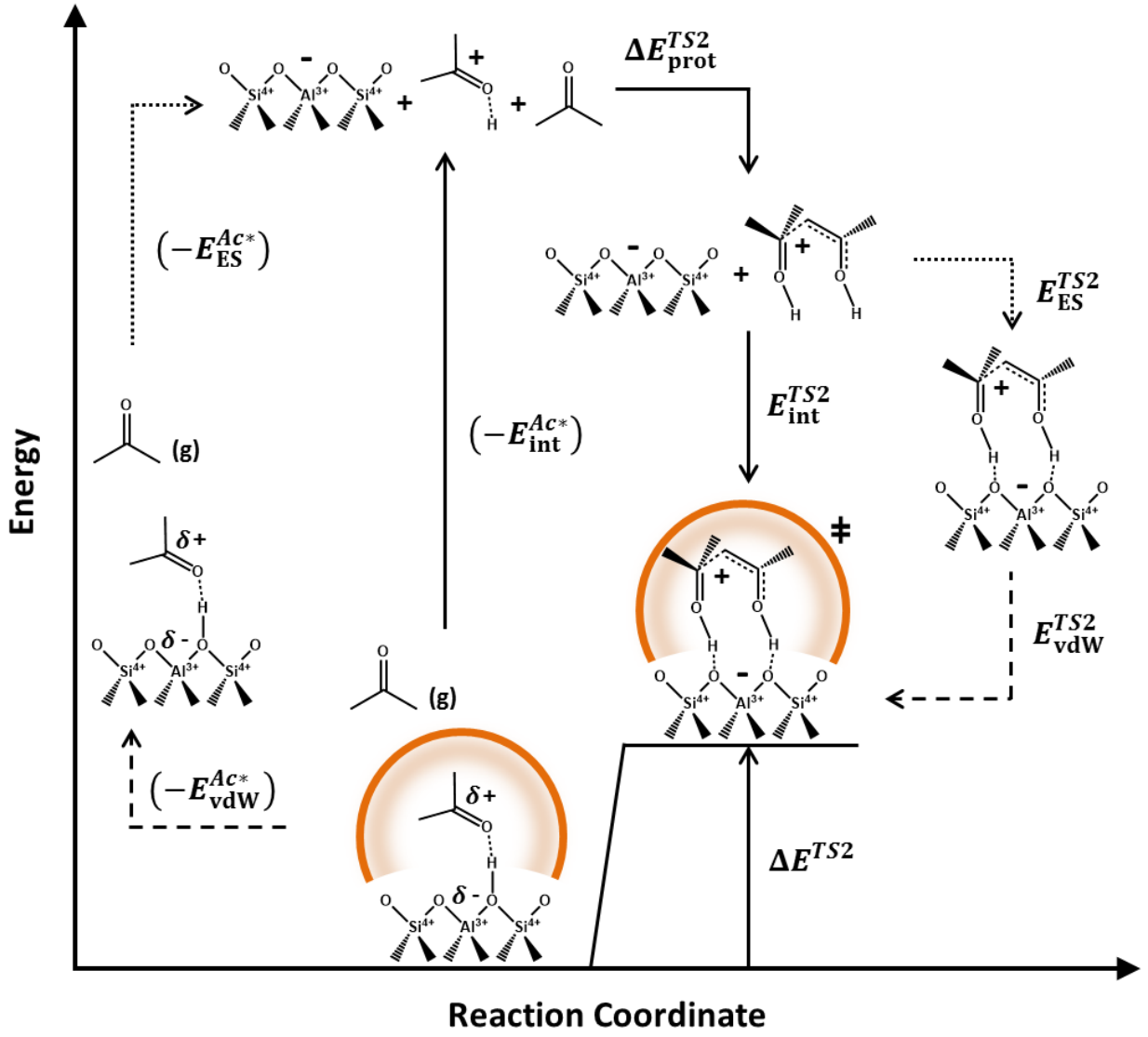

[a] Total interation energies (solid arrows) are separated into electrostatic (ES; dotted arrows) and van der Waals (vdW; dashed arrows) interaction components.

The interaction energies for TS2 and H-bonded acetone (E_{int}^{X}; X = *Ac** or *TS2*) can themselves be dissected into two components:

$$E_{\text{int}}^{X} = E_{\text{ES}}^{X} + E_{\text{vdW}}^{X} \tag{22}$$

where E_{ES}^{X} is the electrostatic interaction energy, representing the interactions between the cationic organic moiety and the conjugate anion due to the separation of charge [38] and E_{vdW}^{X} is the van der Waals interaction energy representing the dispersive interactions between the organic moiety and the framework (discussed below).

The consequences of confinement for reactivity and activation barriers were examined by using this thermochemical construct (Scheme 4). The value of $\Delta E_{\mathrm{prot}}^{TS2}$ reflects catalyst-independent properties of gaseous species. The values of E_{ES}^{X} for TS2 and H-bonded acetone depend on acid strength, a catalyst property that is similar among protons of aluminosilicates (discussed in Section 2.3.5). As a result, the E_{vdW}^{X} values for TS2 and H-bonded acetone (ΔE_{vdW}) are the only terms in Equation 21 (given by Eq. 22) that depend on stabilization by the confining voids:

$$\Delta E_{\mathrm{vdW}} = E_{\mathrm{vdW}}^{TS2} - E_{\mathrm{vdW}}^{H-Ac} \tag{23}$$

These ΔE_{vdW} values rigorously account for the confinement effects for bound structures at each T-site location within a given framework structure.

We calculate ensemble-averaged ΔE_{vdW} values ($\langle \Delta E_{\mathrm{vdW}} \rangle$), exponentially averaging the van der Waals stabilization energies at each distinct Al T-site location of a given framework:

$$\langle \Delta E_{\mathrm{vdW}} \rangle = -k_B T \ln \left(\sum_{i}^{N_{\mathrm{T-site}}} \exp\left(-\frac{\Delta E_{\mathrm{vdW},i}}{k_B T} \right) \mathrm{P}_{\mathrm{T-site},i} \right) \tag{24}$$

$N_{\text{T-site}}$ is the number of crystallographically-distinct T-site locations in the framework; $\Delta E_{\text{vdW},i}$ represents the difference in van der Waals interaction energy between the transition state and the precursors at each T-site, i; and $\mathrm{P}_{\text{T-site},i}$ represents the probability of an Al-atom located at each T-site. These averaging methods allow rigorous comparisons between measured rate constants and calculated barrier values (similar to Eq. 6), providing a more complete description of how the size and shape of the organic species and the framework determine the effectiveness of van der Waals interactions (confinement).

E_{vdW}^{X} values contain only interactions between the atoms of the organic moiety and the framework atoms and, here, these values are estimated by using empirical dispersive energy corrections (DFT-D3) [32, 33]. D3-methods provide an estimate of the attractive interactions between all of the atoms within a structure with each other; therefore, calculating only those interactions between the atoms of the organic moiety and the framework atoms (E_{D3}^{X}) require:

$$E_{\mathrm{D3}}^{X} = E_{\mathrm{D3}}^{X+Z} - \left(\mathrm{E}_{\mathrm{D3}}^{Z} + E_{\mathrm{D3}}^{X_{(g)}} \right) \tag{25}$$

where, E_{D3}^{X+Z} is the D3-correction for the DFT-optimized structure of the organic moiety within the zeolite void (*X* = *Ac** or *TS2* denotes H-bonded acetone or TS2, respectively; *Z* denotes zeolite), $\mathrm{E}_{\mathrm{D3}}^{Z}$ is the D3-correction for the zeolite framework where the organic moiety has been removed from the DFT-optimized structure of the organic moiety within the zeolite void, and $E_{\mathrm{D3}}^{X_{(g)}}$ is the D3-correction for the gaseous analog of the organic moiety. These D3-corrections consider only the attractive dispersive forces between atoms; thus, full DFT simulations are required to generate meaningful structures of the transition state and H-bonded acetone precursor at each distinct T-site within each framework, and thus, these D3-methods be used only after these DFT-optimized structures are determined.

E_{vdW}^{X} values are, alternatively, estimated using the crystal structures of each zeolite framework (FER, TON, MFI, BEA, FAU) [42, 61] and placing DFT-derived structures of the transition state (TS2) and H-bonded acetone (DFT-optimized at the T12 site in MFI; Fig. 10), at each of the T-site locations within each framework (discussed in Section 2.2.6). The van der Waals interaction energies were determined for the resulting structures by individual contributions of Lennard-Jones interactions [69, 70] between each atom in the organic moiety ($\mathrm{X_M}$) and each framework oxygen ($\mathrm{O_Z}$):

$$E_{\mathrm{LJ}}^{X} = \sum_{i}^{O_Z} \sum_{h}^{X_M} \epsilon \left(\left(\frac{d_{eq}}{d_{i,h}} \right)^{12} - 2 \left(\frac{d_{eq}}{d_{i,h}} \right)^{6} \right) \tag{26}$$

These two-atom interaction potentials contain both attractive and repulsive terms and depend on the distance between each *h* atom in the organic moiety and each *i* atom in the framework ($d_{i,h}$) and the equilibrium distance between each atom-pair (d_{eq}), defined here as the sum of their van der Waals radii (O: 0.152 nm, H: 0.120 nm, C: 0.170 nm) [88]. $d_{i,h}$ values smaller than 0.15 nm, such as the proton of H-bonded acetone (Scheme 2), were considered covalent bonds and the resulting two-atom interaction potential was neglected. These two-atom potentials also depend on a scaling factor, denoted here as ε, which was determined by benchmarking E_{LJ}^{X} values (Eq. 26) against E_{D3}^{X} values (Eq. 25) calculated for a set of DFT-optimized structures (Fig. 13).

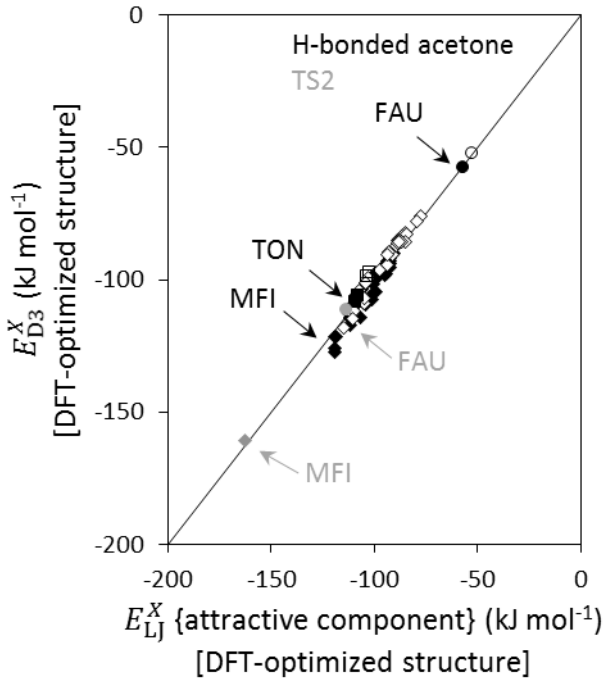

Figure 13: D3 dispersive energy corrections of optimized DFT-structures (Eq. 25) as a function of E_{LJ} values of optimized DFT-structure. Structures of H-bonded acetone (black) and TS2 (gray) in MFI (diamonds), TON (squares), and FAU (circles) frameworks optimized with RPBE + D3(BJ) (filled) and RPBE (open, only H-bonded acetone). $E_{\mathrm{vdW},j}$-values calculated with ε = 1.59 kJ mol^{-1} , Eq. 25. Solid line is a parity line.

Comparisons of E_{D3}^{X} values and E_{LJ}^{X} values require that only the attractive components of E_{LJ}^{X} values (two-atom potentials < 0) are used because E_{D3}^{X} values only reflect attractive forces. Estimations of E_{LJ}^{X} values are similar to E_{D3}^{X} values (Fig. 13, 95% confidence interval (CI) = 0.73 kJ mol^{-1}) for DFT-optimized H-bonded acetone and TS2 structures at a variety of T-site locations (TON: T1, T2 Al locations for H-bonded acetone; MFI: T1-T12 Al locations for H-bonded acetone, T12 Al location for TS2; FAU: T1 Al location for H-bonded acetone and for TS2; VASP, RPBE + D3(BJ)), and this benchmarking was used to determine the ε-factor (ε = 1.59 $\pm$ 0.01 kJ mol^{-1}; Fig. 13) in Equation 26. This ε-factor is independent of organic moiety and framework structure (Fig. 13; TS2, H-bonded acetone organic moieties; TON, MFI, FAU frameworks), consistent with the non-specific nature of van der Waals interactions.

Figure 14 shows that attractive components of minimum E_{LJ}^{Ac*} values, which were calculated, without DFT-optimization of the structure, for H-bonded acetone (Fig. 10a) at each of the 30 distinct O-atoms of the MFI framework accessible to acetone (crystal structure [61]; sampling placement of H-bonded acetone described in Section 2.2.6), are similar to E_{D3}^{Ac*} values of DFT-optimized structures (VASP, RPBE + D3(BJ); 95% CI = 1.61 kJ mol^{-1}). Such similarities over diverse environments and acetone binding locations (E_{LJ}^{Ac*} = -82 – -111 kJ mol^{-1}) show that

this method allows efficient comparisons of stabilization interactions caused by the void environment surrounding each T-site within each framework without requiring full DFT calculations and suggests that calculated E_{LJ}^{Ac*} values provide an accurate assessment of the van der Waals stabilization interactions between H-bonded acetone and the surrounding framework despite these calculations excluding any effects of structural relaxation in the organic moiety and framework components in response to their proximity.

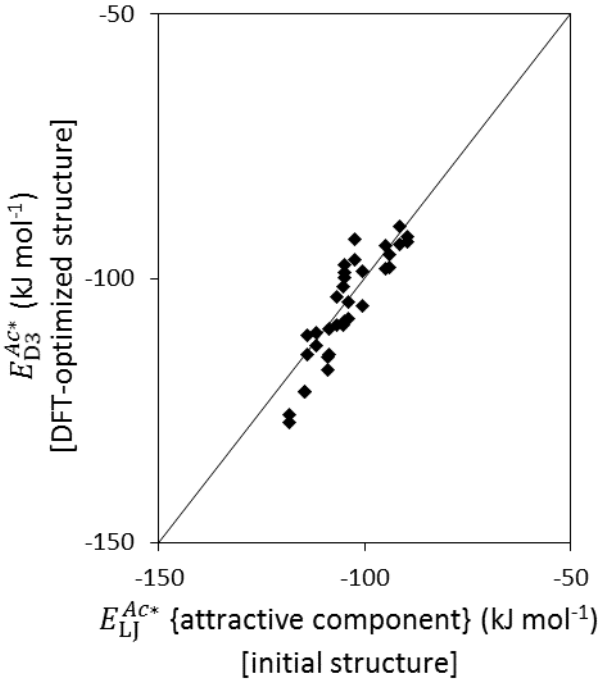

Figure 14: D3 dispersive energy corrections of optimized DFT-structures for H-bonded acetone (Eq. 25) at all distinct O-atoms of MFI as a function of E_{LJ}^{Ac*} values of initial structures (not DFT-optimized). VASP, RPBE + D3(BJ) PAW5. E_{LJ}^{Ac*} values calculated with ε = 1.59 kJ mol^{-1} , Eq. 26. Solid line is a parity line.

The E_{vdW} values of kinetically-relevant transition states (TS2) and precursors (H-bonded acetone) were calculated as E_{LJ}^{X} values by sampling each of the crystallographically-distinct Al locations in each framework according to the method described in Section 2.2.6 for placement of the organic moieties. The E_{vdW} value at each Al location represents the exponential ensemble-average of at least 10^3 orientations of the organic moiety (*j*; Section 2.2.6), weighted by their relative abundance in equilibrated configurations:

$$E_{\mathrm{vdW}} = \frac{\sum_j E_{\mathrm{vdW},j} \exp\left(-\frac{E_{\mathrm{int},j}}{k_B T}\right)}{\sum_j \exp\left(-\frac{E_{\mathrm{int},j}}{k_B T}\right)} \tag{27}$$

where $E_{\mathrm{int},j}$ denotes the interaction energy of configuration, j, which can be dissected into electrostatic and van der Waals contributions using Equation 22:

$$E_{\mathrm{vdW}} = \frac{\sum_j E_{\mathrm{vdW},j} \exp\left(-\frac{E_{\mathrm{vdW},j}}{k_B T}\right)}{\sum_j \exp\left(-\frac{E_{\mathrm{vdW},j}}{k_B T}\right)} \tag{28}$$

Here, the only term of the interaction energy that depends on the configuration of the organic moiety is $E_{\mathrm{vdW},j}$; thus, the remaining energy terms from the dissection of the activation barrier can be factored out of the sum and subsequently cancel from the numerator and denominator terms of Equation 28. The differences between the E_{vdW} values for TS2 $\left(E_{\mathrm{vdW}}^{TS2}\right)$ and H-bonded acetone $\left(E_{\mathrm{vdW}}^{H-Ac}\right)$ therefore rigorously account for the effects of the void environment on acetone condensation rates at each crystallographically-distinct T-site (Eq. 23).

Calculated ΔE_{vdW} values for TON, FAU, and BEA frameworks are similar at each of their respective Al T-site locations (Fig. 15), but vary with framework structure. These results reflect that these frameworks each consist of a single void environment. TON is a one-dimensional, straight channel framework, which has three distinct T-site locations in this channel; therefore, each T-site is surrounded by a similar void environment with nearly identical ΔE_{vdW} values (95% CI = 1.0 kJ mol^{-1}; Fig 15). FAU is a three-dimensional framework with one distinct T-site location; thus, all T-sites are surrounded by identical void environments. The BEA framework consists of two 12-member ring straight channels that intersect to form large voids with limiting diameters similar to those of the channels (Table 1), which provide similar void environments surrounding each of the 9 distinct T-sites (95% CI = 6.0 kJ mol^{-1}; Fig. 15). Therefore, $\langle \Delta E_{\mathrm{vdW}} \rangle$ values (Eq. 24) do not depend on the locations of the Al atoms and their associated protons among the distinct T-sites in these frameworks.

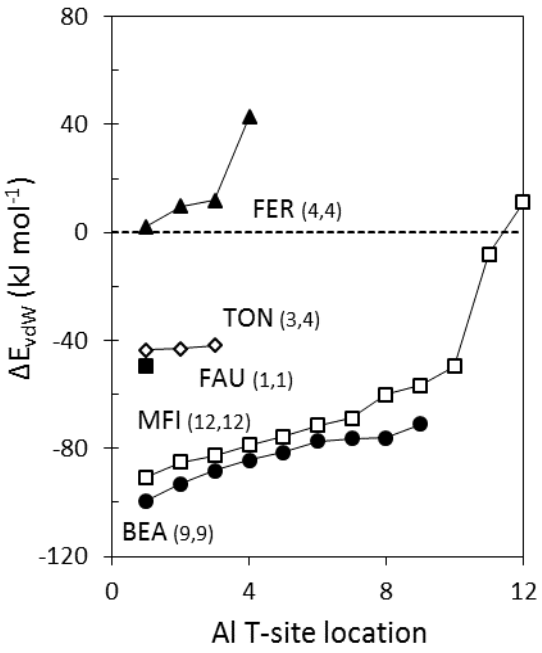

Figure 15: The differences in van der Waals interaction energy values between TS2 and H-bonded acetone (ΔE_{vdW}) at each crystallographically unique Al locations in FER (closed triangles), TON (open circles), FAU (closed squares), MFI (open diamonds), and BEA (closed circles) calculated by Eq. 23. Horizontal axis values are arranged by ascending ΔE_{vdW}-value. Values in parentheses denote the number of accessible Al locations and the total number of crystallographically unique Al locations in each aluminosilicate framework.

The ΔE_{vdW} values for MFI and FER frameworks, however, differ significantly among T-site locations (Fig. 13) because of the very different local environments created by the channel intersections and cage-like voids in these zeolites (Table 1), respectively. Comparisons of measured condensation rate constants with calculated $\langle \Delta E_{\mathrm{vdW}} \rangle$ values (Eq. 24) require knowledge about Al location in samples, which depend on synthetic protocols and are seldom accessible to experiments [89, 90].

Al locations were assumed as uniformly distributed among all distinct T-sites in the absence of experimental evidence of T-site speciation, where $\mathrm{P}_{\mathrm{T\text{-}site},i}$ (Eq. 24) is given by:

$$\mathrm{P}_{\mathrm{T-site},i} = \frac{D_{\mathrm{T-site,i}}}{\sum_{j}^{N_{\mathrm{T-site}}} D_{\mathrm{T-site,j}}} \tag{29}$$

and $D_{\mathrm{T-site,i}}$ represents the number of locations of each T-site, i, per unit cell of the framework (Table 3). Three unique uniform distributions of Al were used to calculate $\langle \Delta E_{\mathrm{vdW}} \rangle$ values for each framework: (1) Al located with equal probability at all T-site locations ($\mathrm{P}_{\mathrm{T\text{-}site}}$; Table 3), (2) Al located with equal probability at T-site locations with access to channels of the framework (T1-T3 and T5-T12 sites in MFI, T1-T3 sites in FER), and (3) Al located with equal probability at T-site

locations with access only to the intersection of framework channels in MFI and cage-like structures in FER (T4 site in MFI, T4 site in FER). The resulting $\langle \Delta E_{\mathrm{vdW}} \rangle$ values provide an estimate of the sensitivity of $\langle \Delta E_{\mathrm{vdW}} \rangle$ to the distribution of Al locations (horizontal bars; Fig. 16).

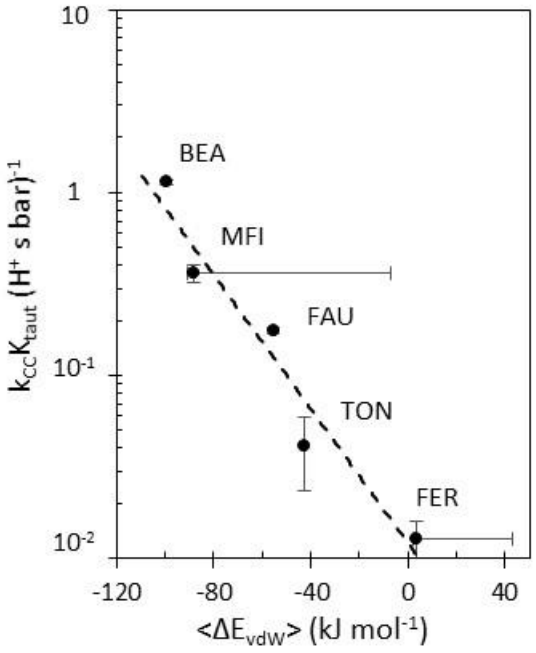

Figure 16: First-order acetone condensation rate constants (473 K, 0.1-5 kPa acetone, 27 kPa H_2) as a function of the ensemble-averaged E_{vdW}-values ($\langle \Delta E_{\mathrm{vdW}} \rangle$) for aluminosilicates (Eq. 24). All samples contain Pt (amount and location of Pt provided in Fig. 4 for MFI, BEA and SI, 2.6.7 for FER, TON, FAU). Vertical bars represent 95% confidence intervals of the regressed linear fits of rate data to the form of Eq. 12. Horizontal bars represent the ensemble averaging of the distinct void environments within each framework. The dashed line through the data points is a trend line.

Measured condensation rate constants increase linearly on a semi-logarithmic plot with decreasing $\langle \Delta E_{\mathrm{vdW}} \rangle$ values (Fig. 16) reflecting the exponential dependence of rate constants on activation barriers that decrease with decreasing $\langle \Delta E_{\mathrm{vdW}} \rangle$ (Scheme 4). Calculated $\langle \Delta E_{\mathrm{vdW}} \rangle$ values also describe the difference in measured reactivity between BEA ($\langle \Delta E_{\mathrm{vdW}} \rangle$ = -99 kJ mol^{-1}) and MFI ($\langle \Delta E_{\mathrm{vdW}} \rangle$ = -88 kJ mol^{-1}), frameworks with similar void size as described by largest cavity diameters (Fig. 12). The lower measured reactivity (per proton) on MFI compared to BEA is surprising given that the channel intersection in MFI, accessible to 11 of the 12 T-sites in MFI (T4 site is the exception), stabilizes the transition state (TS2) to a greater extent than BEA (minimum E_{vdW}^{TS2} = -185 and -179 kJ mol^{-1} for MFI and BEA, respectively; Table 3). The difference in reactivity, however, is attributed to the greater stabilization of the H-bonded acetone species in the sinusoidal channels of MFI, accessible to oxygen atoms vicinal to 11 of the 12 T-sites in MFI (T11 site is the exception), relative to the larger straight channels of BEA (minimum E_{vdW}^{H-Ac} = -108 and

-85 kJ mol^{-1} for MFI and BEA, respectively; Table 3). This increased stabilization of the precursors on MFI leads to larger free energy barriers and the lower reactivity of protons within MFI compared to BEA.

The T4-site located in FER is also of a similar void size to those in MFI and BEA (0.70 nm), but is least effective among the T-sites in FER in stabilizing TS2 (E_{vdW}^{TS2} = -59 kJ mol^{-1} for Al4 FER; Table 3) and much less effective in stabilizing TS2 compared to MFI (E_{vdW}^{TS2} = -185 kJ mol^{-1}) or BEA (E_{vdW}^{TS2} = -179 kJ mol^{-1}). These differences in E_{vdW}^{TS2} values across voids of similar size shows the inability of geometric descriptor, such as void size, to account for the asymmetry of these voids. This method of estimating the van der Waals stabilization energy quantifies the diversity in the size and shape of void environments in aluminosilicate frameworks, where different environments are preferred by adsorbates and transition states, even at a single T-site location, based on the size and shape of the void and that of the organic moieties. The difference between these stabilization energies is the rigorous descriptor of the catalytic consequences of the void environment.

Table 3: Number of each T-site per unit cell ($D_{\text{T-site}}$), T-site probability ($P_{\text{T-site}}$, Eq. 28), E_{vdW}^{TS2} (kJ mol^{-1}; Eq. 26), E_{vdW}^{H-Ac} (kJ mol^{-1}; Eq. 26), ΔE_{vdW} (kJ mol^{-1}; Eq. 23) for each distinct Al location on (a) FER, (b) TON, (c) MFI, (d) BEA, (e) FAU frameworks.

(a) FER (4 T-sites)

configuration	Al T-site	$D_{\text{T-site}}$	$P_{\text{T-site}}$	E_{vdW}^{TS2}	E_{vdW}^{H-Ac}	ΔE_{vdW}
1	Al1	16	0.444	-98	-100	2
2	Al2	8	0.222	-90	-102	12
3	Al3	8	0.222	-100	-110	10
4	Al4	4	0.111	-59	-102	43

(b) TON (4 T-sites)

configuration	Al T-site	$D_{\text{T-site}}$	$P_{\text{T-site}}$	E_{vdW}^{TS2}	E_{vdW}^{H-Ac}	ΔE_{vdW}
1	Al1	8	0.333	-138	-95	-43
2	Al2	8	0.333	-139	-97	-42
3	Al3	4	0.167	-141	-98	-43
4	Al4	4	0.167	--	--	--

(c) MFI (12 T-sites)

configuration	Al T-site	$D_{\text{T-site}}$	$P_{\text{T-site}}$	E_{vdW}^{TS2}	E_{vdW}^{H-Ac}	ΔE_{vdW}
1	Al1	8	0.083	-181	-99	-82
2	Al2	8	0.083	-150	-100	-50
3	Al3	8	0.083	-167	-107	-60
4	Al4	8	0.083	-114	-106	-8
5	Al5	8	0.083	-181	-102	-79
6	Al6	8	0.083	-183	-108	-75

7	Al7	8	0.083	-163	-107	-56
8	Al8	8	0.083	-82	-93	11
9	Al9	8	0.083	-170	-101	-69
10	Al10	8	0.083	-169	-98	-71
11	Al11	8	0.083	-185	-95	-90
12	Al12	8	0.083	-185	-100	-85

(d) BEA (9 T-sites)

configuration	Al T-site	$D_{\text{T-site}}$	$\text{P}_{\text{T-site}}$	E_{vdW}^{TS2}	E_{vdW}^{H-Ac}	ΔE_{vdW}
1	Al1	8	0.125	-155	-84	-71
2	Al2	8	0.125	-162	-85	-77
3	Al3	8	0.125	-170	-82	-92
4	Al4	8	0.125	-165	-81	-84
5	Al5	8	0.125	-158	-82	-76
6	Al6	8	0.125	-179	-80	-99
7	Al7	8	0.125	-161	-85	-76
8	Al8	4	0.0625	-173	-80	-93
9	Al9	4	0.0625	-165	-84	-81

(e) FAU (1 T-site)

configuration	Al T-site	$D_{\text{T-site}}$	$\text{P}_{\text{T-site}}$	E_{vdW}^{TS2}	E_{vdW}^{H-Ac}	ΔE_{vdW}
1	Al1	192	1.00	-113	-58	-55

Lennard-Jones potentials describing the interactions between framework oxygen atoms and atoms of the relevant organic moieties (transition state and precursors) provide valuable insights into the effects of the confining void by quantifying the van der Waals stabilization energy proffered by the diverse sizes and shapes of the void environments throughout aluminosilicate frameworks. The methods described herein require DFT-estimated structures of the organic moieties (TS2 and H-bonded acetone; MFI Al T12 site, VASP, RPBE + D3(BJ)) and rigorous averaging of the stabilization energies at each T-atom location to allow comparisons with experimentally-measured rate constants (per proton). The descriptor of void environment used here ($\langle \Delta E_{\text{vdW}} \rangle$) offers significant advances in the current understanding of the catalytic effects of confining voids by providing (1) consideration of both attractive and repulsive interactions and, thus, estimations of van der Waals stabilization without full DFT-optimizations, (2) efficient determination of reasonable initial structures for DFT-simulations, and (3) extension to other acid-catalyzed reactions with known structures of the relevant transition states and precursors.

2.3.7 Effects of acid strength on catalyst reactivity for acetone reactivity

Acetone condensation rates measured on MFI samples of different heteroatom substitution (Al-, Fe-, Ga-, and B-MFI containing 1% wt. extracrystalline Pt) increased proportionally with increasing acetone pressure (Fig. 17) consistent with the first-order acetone pressure dependencies

measured on all aluminosilicate samples (Section 2.3.3) and the derived rate expression for acetone condensation (Eq. 12). These similar pressure dependencies of condensation rates suggest similar chemical interpretation of the slope of the curve, $k_{CC}K_{taut}$ (Scheme 3).

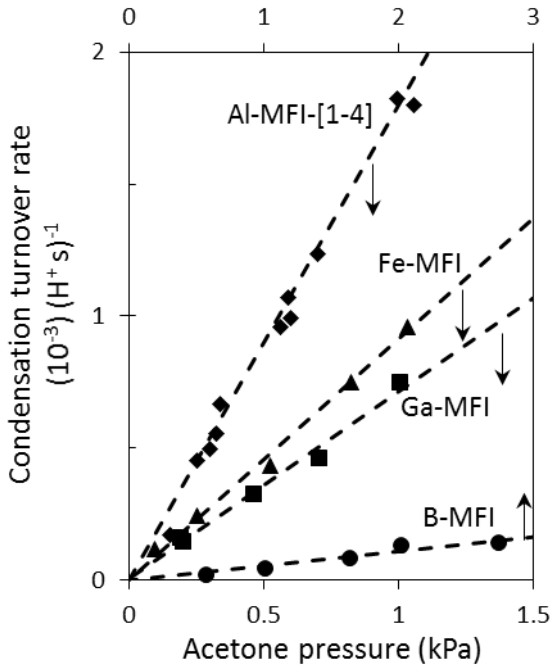

Figure 17: Condensation turnover rate as a function of acetone pressure on Pt-containing samples: Al-MFI-[1-4] (diamonds), Fe-MFI (triangles), Ga-MFI (squares), and B-MFI (circles) (473 K, 27 kPa H_2). All samples contain 1% wt. extracrystalline Pt in the form of Pt/SiO_2. Dashed lines are regressed fits of rate data to the form of Eq. 12.

Acetone condensation rate constants ($k_{CC}K_{taut}$) reflect the activation barrier required to form TS2 from H-bonded acetone and gaseous acetone precursors (Scheme 4). Assessments of the effects of catalyst acid strength on measured $k_{CC}K_{taut}$ values require a measure of acid strength. Acid strength is determined by the stability of the conjugate anion to accept charge; the conjugate anion is formed when the acid site is deprotonated. Efforts to experimentally measure acid strength of zeolitic protons convolute the effects of acid strength with the stability of the proton receptor species and the stabilization of the receptor species due to the size and shape of the surrounding void environment (confinement). Thus, the only rigorous descriptor of acid strength is theoretically accessible and is the energy required to heterolytically cleave the proton from the conjugate anion and separate them to a distance where they no longer interact, deprotonation energy (DPE). DPE values have been previously reported for heteroatom substituted MFI samples [36].

$k_{CC}K_{taut}$ values increased exponentially with decreasing DPE values (increasing catalyst acid strength), as shown in Figure 18. Catalyst reactivities that increases with increasing acid strength are consistent with reaction pathways that are mediated by ion-pair transition states (TS2; Figure 9) formed from uncharged precursors (H-bonded acetone and gaseous acetone) [36, 91],

which supports the mechanistic interpretations for acetone condensation on solid acids discussed above. The exponential dependence of $k_{CC}K_{taut}$ values with respect to DPE values (Fig 18) reflects the exponential dependence of rate constants on activation barriers (Eq. 8), and is represented by:

$$\frac{d(\ln(k_{CC}K_{taut}))}{d(\mathrm{DPE})} = -\frac{1}{\mathrm{RT}}\frac{d(\Delta E^{TS2})}{d(\mathrm{DPE})} \tag{30}$$

where ΔE^{TS2} is the activation barrier for acetone condensation (Scheme 4).

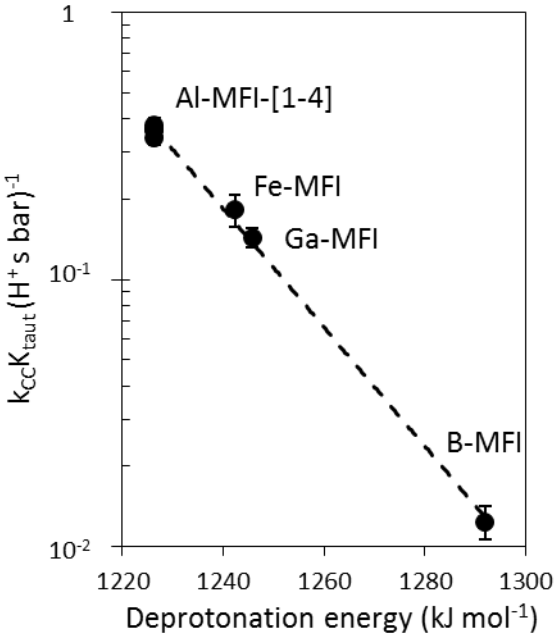

Figure 18: First-order acetone condensation rate constants (473 K, 0.1-2 kPa acetone, 27 kPa H_2) as a function of deprotonation energy (DPE; reported in [36]) for MFI samples of different heteroatom substitution (Al-, Fe-, Ga-, B-MFI samples; Table 1). All samples contain 1% wt. extracrystalline Pt. Vertical bars represent 95% confidence intervals of the regressed linear fits of rate data to the form of Eq. 12. The dashed line is a regressed fit of the data to the form of Eq. 30.

The dependence of ΔE^{TS2} with respect to catalyst DPE is more clearly described by using a thermochemical cycle, shown in Scheme 4. This thermochemical cycle allows the decomposition of ΔE^{TS2}, similar to the discussion of the effects of confinement (Section 2.3.5):

$$\Delta E^{TS2} = -\left(E_{\mathrm{vdW}}^{Ac*} + E_{\mathrm{ES}}^{Ac*}\right) + \Delta E_{\mathrm{prot}}^{TS2} + \left(E_{\mathrm{vdW}}^{TS2} + E_{\mathrm{ES}}^{TS2}\right) \tag{31}$$

where each of the energy terms is shown in Scheme 4. DPE is a property of the catalyst and is the measure of the energy required to separate the proton from the conjugate anion; therefore, the

gaseous transformation of the organic moiety ($\Delta E_{\mathrm{prot}}^{TS2}$) and the van der Waals stabilization energies (E_{vdW}^{X}) do not depend on catalyst DPE. These simplifications yield the description of the DPE dependence of ΔE^{TS2}:

$$\frac{d(\Delta E^{TS2})}{d(\mathrm{DPE})} = \frac{d\left(E_{\mathrm{ES}}^{TS2}\right)}{d(\mathrm{DPE})} - \frac{d\left(E_{\mathrm{ES}}^{Ac*}\right)}{d(\mathrm{DPE})} \tag{32}$$

The electrostatic stabilization energies (E_{ES}^{X}) that remain in Equation 32 describe the stabilization of the organic moieties conferred by the conjugate anion. The values of the derivatives on the right-side of Equation 32 are between zero and -1, where a value of -1 represents no charge separation at the ground state (a bare proton; $E_{\mathrm{ES}}^{X} = -\mathrm{DPE}$) and a value of zero represents complete charge separation to a distance where the two charged species no longer interact at the ground state (full ion-pair; $E_{\mathrm{ES}}^{X} = 0$). Thus, reaction pathways mediated by ion-pair transition states, which are ubiquitous for acid-catalyzed reactions [35-39], formed from uncharged precursors result in activation barriers that decrease with decreasing DPE (left-side of Eq. 32 is positive). The transition states for these reaction pathways require the separation of charge, and the more stable conjugate anions (stronger acids) can more effectively separate charge and therefore, decrease the activation barrier for the reaction (increase intrinsic reactivity of proton).

2.4 Conclusions

We present the elementary steps and assess their kinetic relevance for acetone condensation on a range of microporous and mesoporous aluminosilicates (FER, TON, MFI, BEA, FAU, and MCM-41) using kinetic, spectroscopic, and isotopic data that are supported by theoretical simulations. Rapid catalyst deactivation that limits the study and application of solid acid catalysts for aldol condensation was inhibited through the addition of Pt—as physical mixtures with the acid catalyst or ion-exchanged into the crystals—and H_2 to hydrogenate C=C bonds in the reactive α,β-unsaturated intermediates, MO. Selective titrations of the active site with 2,6-di-*tert*-butyl pyridine during catalysis suggest that protons account for all of the reactivity and allow assessment of the number of active protons in each sample, which is required for rigorous normalization of the measured rate and comparisons with DFT-simulated barriers (free energy and enthalpy). Our experimental work, in tandem with our DFT-calculations benchmark a descriptor of the catalytic consequences of confining void environment on reactivity; this descriptor is the van der Waals stabilization energies, which quantifies the fit—size and shape—of the relevant organic moieties (TS2 and H-bonded acetone) in the void environment. These assessments of fit demonstrate that differences in the reactivity of aluminosilicates are explained by their ability to preferentially stabilize the transition states over the relevant precursors even in the case of frameworks of similar size (MFI and BEA), which cannot be distinguished by void size. Estimations of van der Waals stabilization energies also identify these zeolite frameworks that have diverse void environments (MFI and FER) where the barrier is very sensitive to the distribution of Al locations. These

methods and concepts of describing the effect of the void environment on catalyst reactivity provide improved efficiency and do not require full DFT-simulations at each T-site location, and they are also general and can be used for any solid acid catalyzed reaction. We also investigated the effect of acid strength on the intrinsic reactivity of protons within MFI samples of different heteroatom substitution (isomorphously-substituted Al-, Fe-, Ga-, B-MFI samples). We found that condensation rate constants increased exponentially with deprotonation energy (DPE)—the theoretically accessible and rigorous descriptor of catalyst acid strength—which is consistent with the DFT-simulations shown here. The proposed mechanism for acetone condensation depends on an activation barrier that reflects the energy difference between uncharged precursors (H-bonded acetone and gaseous acetone) and an ion-pair transition state (TS2); this measured dependence on acid strength is ubiquitous for acid catalyzed reactions that occur from uncharged precursors.

2.5 Acknowledgements

The authors acknowledge: the financial support of BP, p.l.c. for this work as part of the BP Conversion Consortium (BP-XC^2) the technical discussions with Drs. Drew Braden, Eric Doskocil, and John Shabaker (BP, p.l.c.), Dr. Shuai Wang, Dr. David Hibbitts, and Michele Sarazen (University of California, Berkeley), and Prof. Matthew Neurock (University of Minnesota); the proton counts of the FER sample performed by Dr. Andrew Jones and Gina Noh (University of California, Berkeley); and Dr. Neng Guo (BP, p.l.c.) for the synthesis of the MFI samples of different heteroatoms (Fe-, Ga-, B-MFI samples). Computational facilities were provided by BP High Performance Computing (BP, p.l.c.) and by the Extreme Science and Engineering Discovery Environment (XSEDE), which is supported by the National Science Foundation (grant number: CHE-140066).

2.6 Supporting Information

2.6.1 Equilibrium concentration of diacetone alcohol

Diacetone alcohol (DA) is the initial product of acetone condensation; however, it was not detected (GC, FID) at any of the reaction conditions used. DA undergoes facile dehydration on the Brønsted acid site equilibrating DA with mesityl oxide (MO) with an equilibrium pressure of DA represented as:

$$(DA) = \frac{(MO)(H_2O)}{\exp\left(\frac{-\Delta G}{RT}\right)} \tag{S1}$$

where (X), $X = DA, MO, H_2O$, represents the respective pressures (bar) of DA, MO, and H_2O; and ΔG is the reaction free energy for the dehydration of DA to MO and H_2O. The calculated ΔG is -51 kJ mol^{-1} (473 K, VASP, RPBE + D3(BJ); as discussed in Section 2.2.4) resulting in estimated equilibrium DA pressure ranges from 3.2 x 10^{-14} to 5.1 x 10^{-10} Pa (Eq. S1) over the measured range of MO and H_2O pressures (3.5 x 10^{-2} to 4.4 Pa). These DA pressures are far below the GC detection limit for DA (0.05 Pa), as determined by direct GC injections of known concentrations of a DA standard (≥ 98%, Santa Cruz Biotechnology).

2.6.2 Calculating ensemble (exponential) average of free energies

Measured rates respond to the local void environment surrounding each proton, where the measured rate ($\langle r \rangle$) normalized by the number of protons (N_{H^+}) is given by:

$$\frac{\langle r \rangle}{N_{H^+}} = \frac{1}{N_{H^+}} \sum_{i=1}^{N_{H^+}} r_i \tag{S2}$$

where r_i is the rate at each proton, i. Transition state theory of non-ideal systems relate this rate to a Gibbs free energy barrier ($\Delta G^{\ddagger}$):

$$r = \frac{k_B T}{h} \exp\left(-\frac{\Delta G^{\ddagger}}{k_B T}\right) \prod_j a_j^{\nu_j} \tag{S3}$$

Here k_B is the Boltzmann constant, h is Planck's constant, a_j represents the activity of species j, and ν_j represents the stoichiometric coefficient of species j, respectively. This representation of the rate is substituted into Equation S2 providing:

$$\frac{k_B T}{h} \exp\left(-\frac{\langle \Delta G^{\ddagger} \rangle}{k_B T}\right) \prod_j a_j^{\nu_j} = \frac{1}{N_{H^+}} \sum_{i=1}^{N_{H^+}} \frac{k_B T}{h} \exp\left(-\frac{\Delta G_i^{\ddagger}}{k_B T}\right) \prod_j a_j^{\nu_j} \tag{S4}$$

where $\langle \Delta G^{\ddagger} \rangle$ represents the ensemble (exponential) average Gibbs free energy barrier. Equilibrium of gaseous species at all protons (Fig. 5) allows the cancellation of the activity terms, and solving for $\langle \Delta G^{\ddagger} \rangle$ yields:

$$\langle \Delta G^{\ddagger} \rangle = -k_B T \ln \left(\frac{1}{N_{H^+}} \sum_{i=1}^{N_{H^+}} exp\left(-\frac{\Delta G_i^{\ddagger}}{k_B T} \right) \right) \tag{S5}$$

This equation requires the Gibbs free energy barrier at each proton in the sample, which is simplified by lumping together protons in crystallographically identical positions in the framework:

$$\langle \Delta G \rangle = -k_B T \ln \left(\sum_{i=1}^{N_{\text{site}}} \exp\left(-\frac{\Delta G_i}{k_B T} \right) \mathrm{P}_{\text{site},i} \right) \tag{S6}$$

where N_{site} is the total number of crystallographically distinct sites, and $\mathrm{P}_{\text{site},i}$ is the probability the proton is located at site i. If there is equal probability the proton is at each site (uniform distribution), the probability term is given by:

$$\mathrm{P}_{\text{site},i} = \frac{1}{N_{\text{site}}} \tag{S7}$$

which would lead to an equation similar to Equation S5 ($N_{\text{site}} = N_{H^+}$).

Each T-site location in these aluminosilicate frameworks has 4 vicinal oxygen atoms ($N_{\text{site}} = 4$), and each oxygen has a probability of being bound to the proton determined by the Boltzmann distribution of free energies:

$$\mathrm{P}_{\text{site},i} = \frac{\exp\left(-\frac{G_i^p}{k_B T} \right)}{\sum_{j=1}^{N_{\text{site}}} \exp\left(-\frac{G_j^p}{k_B T} \right)} \tag{S8}$$

This is used when determining free energies of acetone adsorption at a T-site (Section 2.3.3) and calculating expectation values (Eq. 25).

The ensemble average Gibbs free energy for an entire framework requires a distribution of Al locations, and here we assume a uniform distribution across all T-sites of the unit cell:

$$\mathrm{P}_{\text{site},i} = \frac{D_{\text{site,i}}}{\sum_{j}^{N_{\text{site}}} D_{\text{site,j}}} \tag{S9}$$

where N_{site} is the number of crystallographically distinct T-site and $D_{\text{site},i}$ is the number of T-site i present in the unit cell.

2.6.3 DFT-estimated structures of acetone bound to protons at distinct locations on MFI framework

The bond distance between the framework oxygen ($O_{zeolite}$) and the proton of DFT-simulated structures of H-bonded acetone at each crystallographically distinct T-site on MFI were are shown in Figure S.1 (VASP, RPBE + D3(BJ)). The (expected) bond distances $\left(\langle d_{O_z-H}\rangle\right)$ for Al located at each crystallographically distinct T-site (closed symbols, Fig S.1) were calculated by:

$$\langle d_{O_z-H}\rangle = \frac{\sum_{i=1}^{O-atoms}\left(d_{O_{z,i}-H}\right)\exp\left(-\frac{G_{O_{z,i}-H}}{k_BT}\right)}{\sum_{j=1}^{O-atoms}\exp\left(-\frac{G_{O_{z,j}-H}}{k_BT}\right)} \qquad \text{(S10)}$$

where $d_{O_{z,i}-H}$ is the $O_{zeolite}$-H bond distance at each O-atom, i, and $G_{O_{z,i}-H}$ is the corresponding Gibbs free energy of H-bonded acetone at that framework O-atom. This expected $O_{zeolite}$-H bond distance does not vary with Al location (Fig S.1) and has an arithmetic mean across all Al locations of 0.1100 $\pm$ 0.0005 nm, which was used to place the H-bonded acetone structure at each crystallographically unique position in FER, TON, MFI, BEA, and FAU frameworks (discussed in Section 2.2.6).

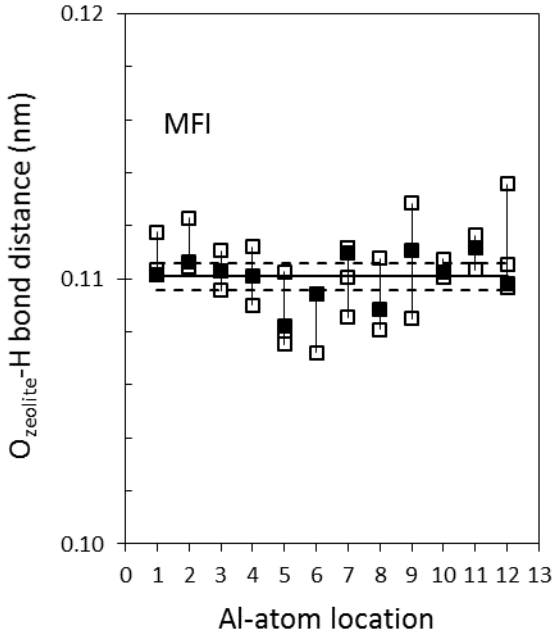

Figure S.1: DFT-estimated $O_{zeolite}$-H bond distance of H-bonded acetone at each accessible oxygen for all crystallographically distinct Al locations (open squares; MFI, VASP, RPBE + D3(BJ), PAW5). Expected $O_{zeolite}$-H bond distance (closed squares) calculated with Eq. S10. Solid and dashed horizontal lines are, respectively, the arithmetic mean of the expected $O_{zeolite}$-H bond distance at each Al location and corresponding 95% confidence interval (0.1100 $\pm$ 0.0005 nm).

2.6.4 Effect of acetone conversion and temperature on isomesityl oxide to mesityl oxide molar ratio, determination of thermodynamic constants for their interconversion.

Mesityl oxide and isomesityl oxide are the only C_6 products measured in the absence of a hydrogenation catalyst. These products are observed as a constant ratio to each other over the range of acetone conversion measured and across the aluminosilicate samples used (Fig. S.1a), consistent with rapid double-bond isomerization on protons and the equilibrium of the C_6 species. The temperature dependence of this product ratio is independent of catalyst identity (450 - 483 K, Fig. S.1b) and is used to determine the thermodynamic barrier in enthalpy (ΔH) and entropy (ΔS) defined by:

$$\Delta G = \Delta H - T\Delta S \tag{S11}$$

Substitution of Equation S9 into Equation 12 yields

$$K_{eq} = \frac{(IMO)}{(MO)} = \exp\left(-\frac{(\Delta H - T\Delta S)}{RT}\right) \tag{S12}$$

where (*IMO*) and (*MO*) denotes the respective pressures of isomesityl oxide and mesityl oxide and *R* represents the gas constant.

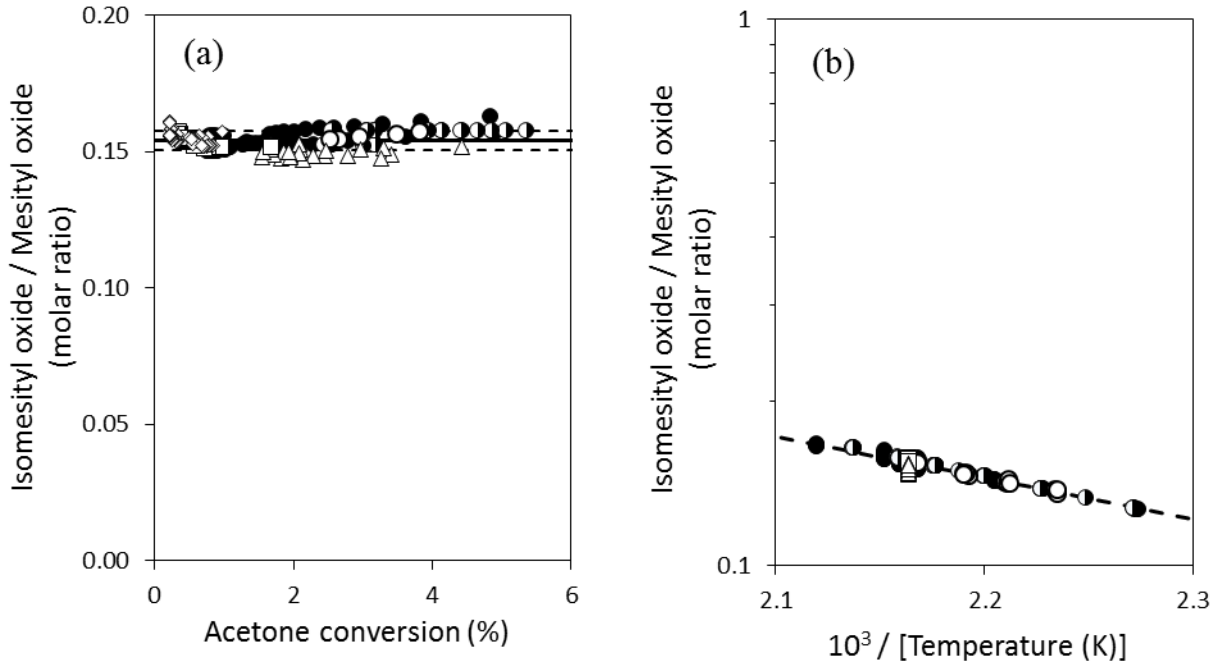

Figure S.2: Isomesityl oxide to mesityl oxide molar ratio as a function of (a) acetone conversion (473 ± 3 K, 0.1 - 5 kPa acetone) and (b) reaction temperature (450-483 K, 0.3-1 kPa acetone) on MFI-[1-4] (circles: ○, ○, ●, ◑, respectively) BEA-2 (squares), MCM-41 (triangles). Horizontal lines in (a) represents the fitted ratio at 473 ± 3 K with the solid line representing 473 K and the dashed lines representing 470 K and 476 K.Dashed line in (b) represents regressed fit of data to the form of Eq S12.

Regression of the data shown in Figure S.1b yields a ΔH of 14.4 $\pm$ 0.7 kJ mol^{-1} and a ΔS of 15 $\pm$ 1 J (mol K)$^{-1}$ (Eq. S10), which results in a ΔG of 7 $\pm$ 1 kJ mol^{-1} at 473 K (Eq. S9). These values are consistent with DFT-calculated ΔH of 17 kJ mol^{-1} for the conversion of MO to IMO (473 K, VASP, RPBE + D3(BJ), methods in Section 2.2.5) suggesting the equilibration of the C_6 species.

2.6.5 Effect of acetone conversion on acetic acid to isobutene molar ratio.

Isobutene and acetic acid were the majority of products formed during acetone condensation on MFI, in the absence of a hydrogenation catalyst. These products are produced in equimolar quantities over the range of acetone conversions measured (Fig. S.2); this is attributed to both species forming from a β-scission reaction of a C_6 species. At low acetone conversion the ratio appears to decrease below unity, but this is an artifact due to the difficulty in measuring low acetic acid concentration with the FID (chromatographic separation: HP-1).

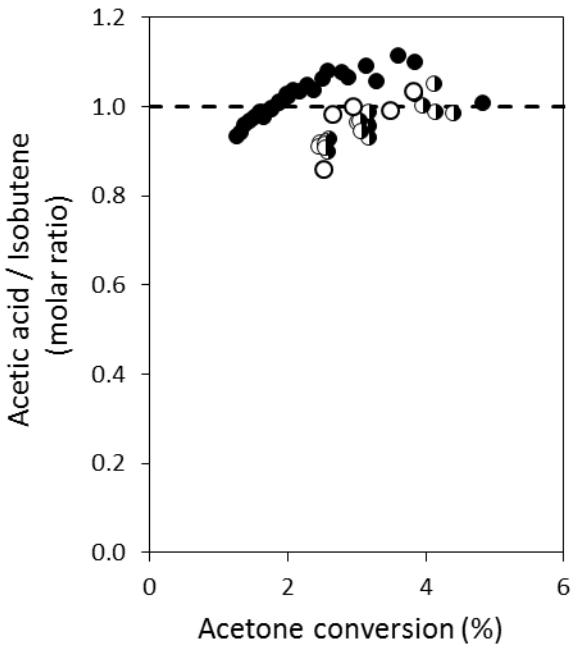

Figure S.3: Effect of acetone conversion on acetic acid to isobutene molar ratio on MFI-[1-4] (circles: ○,○,●,◑, respectively) (450-483 K, 0.3-1 kPa acetone). Dashed line denotes unity.

2.6.6 Effect of space velocity and H_2O pressure on acetone condensation rate.

Hydrogenation of acetone is undesired when upgrading acetone to larger chemicals and fuels; however, catalyst stability is of greater importance than selectivity for a mechanistic study. Acetone hydrogenation on the metal catalyst ultimately results in the formation of propane and H_2O, and the potential effects of these species on the condensation rate is the only concern for this

study. Concentration of these products depend on the conversion and to systematically varying the product concentrations the condensation rate is measured at various acetone residence times. Figure S.3a shows the effective first-order condensation rate constant as a function of residence time for different acetone pressures. The condensation rate decreases exponentially with increasing residence time indicating secondary reactions that block active sites—from condensation or acetone hydrogenation—and to account for this effect all reported rates are extrapolated to zero residence time (zero conversion).

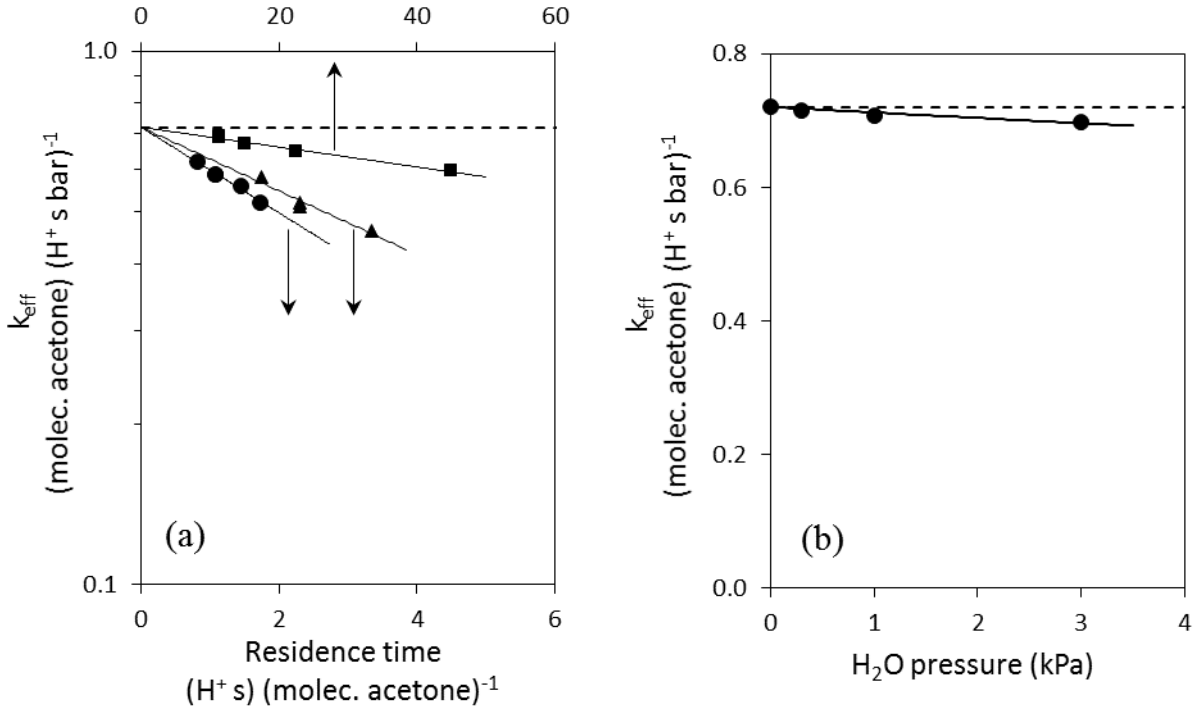

Figure S.4: Effective first-order condensation rate constant as a function of (a) residence time (473 K; 0.5, 1.9, 3.8 kPa acetone (squares, triangles, circles, respectively); 0 kPa H_2O co-fed) and (b) H_2O pressure on MFI-3 + Pt/SiO_2 (1% wt extracrystalline Pt; 473 K, 1.0 kPa acetone). Dashed lines denote first-order rate constant on MFI-3 + Pt/SiO_2, and solid lines represent (a) semilogarithmic regression of data collected at each acetone pressure according and (b) regressed fit of data to the form of Eq S13.

Oligomerization of propene and cross-coupling of propene and acetone are not observed due to the strong binding of acetone to the H^+ and the low operating conversions ($\leq$ 5%) ruling out any effects of propane and propene. Co-feeding H_2O to the reactor results in a negligible decrease in the condensation rate which can be described by an additional term in the denominator of the rate equation representing H_2O adsorption on protons:

$$r = \frac{k_{CC} K_{taut} K_{Ac} (Ac)}{K_{Ac}(Ac) + K_{H_2O}(H_2O)} \tag{S13}$$

where K_{H2O} represents the adsorption constant for H_2O on the H^+ and (H_2O) represents the H_2O pressure. The data in Figure S.3b provides a $K_{Ac}(K_{H2O})^{-1}$ estimate of 80 $\pm$ 20 when fitted to

Equation S11, which corresponding to acetone adsorption free energy being 17 $\pm$ 1 kJ mol^{-1} stronger than H_2O adsorption on protons (Eq. 9). In the absence of co-fed H_2O, the maximum H_2O pressure is 0.02 kPa, which is much lower than the pressure of co-fed H_2O and does not affect the condensation rate.

2.6.7 Effect of acetone pressure on condensation rate on all aluminosilicate samples used.

Condensation turnover rates (normalized per proton) are proportional to acetone pressure for all of the aluminosilicate samples used (Fig. S.5; FER, TON, MFI, BEA, FAU, MCM-41), which suggest that a similar mechanism for acetone condensation can be extended across all aluminosilicates used. The slope of these data for each sample represents the effective first-order rate constant and is used to compare the reactivity of the different samples (Fig. 12 and Fig. 14).

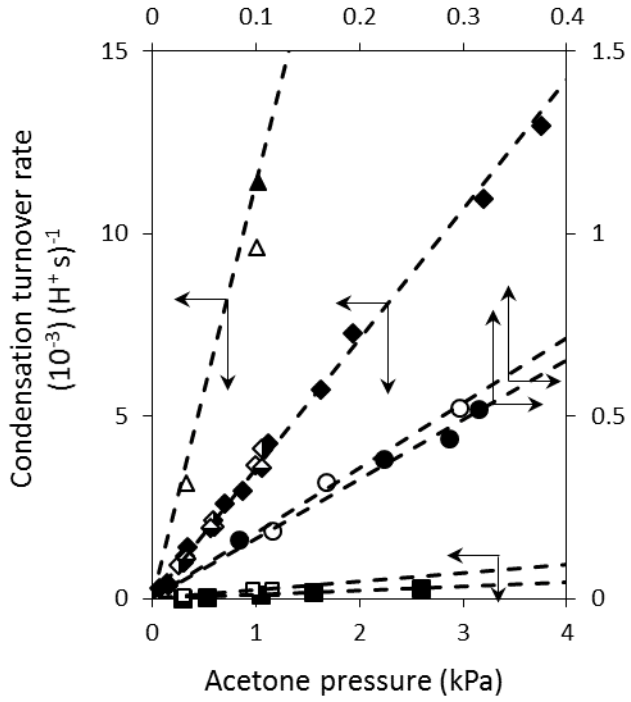

Figure S.5: Condensation turnover rate as a function of acetone pressure on Pt-stabilized FER (filled squares), TON (open squares), MFI-[1-4] (diamonds: ◇, ◇, ◆, ◇, respectively), BEA-[1-2] (triangles: filled, open, respectively), FAU (open circles), MCM-41 (closed circles) (473 K, 27 kPa H_2). Pt content: FER + Pt/SiO_2 (1% wt. extracrystalline Pt), TON + Pt/SiO_2 (1% wt. extracrystalline Pt), MFI-[1-4] + Pt/SiO_2 (1% wt. extracrystalline Pt), Pt/BEA-1 + Pt/SiO_2 (1% wt. intracrystalline Pt and 1% wt. extracrystalline Pt), BEA-2 + Pt/SiO_2 (1.3% wt. extracrystalline Pt), FAU + Pt/SiO_2 (1.3% wt. extracrystalline Pt), MCM-41 + Pt/SiO_2 (0.66% wt. extracrystalline Pt). Dashed lines are regressed linear fits to the form of Eq. 12. Rate data at higher acetone pressures are shown for BEA-1 sample in Figure 4.

2.6.8 H/D kinetic isotope effect on condensation rates

Measured condensation rates on MFI-3 + Pt/SiO_2 flowing perdeuterated acetone (acetone-d_6) and D_2 were similar to those measured while flowing undeuterated acetone (acetone-d_0) and H_2, as shown in Figure S.6.

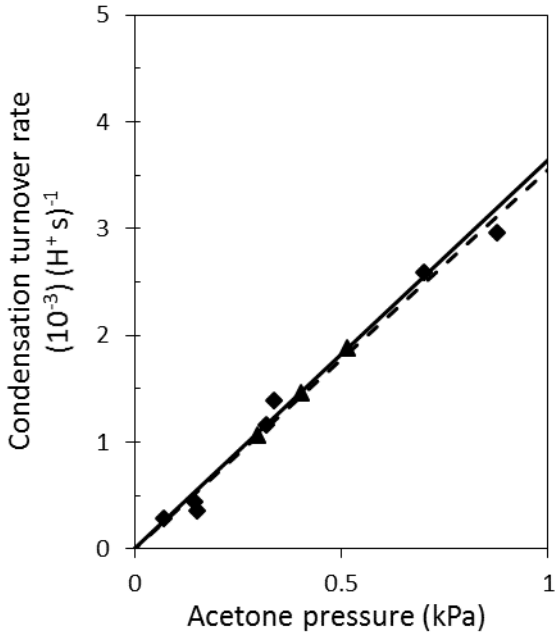

Figure S.6: Condensation turnover rate as a function of acetone-d_0 (diamonds) and acetone-d_6 (triangles) pressure on Pt-stabilized MFI-3 (473 K, 27 kPa H_2 (diamonds) and 27 kPa D_2 (triangles); 1% wt. extracrystalline Pt). Dashed and solid lines are regressed linear fits to the form of Eq. 15 for the rate data using acetone-d_0/H_2 and acetone-d_6/D_2, respectively.

2.7 References

1. Taarning, E., et al., *Zeolite-catalyzed biomass conversion to fuels and chemicals.* Energy & Environmental Science, 2011. **4**(3): p. 793-793.
2. Kumar, P., et al., *Methods for Pretreatment of Lignocellulosic Biomass for Efficient Hydrolysis and Biofuel Production.* Industrial & Engineering Chemistry Research, 2009. **48**: p. 3713-3729.
3. Bridgwater, A., *Renewable fuels and chemicals by thermal processing of biomass.* Chemical Engineering Journal, 2003. **91**(2-3): p. 87-102.
4. Corma, A., et al., *Production of High-Quality Diesel from Biomass Waste Products.* Angewandte Chemie (International ed.), 2011. **50**(10): p. 2375-2378.
5. Di Cosimo, J.I. and C.R. Apesteguía, *Study of the catalyst deactivation in the base-catalyzed oligomerization of acetone.* Journal of Molecular Catalysis A: Chemical, 1998. **130**(1-2): p. 177-185.
6. Luo, S. and J.L. Falconer, *Aldol condensation of acetaldehyde to form high molecular weight compounds on TiO2.* Catalysis letters, 1999. **57**: p. 89-93.
7. Sun, J., et al., *Key Roles of Lewis Acid-Base Pairs on ZnxZryOz in Direct Ethanol/Acetone to Isobutene Conversion.* Journal of the American Chemical Society, 2016. **138**(2): p. 507-517.
8. Sad, M.E., M. Neurock, and E. Iglesia, *Formation of C-C and C-O bonds and oxygen removal in reactions of alkanediols, alkanols, and alkanals on copper catalysts.* Journal of the American Chemical Society, 2011. **133**(50): p. 20384-98.
9. Biaglow, A.I., et al., *A 13C NMR Study of the Condensation Chemistry of Acetone and Acetaldehyde Adsorbed at the Brønsted Acid Sites in H-ZSM-5.* Journal of Catalysis, 1995. **151**(2): p. 373-384.
10. Lin, F. and Y.-H.C. Chin, *Mechanism of intra- and inter-molecular CC bond formation of propanal on Brønsted acid sites contained within MFI zeolites.* Journal of Catalysis, 2014. **311**: p. 244-256.
11. Gounder, R. and E. Iglesia, *The catalytic diversity of zeolites: confinement and solvation effects within voids of molecular dimensions.* Chemical communications (Cambridge, England), 2013. **49**(34): p. 3491-509.
12. Jones, A.J. and E. Iglesia, *The Strength of Brønsted Acid Sites in Microporous Aluminosilicates.* ACS Catalysis, 2015. **5**(10): p. 5741-5755.
13. Kubelková, L., et al., *Acetone Conversion and Deactivation of Zeolites*, in *Studies in Surface Science and Catalysis*, P.A. Jacobs and R.A.v. Santen, Editors. 1989, Elsevier. p. 1203-1212.
14. Kubelková, L. and J. Nováková, *Deactivation and regeneration of HZSM-5 zeolite in acetone conversion: Properties of OH groups.* Journal of Molecular Catalysis, 1992. **75**(1): p. 53-62.
15. Ungureanu, A., et al., *Aldol condensation of aldehydes over semicrystalline zeolitic-mesoporous UL-ZSM-5.* Microporous and Mesoporous Materials, 2005. **84**(1-3): p. 283-296.
16. Konno, H., et al., *Characterization and catalytic performance of modified nano-scale ZSM-5 for the acetone-to-olefins reaction.* Applied Catalysis A: General, 2014. **475**: p. 127-133.
17. Tago, T., et al., *Selective synthesis for light olefins from acetone over ZSM-5 zeolites with nano- and macro-crystal sizes.* Applied Catalysis A: General, 2011. **403**(1-2): p. 183-191.

18. Panov, A.G. and J.J. Fripiat, *Acetone Condensation Reaction on Acid Catalysts.* Journal of Catalysis, 1998. **178**(1): p. 188-197.
19. Hutchings, G., et al., *Acetone conversion to isobutene in high selectivity using zeolite β catalyst.* Catalysis letters, 1993. **21**(1-2): p. 49-53.
20. Tago, T., et al., *Selective production of isobutylene from acetone over alkali metal ion-exchanged BEA zeolites.* Catalysis Today, 2011. **164**(1): p. 158-162.
21. Yang, P., et al., *One-step synthesis of methyl isobutyl ketone from acetone over Pd/MCM-22 zeolites.* Journal of Molecular Catalysis A: Chemical, 2007. **272**(1-2): p. 75-83.
22. Panov, A. and J. Fripiat, *Poisoning of aldol condensation reaction with H2O on acid catalysts.* Catalysis letters, 1999. **57**(1-2): p. 25-32.
23. Dumitriu, E., et al., *The aldol condensation of lower aldehydes over MFI zeolites with different acidic properties.* Microporous and Mesoporous Materials, 2001. **43**(3): p. 341-359.
24. Gayubo, A.G. and A.T. Aguayo, *Transformation of oxygenate components of biomass pyrolysis oil on a HZSM-5 zeolite. II. Aldehydes, ketones, and acids.* Industrial & …, 2004: p. 2619-2626.
25. Salvapati, G.S., K.V. Ramanamurty, and M. Janardanarao, *Selective catalytic self-condensation of acetone.* Journal of Molecular Catalysis, 1989. **54**(1): p. 9-30.
26. Melo, L., et al., *Acetone transformation into methyl isobutyl ketone over Pt/HMFI catalysts. IV. Effect of density and strength of the acidic sites.* Catalysis letters, 1999. **60**: p. 217-222.
27. Melo, L., et al., *Effect of the metallic/acid site (nPt/nA) ratio on the transformation of acetone towards methyl isobutyl ketone.* Catalysis letters, 1997. **44**: p. 201-204.
28. Melo, L., et al., *Synthesis of methyl isobutyl ketone using Pt–H ZSM5 bifunctional catalysts. III. Effect of the nPt/nA parameter on the xPt–H ZSM5 (y) catalysts.* Catalysis letters, 1998. **51**: p. 207-212.
29. Melo, L., et al., *Acetone transformation over Pt/H[Al]ZSM5 and Pt/H[Ga]ZSM5 catalysts.* Journal of Molecular Catalysis A: Chemical, 2002. **177**(2): p. 281-287.
30. Vannice, M. and B. Sen, *Metal-support effects on the intramolecular selectivity of crotonaldehyde hydrogenation over platinum.* Journal of Catalysis, 1989. **78**(115): p. 65-78.
31. Marinelli, T., S. Nabuurs, and V. Ponec, *Activity and Selectivity in the Reactions of Substituted α,β-Unsaturated Aldehydes.* Journal of Catalysis, 1995. **151**(2): p. 431-438.
32. Grimme, S., S. Ehrlich, and L. Goerigk, *Effect of the Damping Function in Dispersion Corrected Density Functional Theory.* Journal of computational chemistry, 2011. **32**(7): p. 1456-1465.
33. Grimme, S., et al., *A consistent and accurate ab initio parametrization of density functional dispersion correction (DFT-D) for the 94 elements H-Pu.* The Journal of Chemical Physics, 2010. **132**(15): p. 154104.
34. First, E.L., et al., *Computational characterization of zeolite porous networks: an automated approach.* Physical chemistry chemical physics : PCCP, 2011. **13**(38): p. 17339-58.
35. Macht, J., R.T. Carr, and E. Iglesia, *Consequences of Acid Strength for Isomerization and Elimination Catalysis on Solid Acids.* Journal of the American Chemical Society, 2009. **131**: p. 6554-6565.

36. Jones, A.J., et al., *Acid strength and solvation in catalysis by MFI zeolites and effects of the identity, concentration and location of framework heteroatoms.* Journal of Catalysis, 2014. **312**: p. 58-68.
37. Gounder, R., et al., *Solvation and acid strength effects on catalysis by faujasite zeolites.* Journal of Catalysis, 2012. **286**: p. 214 - 223.
38. Deshlahra, P., R.T. Carr, and E. Iglesia, *Ionic and Covalent Stabilization of Intermediates and Transition States in Catalysis by Solid Acids.* Journal of the American Chemical Society, 2014. **136**: p. 15229-15247.
39. Carr, R.T., M. Neurock, and E. Iglesia, *Catalytic consequences of acid strength in the conversion of methanl to dimethyl ether.* Journal of Catalysis, 2011. **278**: p. 78-93.
40. Skeels, G.W. and D.W. Breck, *Silicon substituted Y zeolite composition LZ-210* 1987, Union Carbide Corporation: United States. p. 26.
41. Corma, A., V. Fornés, and F. Rey, *Extraction of extra-framework aluminium in ultrastable Y zeolites by $(NH_4)_2SiF_6$ treatments.* Applied Catalysis, 1990. **59**: p. 267-274.
42. Baerlocher, C. and L.B. McCusker. *Database of Zeolite Structures.* February 6, 2016]; Available from: http://www.iza-structure.org/databases/.
43. Jones, A.J., S.I. Zones, and E. Iglesia, *Implications of Transition State Confinement within Small Voids for Acid Catalysis.* The Journal of Physical Chemistry …, 2014. **118**(31): p. 17787-17800.
44. Sarazen, M. and E. Iglesia, *unpublished results*. 2016.
45. Levenspiel, O., *Experimental Search for a Simple Rate Equation to Describe Deactivating Porous Catalyst Particles.* Journal of Catalysis, 1972. **25**: p. 265-272.
46. Zhao, Y.H., M.H. Abraham, and A.M. Zissimos, *Fast calculation of van der Waals volume as a sum of atomic and bond contributions and its application to drug compounds.* The Journal of organic chemistry, 2003. **68**(19): p. 7368-7373.
47. Foster, M.D., et al., *A geometric solution to the largest-free-sphere problem in zeolite frameworks.* Microporous and Mesoporous Materials, 2006. **90**(1-3): p. 32-38.
48. Kresse, G. and J. Hafner, *Ab initio molecular dynamics for liquid metals.* Physical Review B, 1993. **47**: p. 558-561.
49. Kresse, G. and J. Hafner, *Ab initio molecular-dynamics simulation of the liquid-metal–amorphous-semiconductor transition in germanium.* Physical Review B, 1994. **49**: p. 14251-14269.
50. Kresse, G. and J. Furthmüller, *Efficiency of ab-initio total energy calculations for metals and semiconductors using a plane-wave basis set.* Computational Materials Science, 1996. **6**: p. 15-50.
51. Kresse, G. and J. Furthmüller, *Efficient iterative schemes for ab initio total-energy calculations using a plane-wave basis set.* Physical Review B, 1996. **54**: p. 11169-11186.
52. Blöchl, P.E., *Projector augmented-wave method.* Physical Review B, 1994. **50**: p. 17953-17979.
53. Kresse, G. and D. Joubert, *From ultrasoft pseudopotentials to the projector augmented-wave method.* Physical Review B, 1999. **59**: p. 1758-1775.
54. Yang, K., et al., *Tests of the RPBE, revPBE, tau-HCTHhyb, omegaB97X-D, and MOHLYP density functional approximations and 29 others against representative databases for diverse bond energies and barrier heights in catalysis.* The Journal of chemical physics, 2010. **132**: p. 164117.

55. Perdew, J.P., K. Burke, and M. Ernzerhof, *Generalized Gradient Approximation Made Simple.* Physical Review Letters, 1996. **77**(18): p. 3865-3868.
56. Lee, K., et al., *Higher-accuracy van der Waals density functional.* Physical Review B, 2010. **82**: p. 081101.
57. Klimeš, J., D.R. Bowler, and A. Michaelides, *Van der Waals density functionals applied to solids.* Physical Review B, 2011. **83**(19): p. 195131.
58. Román-Pérez, G. and J.M. Soler, *Efficient Implementation of a van der Waals Density Functional: Application to Double-Wall Carbon Nanotubes.* Physical Review Letters, 2009. **103**(9): p. 096102.
59. Dion, M., et al., *Van der Waals Density Functional for General Geometries.* Physical Review Letters, 2004. **92**(24): p. 246401.
60. van Koningsveld, H., H. van Bekkum, and J.C. Jansen, *On the location and disorder of the tetrapropylammonium (TPA) ion in zeolite ZSM-5 with improved framework accuracy.* Acta Crystallographica Section B Structural Science, 1987. **43**: p. 127-132.
61. Olson, D.H., et al., *Crystal structure and structure-related properties of ZSM-5.* The Journal of Physical Chemistry, 1981. **85**: p. 2238-2243.
62. Momma, K. and F. Izumi, *VESTA: a three-dimensional visualization system for electronic and structural analysis.* Journal of Applied Crystallography, 2008. **41**: p. 653-658.
63. Jónsson, H., G. Mills, and K.W. Jacobsen, *Nudged elastic band method for finding minimum energy paths of transitions,* in *Classical and Quantum Dynamics in Condensed Phase Simulations*, B.J. Berne, G. Ciccotti, and D.F. Coker, Editors. 1998, World Scientific. p. 385-404.
64. Henkelman, G. and H. Jónsson, *A dimer method for finding saddle points on high dimensional potential surfaces using only first derivatives.* The Journal of Chemical Physics, 1999. **111**(15): p. 7010.
65. Deshlahra, P., et al., *Mechanistic Details and Reactivity Descriptors in Oxidation and Acid Catalysis of Methanol.* ACS Catalysis, 2015. **5**(2): p. 666-682.
66. Campbell, C.T. and J.R.V. Sellers, *Enthalpies and Entropies of Adsorption on Well-Defined Oxide Surfaces : Experimental Measurements.* Chemical reviews, 2013. **113**: p. 4106-4135.
67. Eyring, H., *The Activated Complex in Chemical Reactions.* The Journal of Chemical Physics, 1935. **3**(2): p. 107-115.
68. Evans, M.G. and M. Polanyi, *Some applications of the transition state method to the calculation of reaction velocities, especially in solution.* Transactions of the Faraday Society, 1935. **31**: p. 875-894.
69. Lennard-Jones, J.E., *Cohesion.* The Proceedings of the Physical Society, 1931. **43**(5): p. 461-482.
70. Lennard-Jones, J.E., *On the Determination of Molecular Fields - II. From the Equation of State of a Gas.* Proceedings of the Royal Society of London, 1924. **106**(738): p. 463-477.
71. Löwdin, P.-O., *On the Non-Orthogonality Problem Connected with the Use of Atomic Wave Functions in the Theory of Molecules and Crystals.* The Journal of Chemical Physics, 1950. **18**(3): p. 365-375.
72. Qian, X., et al., *Quasiatomic orbitals for ab initio tight-binding analysis.* Physical Review B - Condensed Matter and Materials Physics, 2008. **78**(24): p. 1-22.

73. Lu, W.C., et al., *Molecule intrinsic minimal basis sets. I. Exact resolution of ab initio optimized molecular orbitals in terms of deformed atomic minimal-basis orbitals.* The Journal of chemical physics, 2004. **120**(6): p. 2629-2637.
74. Lu, W.C., et al., *Representation of electronic structures in crystals in terms of highly localized quasiatomic minimal basis orbitals.* Physical Review B - Condensed Matter and Materials Physics, 2004. **70**(4): p. 1-4.
75. Chan, T.L., et al., *Highly localized quasiatomic minimal basis orbitals for Mo from ab initio calculations.* Physical Review B - Condensed Matter and Materials Physics, 2007. **76**(20): p. 1-10.
76. Deserno, M., *How to generate equidistributed points on the surface of a sphere*, M.-P.-I.f. Polymerforshung, Editor. 2004.
77. Lee, J.W., J.B. Butt, and D.M. Downing, *Kinetic, transport, and deactivation rate interactions on steady state and transient responses in heterogeneous catalysis.* AIChE Journal, 1978. **24**(2): p. 212-222.
78. Wolf, E.E. and E.E. Petersen, *On the kinetics of self-poisoning catalytic reactions.* Journal of Catalysis, 1977. **47**(1): p. 28-32.
79. Baertsch, C.D., et al., *Genesis of Brønsted Acid Sites during Dehydration of 2-Butanol on Tungsten Oxide Catalysts.* Journal of Catalysis, 2002. **205**: p. 44-57.
80. Boekfa, B., et al., *Adsorption and Tautomerization Reaction of Acetone on Acidic Zeolites: The Confinement Effect in Different Types of Zeolites.* The Journal of Physical Chemistry C, 2010. **114**(35): p. 15061-15067.
81. Pelmenschikov, A., et al., *(A, B, C) triplet of infrared OH bands of zeolitic H-complexes.* Journal of physical chemistry, 1995. **99**(11): p. 3612-3617.
82. Lamberti, C., et al., *Probing the surfaces of heterogeneous catalysts by in situ IR spectroscopy.* Chemical Society reviews, 2010. **39**(12): p. 4951-5001.
83. Parker, L.M., D.M. Bibby, and G.R. Burns, *FTIR spectra of bases sorbed on H+ZSM-5 - A study of hydrogen bonding*, P.A. Jacobs and R. van Santen, Editors. 1989, Elsevier. p. 963-972.
84. Kubelková, L., J. Čejka, and J. Nováková, *Surface reactivity of ZSM-5 zeolites in interaction with ketones at ambient temperature (a FT-i.r. study).* Zeolites, 1991. **11**(1): p. 48-53.
85. Crossee, P. and J.H. Schachtschneider, *Vibrational analysis of acetone, acetaldehyde, and formaldehyde.* The Journal of chemical physics, 1966. **44**(97): p. 97-11.
86. Pimentel, G.C. and A.L. McClellan, *Hydrogen Bonding.* Annual Review of Physical Chemistry, 1971. **22**: p. 347-385.
87. Xu, M., W. Wang, and M. Hunger, *Formation of acetone enol on acidic zeolite ZSM-5 evidenced by H/D exchange.* Chemical communications (Cambridge, England), 2003(6): p. 722-3.
88. Bondi, A., *van der Waals Volumes and Radii.* The Journal of Physical Chemistry, 1964. **68**(3): p. 441-451.
89. Sklenak, S., et al., *Aluminum siting in silicon-rich zeolite frameworks: A combined high-resolution 27Al NMR spectroscopy and quantum mechanics/molecular mechanics study of ZSM-5.* Angewandte Chemie - International Edition, 2007. **46**(38): p. 7286-7289.
90. Cejka, J., et al., *Zeolite-based materials for novel catalytic applications: Opportunities, perspectives and open problems.* Catalysis Today, 2012. **179**(1): p. 2-15.

91. Rigby, A.M., G. Kramer, and R. van Santen, *Mechanisms of Hydrocarbon Conversion in Zeolites: A Quantum Mechanical Study.* Journal of Catalysis, 1997. **170**(1): p. 1-10.

Chapter 3

Kinetic and mechanistic assessments of acetone conversion to isobutene and acetic acid on solid Brønsted acid catalysts

Abstract

Solid Brønsted acids catalyze aldol condensation reactions that grow carbon chains using oxygenate molecules; these catalysts, however, deactivate rapidly and catalyze β-scission reactions that break C-C bonds. Acetone condensation on solid acids shows significant selectivities to isobutene (C_4), yet mechanistic details of this conversion remains elusive. Here, we studied acetone condensation on a series of microporous and mesoporous aluminosilicates (FER, TON, MFI, BEA, MCM-41), and selectivity to C_4 species was the highest on MFI samples as determined by rigorous comparison of lumped rate constants derived from selectivity dependences on acetone conversion and acetone and H_2O pressures. Measurements of these effects also indicate that C_6 (ketol and alkenone) intermediates are quasi-equilibrated with each other and present at pseudo-steady state. Detailed analysis of the effects of H_2O, which determines the relative concentrations of C_6-alkenones and their ketol precursors, reveals two β-scission pathways with distinct site requirements. One route involves the β-scission of ketol species and occurs exclusively on protons. The second, and predominant route at low H_2O pressures, involves the β-scission of C_6-alkenones or their tautomers. The selectivity toward this second pathway increased sharply with decreasing proton densities (increasing Si/Al ratios) on a series of MFI samples, even though acetone condensation turnover rates (per proton) remain unchanged. These selectivity trends are not consistent with diffusion-enhanced secondary reactions or bifunctional mechanisms, but rather indicate a mechanism where a highly reactive C_6-alkenol is formed on protons and decomposes in vicinal confining voids forming stable β-scission products via free-radical pathways. These voids provide van der Waals stabilization to chain propagation transition states, even without the presence of protons, based on their size and shape. Consistent with C_4 selectivity measurements, β-scission rates from these reaction pathways are proportional to both the number of initiation sites (protons) and propagation locations (voids). The plausible involvement of these free radical reaction pathways is also consistent with coupled cluster (CCSD) calculations free energies of gaseous intermediates and radical species.

3.1 Introduction

Reaction pathways to produce branched olefins from biomass-derived molecules are critical with the increased use of biomass feedstocks [1]. One such pathway is the conversion of acetone into isobutene (C_4), a valuable precursor for the production of butyl rubber and polyisobutylene [2, 3]. The conversion of acetone into C_4 has been studied on a variety of solid acids including: amorphous oxides (Si-Al, Si-W) and crystalline aluminosilicates (MFI, BEA, ERI, FAU) [4-10]. The mechanistic details of these reactions, however, remain unclear due to rapid subsequent reactions on acid sites at the elevated temperatures used ($\geq$ 573 K), such as isomerization, oligomerization, and ketonization [11, 12], which consume initial products and lead to catalyst deactivation [7] (Chapter 2).

Initial conversions of alkanones on solid acids form dimer β-ketol by aldol condensation pathways, which even proceed at ambient temperature in the presence of protons [13]. These reactive β-ketol species readily dehydrate on acid sites to form α,β-unsaturated alkanones [14, 15]. Conversion of β-ketol and α,β-unsaturated alkanone products from acetone condensation (diacetone alcohol and mesityl oxide, respectively) were first reported in 1940 by McAllister and co-workers, where they showed that these C_6 species are precursors to isobutene formation by feeding each species over a silica-phosphoric acid catalyst [16], and they postulated that the hydrolytic cleavage of α,β-unsaturated alkanones on acid sites is the predominant reaction pathway. More recent studies using zeolite catalysts have led to conflicting reports on some of the key mechanistic details of C_4 formation from acetone condensation, including: (1) the precursors of C_4 formation (mesityl oxide, diacetone alcohol, trimer oxygenate products, or larger unsaturated species) [7-10], (2) the active site for C_4 formation (Brønsted acid site or Lewis acid site) [10, 17], (3) the effects of H_2O pressure on catalyst stability and C_4 selectivity [7, 17], and (4) the effects of catalyst Si/Al ratio on C_4 selectivity [7, 8, 10, 18].

Here, we address each of these issues and construct a plausible set of elementary steps for C_4 formation from acetone by measuring condensation rates and selectivities on a range of aluminosilicates (FER, TON, MFI, BEA, MCM-41) at low acetone conversions ($\leq$ 6 %) and low reaction temperature (453-483 K) to prevent subsequent reactions. In our previous work on acetone condensation on aluminosilicates (FER, TON, MFI, BEA, FAU, MCM-41), we were able to stabilize condensation rates via addition of a hydrogenation function (Pt clusters and H_2) and determined that condensation rates are first-order in acetone pressure (463-483 K, 0.1-5.0 kPa acetone; Chapter 2). The study, further, concluded that C-C bond formation, occurring on protons saturated in H-bonded acetone, is kinetically-relevant for acetone condensation on aluminosilicates at these conditions. These measured first-order dependences on acetone pressure (Ac) and mechanistic interpretations yield a condensation rate expression (per proton):

$$\frac{r_{\text{cond}}}{[H^+]} = k_{\text{cond}}(\text{Ac}) \qquad (1)$$

where k_{cond} is the first-order rate constant. Here, we build on these findings by using aluminosilicates without the presence of a metal function.

Rate and selectivity measurements during catalyst deactivation provide insight into effects of reactant conversion on product selectivities and potential methods to inhibit catalyst deactivation. These measurements indicate that C_4 formation from acetone occurs via a quasi-equilibrated pool of C_6 β-ketol and α,β-unsaturated alkanone intermediates (C_6-pool), which are present at pseudo-steady state concentrations; thus, precluding the formation of C_4 from oligomerization-cracking cycles of C_{9+} products, consistent with C_{13}-labelling studies that find three of the four C-atoms in C_4 are derived from the same acetone molecule [6]. We identify two distinct C_4 formation pathways from the C_6-pool, which are distinguished by H_2O pressure dependence. The H_2O-assisted pathway occurs exclusively on protons, as determined by using MFI samples of different proton densities; this pathway is referred to as the β-scission of diacetone alcohol (DA; Scheme 1) here, but is indistinguishable from any other β-scission pathway mediated by a transition state of similar composition (such as the hydrolytic cleavage of mesityl oxide). The second pathway, referred to as the β-scission of mesityl oxide species (MO; Scheme 1), is the predominant C_4 formation pathway in the absence of added H_2O (dry conditions) and is most

effectively catalyzed by MFI. This pathway leads to C_4 selectivities that increase with decreasing proton density (increasing Si/Al ratio)—a result that has been reported previously [7, 8, 18]—somewhat unexpectedly suggesting that protons are not the active sites but instead this pathway is proportional to both protons and microporous volume. The addition pure silica MFI (silicate-1, SIL-1) in physical mixtures with Al-MFI, however, showed no additional conversion to C_4 consistent with the active site for MO β-scission requiring both microporous volume and nearby protons in close (intracrystal) proximity.

Such active site requirements for MO β-scission cannot be explained by bifunctional catalysis mechanisms or the presence of non-framework Al acting as Lewis acid centers or silanols acting as weak Brønsted acids; instead these requirements are consistent with free-radical pathways. Similar pathways have been determined for the thermal decomposition of mesityl oxide (C_6 α,β-unsaturated alkanone) at elevated temperatures (685-763 K) [19], which occur in the absence of a catalyst to convert mesityl oxide to more reactive C_6-species such as alkenol species; reactions that are efficiently catalyzed by protons [20]. Confining voids, present in microporous solids (FER, TON, MFI, BEA), have also been reported to reduce activation barriers and required reaction temperatures by stabilizing transition states via van der Waals interactions [21], which increase enthalpic stabilization at the cost of entropic losses. The plausibility of protons forming highly-reactive C_6 species, which propagate free radical chain reaction via β-scission in the vicinal confining voids, are further investigated by using coupled calculations to estimate free energies of C_6 intermediates and radical species. These theoretical treatments suggest that free-radical β-scission pathways catalyzed by the combination of protons and vicinal confining voids are the only plausible explanation for the measured rates and C_4 selectivities on aluminosilicates.

3.2 Methods

3.2.1 Catalyst synthesis protocols

All catalysts used were the same samples and preparations as those reported previously (Chapter 2). NH_4^+-MFI (Zeolyst, Si/Al_{tot} = 16.6, 29.2, 43.8, and 168.3), NH_4^+-BEA (Zeolyst, Si/Al_{tot} = 43.3), NH_4^+-FER (Zeolyst, Si/Al_{tot} = 10.3), NH_4^+-TON (BP p.l.c., Si/Al_{tot} = 40.0), and NH_4^+-MCM-41 (Sigma-Aldrich, 643653, Si/Al_{tot} = 37.8) were treated in flowing dry air (1.5 cm^3 g^{-1} s^{-1}, zero grade, Praxair) heated to 823 K (at 0.025 K s^{-1}) and held for 5 h. Si, Al, and Na contents were measured by inductively-coupled plasma atomic emission spectroscopy (ICP-AES; Galbraith Laboratories). Table 1 lists the sample nomenclature, provenance, Si/Al ratio, H^+/Al ratio, and proton densities. Void sizes of these frameworks, shown in Table 1, are described by two metrics: (1) the largest inscribed sphere (largest cavity diameter) and (2) the largest sphere that can traverse each framework (pore-limiting diameter), each metric is derived from crystallographic data [22].

SIL-1 (silicate-1, pure silica MFI) samples were prepared using previously reported protocols [21], where fumed SiO_2 (Cabosil M5) was added to a solution of tetrapropylammonium hydroxide (TPAOH; Alfa Aesar, 40% wt.) and stirred for 2h; then aqueous HF was added (Alfa Aesar, 48% wt.) and stirred for 4 h. The gel (1 SiO_2/0.1 TPAOH/ 0.1 HF/33 H_2O molar ratios; pH = 5.5) was placed within a Teflon-lined stainless steel autoclave (Parr; 23 cm^3) and heated to 448 K under autogenous pressure for 14 days without stirring. The resulting solution was cooled to ambient temperature and filtered to recover the solids. These solids were washed with deionized

H_2O (>17.6 Ω cm resistivity) until the pH of the filtrate was lower than 9, and then dried at ambient temperature in ambient air for 8 h. The solids were then heated to 823 K (at 0.05 K s^{-1}) in ambient air and held for 6 h to remove the TPAOH.

Table 1: Zeolite and mesoporous aluminosilicate sample information

Zeolite	Provenance	Si/Al ratio[a]	H^+/Al	$H^+/g_{zeolite}$[e]	d_{LCD}[f] (nm)	d_{PLD}[g] (nm)
MFI-1	Zeolyst	16.6	0.65[b]	0.620	0.70	0.50
MFI-2	Zeolyst	29.2	0.77[b]	0.422	0.70	0.50
MFI-3	Zeolyst	43.8	1.03[b]	0.382	0.70	0.50
MFI-4	Zeolyst	168.3	0.70[b]	0.070	0.70	0.50
BEA	Zeolyst	43.3	1.04[c]	0.404	0.69	0.67
FER	Zeolyst	9.5	0.35[b]	0.363	0.70	0.53
TON	BP p.l.c.	40.0	0.88[d]	0.357	0.57	0.57
MCM-41	Sigma-Aldrich	37.8	0.42[c]	0.182	2.50[h]	2.50[h]

[a] Elemental analysis (ICP-OES; Galbraith Laboratories).
[b] Determined from pyridine titrations during CH_3OH dehydration reactions at 433 K [23].
[c] From 2,6-di-*tert*-butylpyridine titrations during acetone condensation reactions at 473 K [Chapter 2].
[d] From the amount of NH_3 evolved from NH_4^+-exchanged samples [11].
[e] Proton density were calculated using Si/Al and H^+/Al values reported here and unit cell parameters that were reported on the International Zeolite Association (IZA) web site [24]
[f] Largest-cavity diameter [22].
[g] Pore-limiting diameter [22].
[h] Diameter of cylindrical channel reported by Sigma-Aldrich.

3.2.2 Catalytic rate and selectivity measurements

Condensation rates and selectivities were measured at low acetone conversion (< 5%) to maintain differential reaction conditions and a range of reaction temperatures (463-483 K). Catalyst powders (< 180 μm aggregates) were pressed into wafers (690 bar, 0.1 h), crushed, and sieved to retain 180-250 μm aggregates. A tubular quartz reactor (7.0 mm i.d.) was used to hold these aggregates (0.020-0.200 g), and a three-zone resistively-heated furnace (Applied Test Systems Inc., model number 3210) was used to maintain constant reaction temperature. This furnace was controlled by three independent controllers (Watlow Series 988), which used K-type thermocouples (Omega). The catalyst temperature was measured by a similar K-type thermocouple in contact with midpoint along the catalyst bed at the outer surface of the quartz reactor. Catalyst samples (Table 1) were treated in flowing dry air (83.3 cm^3 g^{-1} s^{-1}, Extra dry, Praxair) by heating to 818 K (at 0.025 K s^{-1}; 2 h hold) and subsequently cooled to reaction temperatures.

Liquid acetone (≥ 99.9%, Sigma-Aldrich) was pumped into He (UHP, Praxair) and H_2 (UHP, Praxair) streams using a syringe pump (Legato 100, KD Scientific) and vaporized in

transfer lines maintained at 403 K. Inlet and effluent streams were analyzed by gas chromatography (GC; Agilent 6890A) using flame ionization detection (FID) after chromatographic separation (HP-1 column, Agilent). Molecular speciation was confirmed using mass spectrometry (MKS Spectra Minilab) and known standards. Retention times and response factors were determined from known concentrations of these compounds: acetone (≥ 99.9%, Sigma-Aldrich), diacetone alcohol (≥ 98%, Santa Cruz Biotechnology), mesityl oxide (98%, Spectrum Chemical), isobutene (99.0%, Praxair), acetic acid (≥ 99.99%, Sigma Aldrich), and 1,3,5-trimethylbenze (98%, Sigma-Aldrich), methyl isobutyl ketone (99.5%, ACROS Organics).

Diacetone alcohol (DA), the initial acetone condensation product, was not detected among reaction products because its fast dehydration and favorable thermodynamics (Scheme 1) to mesityl oxide and H_2O lead to DA concentrations below chromatographic detection limits (3.5 x 10^{-13}-5.6 x 10^{-9} Pa DA). Here we also measure isomesityl oxide (Scheme 1) at amounts consistent with its equilibrium with mesityl oxide, and we the plausibility existence of tautomerization C_6-enol isomers at reaction conditions by estimating the differences in free energy between mesityl oxide and these C_6-enols (Scheme 1) using coupled cluster methods (discussed in Section 3.2.3).

Scheme 1: Reaction network for gaseous C_6-pool involving dehydration and tautomerization on Brønsted acid sites*

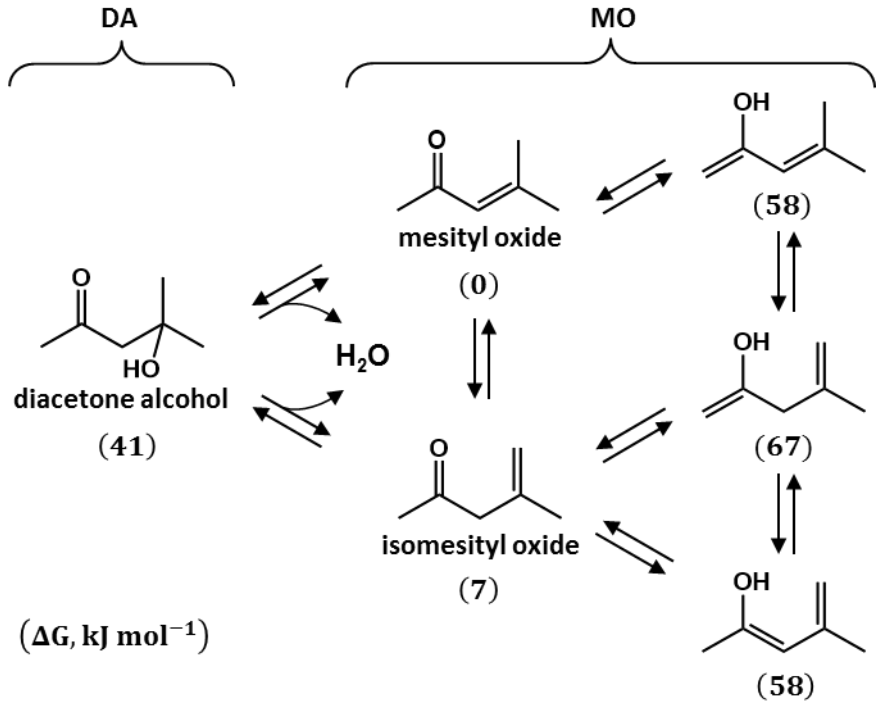

*Gibbs free energy differences between gaseous species and mesityl oxide are provided in parenthesis (473 K, CCSD, AUG-cc-pVDZ; discussed in Section 3.2.3). The value for diacetone alcohol is the free energy difference between gaseous diacetone alcohol and the sum of gaseous mesityl oxide and gaseous H_2O.

3.2.3 Coupled cluster treatments of gaseous intermediates and radical species

Electronic energies and vibrational frequencies of gaseous molecules (spin multiplicity = 1) and gaseous radicals (spin multiplicity = 2) were calculated using coupled cluster methods with single and double substitutions from the Hartee-Fock determinant (CCSD) [25-28] and Dunning's correlation-consistent, polarized valence, double-zeta basis set [29-31] with added angular momentum diffuse functions (AUG-cc-pVDZ) [29, 31] using Gaussian 09 [32]. Enthalpic and entropic corrections at reaction temperatures were determined from vibrational frequencies, and these corrections together with electron energies were used to calculate free energies, which were used to determine free energy thermodynamic barriers (ΔG):

$$\Delta G = \sum_{p}^{\text{products}} G_p - \sum_{r}^{\text{reactants}} G_r \qquad (2)$$

where G_i represents the free energy of a reactant (r) or product (p). Free energies of C_6 intermediates are shown in Scheme 1.

Thermodynamic free energy differences are used to estimate equilibrium constants (K_{eq}) for reactions between gaseous molecules:

$$K_{eq} = \exp\left(-\frac{\Delta G}{k_B T}\right) \qquad (3)$$

where k_B is the Boltzmann constant and T is the reaction temperature (K). These equilibrium constants, taken together with the measured pressures of reactant and product species ((X_i); $i = r$ or p, respectively; units: bar), are used to determine the approach to equilibrium (η) for a given reaction:

$$\eta = \frac{1}{K_{eq}} \frac{\prod_p^{\text{products}} (X_p)}{\prod_r^{\text{reactants}} (X_r)} \qquad (4)$$

3.3 Results and Discussions

3.3.1 Effect of acetone pressure on catalyst deactivation and product selectivity

Aluminosilicates of different frameworks and proton densities (FER, TON, MFI, BEA, MCM-41; Table 1) were used to investigate the elementary steps and site requirements for the conversion of acetone into isobutene (C_4). Rigorous mechanistic assessments and comparisons among samples require the determination of rate constants, which account for dependences of rate and selectivity on reaction conditions. Here, we use MFI as an example to develop a mechanism that is consistent with the measured effects of acetone pressure and acetone conversion on deactivation rates and C_4 selectivities.

Measured acetone condensation rates on MFI-3 decreased with time on stream at all acetone pressures (0.33-3.75 kPa acetone; Fig. 1); these rates were measured at low acetone conversions ($\leq$ 6%), which results in low product concentrations and negligible changes of acetone

pressure down the catalyst bed. Effective first-order rate constants (k_{cond}; Eq. 1), plotted in Figure 1 as measured condensation rate (per initial proton loaded ($H^+|_{t=0}$)) divided by acetone pressure, are independent of acetone pressure at zero time on stream and consistent both with values and acetone pressure dependence previously reported on Pt-stabilized MFI samples (Chapter 2). The k_{cond} values reported here decreased more rapidly with increasing acetone pressures (Fig. 1), and the curvature apparent at each acetone pressure suggests strong binding of a reaction product, which decreases in concentration as the catalyst deactivates.

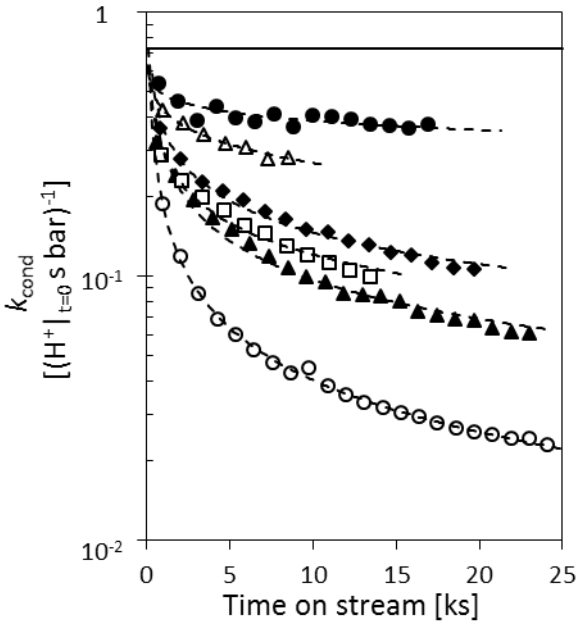

Figure 1: Effective condensation rate constant per initial proton loaded (k_{cond}; Eq 1) as a function of time on stream. Rates were measured on MFI-3 at 0.33 (filled circles), 0.50 (open triangles), 1.02 (filled diamonds), 1.53 (open squares), 1.93 (filled triangles), and 3.75 (open circles) kPa acetone pressure (balance He, 473 K). Horizontal solid line represents first-order condensation rate constant reported previously (Chapter 2) and dashed lines are trend lines to guide the eye.

Conversion of acetone on MFI, at the temperatures used here (453-483K), produced several detectable product groups: mesityl oxide and isomesityl oxide (C_6-alkenone condensation products (MO); Scheme 1), which were equilibrated with each other at all conditions studied (Chapter 2), and C_4 and acetic acid (β-scission products) that were formed in equimolar amounts (Chapter 2). The proportional increase of C_4/MO molar ratios with increasing acetone conversion (Fig. 2) suggests that β-scission is a subsequent reaction that converts either the C_6-products (equilibrated pool of DA and MO species, Scheme 1) or products formed from the C_6-pool (Scheme 2). Measured C_4/MO molar ratios also increased with decreasing acetone pressure (Fig 2), reflecting different acetone pressure dependences of C_4 and MO concentrations.

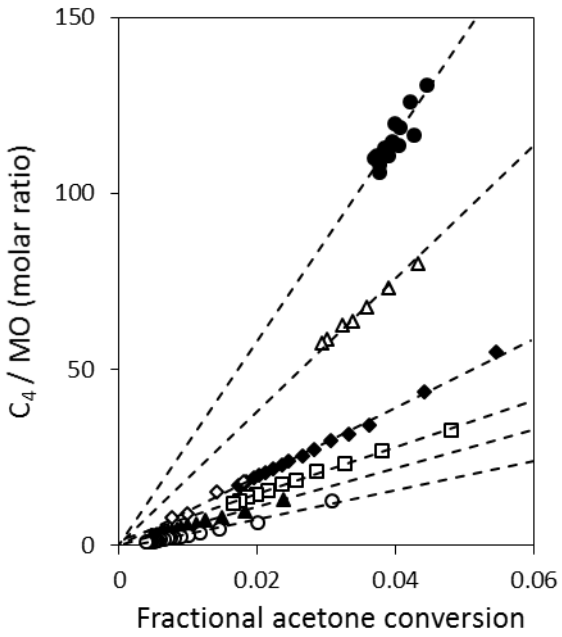

Figure 2: Effect of acetone conversion on C_4/MO molar ratio measured on MFI-3 at 0.33 (filled circles), 0.50 (open triangles), 1.02 (filled and open diamonds), 1.53 (open squares), 1.93 (filled triangles), and 3.75 (open circles) kPa acetone pressure (balance He, 473 K). Dashed lines are regressed linear fits of the data through the origin. Open diamonds are data points measured at different acetone residence times (6.6-15 ($H^+|_{t=0}$ s) acetone^{-1}); all other data points are measured while catalyst deactivates.

Here, acetone conversion was varied by catalyst deactivation with time on stream (Fig. 2) and by changing acetone residence time (open diamonds; Fig. 2); both methods of varying acetone conversion resulted in similar linear trends of C_4/MO ratios, which suggests either (1) the site that catalyzes condensation (protons) is also responsible for β-scission or (2) there are two distinguishable active sites where one catalyzes condensation (protons) and the other catalyzes β-scission (L_2; Scheme 2) and both active sites deactivate at the same rate.

Scheme 2: Serial reaction pathways to form isobutene and acetic acid from acetone on MFI[a]

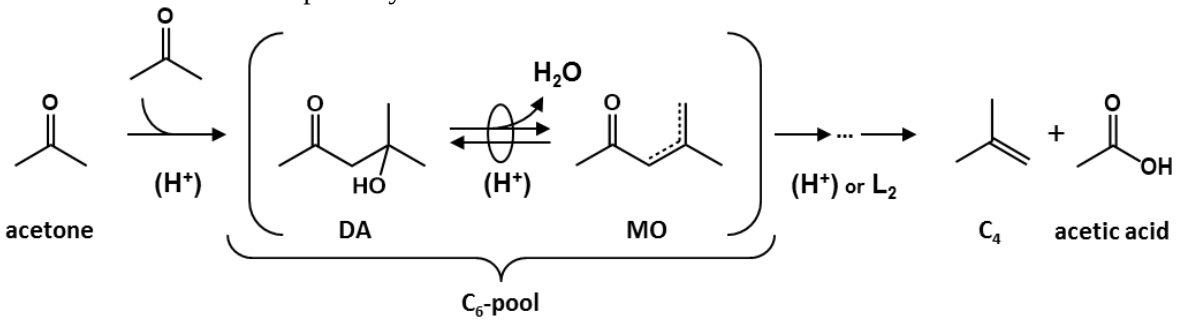

[a]Quasi-equilibrated C_6-pool is indicated by a circle over the double arrows and is shown in Scheme 1. Equilibrated double-bond isomers of MO are indicated by dotted lines for double bonds (MO). Reaction pathways are consistent with those previously reported [7, 14].

Measured C_4/MO molar ratios (Fig. 2) are much greater than unity, and MO pressures are independent of acetone conversion (Fig. 3a) and increased with the square of acetone pressure (Fig. 3b). These data reflect highly reactive C_6 species (Scheme 1) that are either equilibrated with acetone or present at pseudo-steady state. Equilibration of the C_6 species with acetone during condensation on MFI-3 is inconsistent with previous reports where the addition of a metal function, which hydrogenates MO to the corresponding saturated alkanones, did not result in an increase in condensation rate (Chapter 2). Here, we also use couple cluster theory calculations (CCSD), together with measured acetone and MO pressures, to determine the approach to equilibrium (η; Eq. 4) for the conversion of acetone to H_2O and mesityl oxide (the most stable C_6 species; Scheme 1). The maximum η value was 0.006, which is much less than unity and suggests that the C_6 species are far from equilibrium with acetone. Thus, we infer from these η values, previous reports, and constant MO pressure measured across a range of acetone conversion that MO species are present at pseudo-steady state concentrations during acetone condensation.

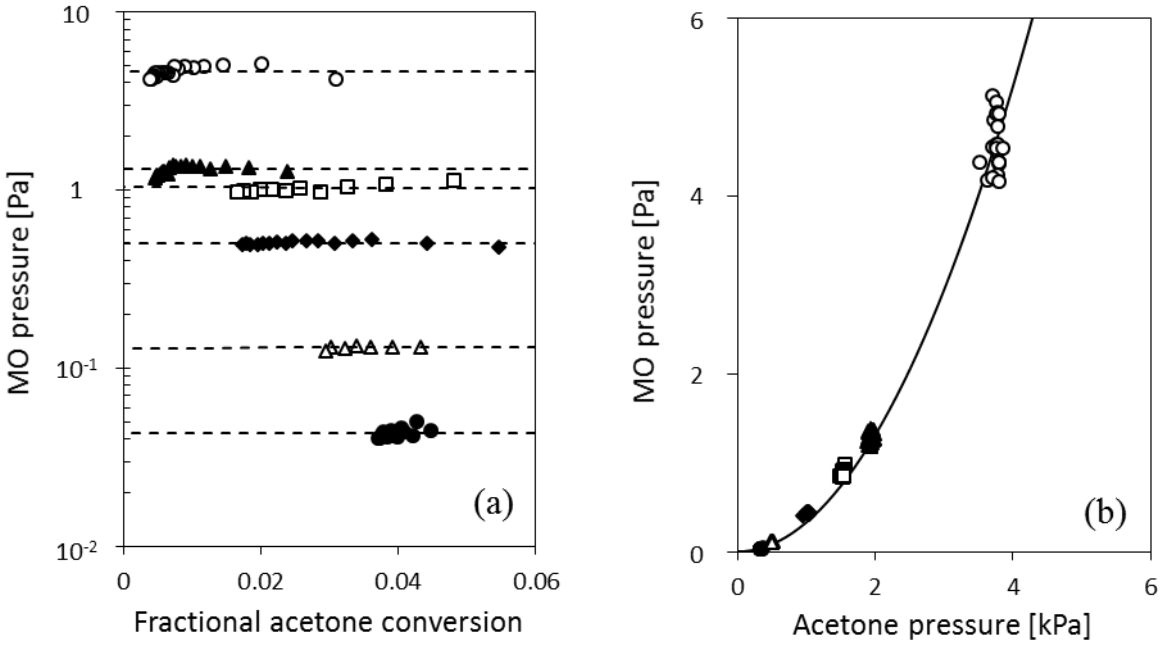

Figure 3: MO pressure (mesityl oxide and isomesityl oxide, Scheme 1) as a function of (a) acetone conversion and (b) acetone pressure on MFI-3 at 0.33 (filled circles), 0.50 (open triangles), 1.02 (filled diamonds), 1.53 (open squares), 1.93 (filled triangles), and 3.75 (open circles) kPa acetone pressure (balance He, 473 K). Dashed lines represent regressed linear fits of data with zero slope and solid line represents regressed fit of data to the form of Eq. 9.

Pseudo-steady state approximations require species are formed and depleted at equal rates:

$$r_{formation} = r_{consumption} \quad (5)$$

Here the formation rate ($r_{formation}$) of C_6 species is described by the acetone condensation rate (Scheme 2):

$$\frac{r_{formation}}{[H^+]} = \frac{k_{cond} K_{Ac} (\mathrm{Ac})^2}{K_{Ac} (\mathrm{Ac})} \qquad (6)$$

where k_{cond} and K_{Ac} are kinetic and thermodynamic constants, respectively, representing C-C bond formation and acetone adsorption on protons as shown in Scheme 3 The denominator term in Equation 6 represents that all protons are saturated with acetone, which is consistent with the favorable H-bonding of acetone on protons of aluminosilicates determined by infrared spectroscopy [33, 34] (Chapter 2).

Scheme 3: Plausible elementary steps for the formation of measured products MO, isobutene, and acetic acid from acetone on Brønsted acid sites[a]

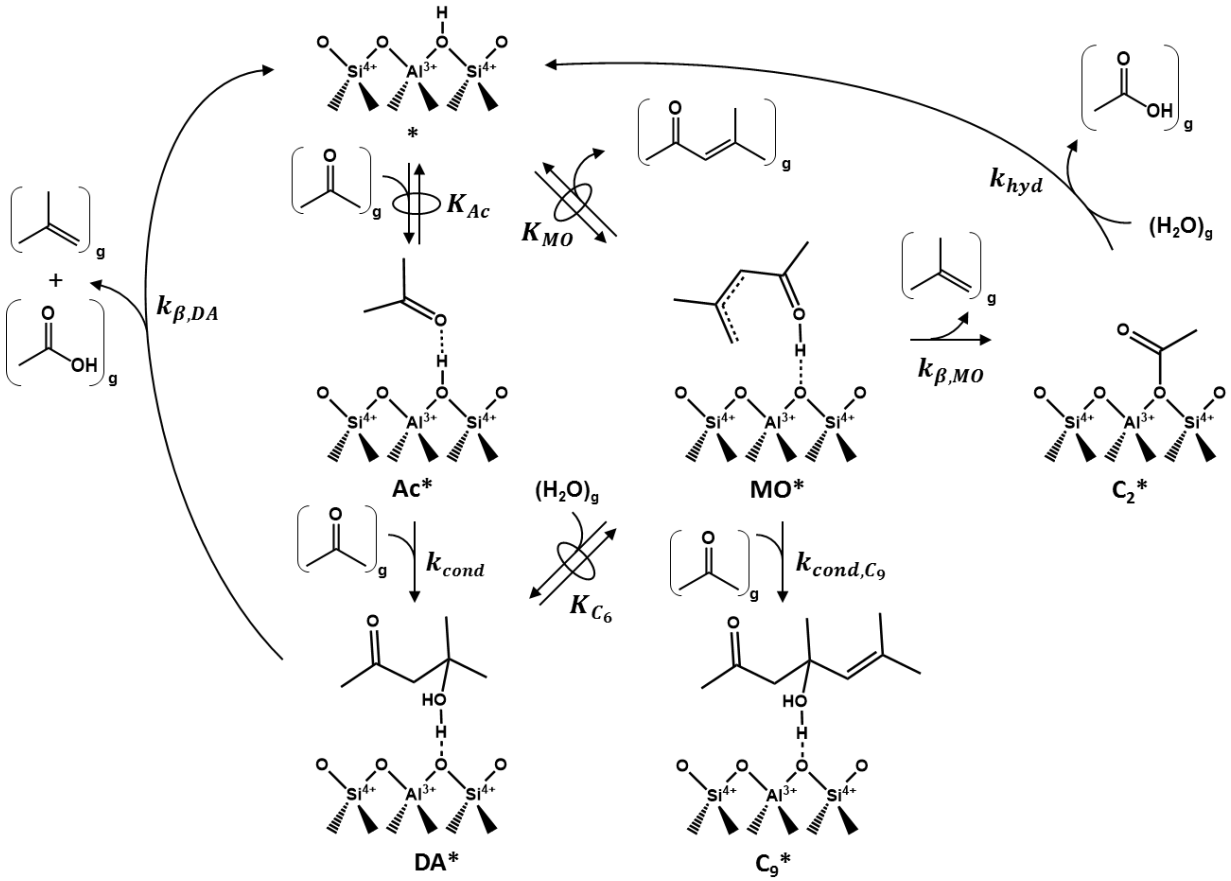

[a]Surface intermediate labels correspond to bare protons (*), H-bonded acetone (Ac*), protonated diacetone alcohol (DA*), protonated mesityl oxide (MO*), acetyl alkoxides (C_2*), and protonated C_9 β-ketol species (C_9*). k_X and K_X denote kinetic constants for forward steps and equilibrium constants, respectively. Quasi-equilibrated steps are indicated by a circle over the double arrows. Equilibrated double-bond isomers (Scheme 1) are indicated by dotted lines for double bonds (MO*).

The rate expression for the consumption of C_6 species ($r_{consumption}$; Eq. 5) is equivalent to the rate expression for C_4 formation because serial reaction pathway described above and MO and β-scission products are the only species detected (Scheme 2). C_4 formation has been proposed to occur via two pathways: (1) the β-scission of large condensation products (C_{9+}) on protons [9, 10] and (2) the β-scission of C_6 species (β-ketol or α,β-unsaturated alkenones) [7-10, 14, 16]. Here, we distinguish these proposed pathways by comparing the second-order acetone pressure dependence of measured MO pressures (Fig. 3b) with the acetone pressure dependence determined from the pseudo-steady state concentrations of C_6 species.

These proposals for consumption of C_6 species (Scheme 1) yield a combined rate expression:

$$\frac{\mathrm{r}_{consumption}}{[H^+]} = \frac{\frac{k_{\beta,DA}K_{MO}}{K_{C_6}}(\mathrm{MO})(\mathrm{H_2O})}{K_{Ac}(\mathrm{Ac})} + \frac{k_{\beta,MO}K_{MO}(\mathrm{MO})}{K_{Ac}(\mathrm{Ac})} + \frac{k_{cond,C_9}(\mathrm{Ac})K_{MO}(\mathrm{MO})}{K_{Ac}(\mathrm{Ac})} \quad (7)$$

where the three additive terms (from left to right) represent the respective rates of β-scission of diacetone alcohol (DA; C_6 β-ketol), β-scission of MO, and condensation of MO with acetone (Scheme 3). k_X and K_X are, respectively, the kinetic and thermodynamic constants for the elementary steps shown in Scheme 3. Here, the H_2O pressure can be considered equal to the MO pressure because there are no detectable products from other reaction pathways that produce H2O (Scheme 3). This assumption is consistent with measurements where H_2O is added (Section 3.3.3). Solving for the pseudo-steady state concentration of MO using Equations 6 and 7 yields:

$$(\mathrm{MO}) = \left(\frac{2k_{\beta,DA}}{K_{C_6}}\right)^{-1}\left(\sqrt{\left(k_{\beta,MO}+k_{cond,C_9}(Ac)\right)^2 + 4\frac{k_{\beta,DA}}{K_{C_6}}\frac{k_{cond}K_{Ac}}{K_{MO}}(\mathrm{Ac})^2} - \left(k_{\beta,MO}+k_{cond,C_9}(Ac)\right)\right) \quad (8)$$

Regression of the data in Figure 3b to the form of Equation 8 revealed the insensitivity of MO pressure to the terms corresponding to DA β-scission and condensation of MO with acetone. These conclusions suggest that β-scission of MO is the dominant pathway for the consumption of C_6 species and allows the simplification of Equation 8:

$$(\mathrm{MO}) = \frac{k_{cond}K_{Ac}}{k_{\beta,MO}K_{MO}}(\mathrm{Ac})^2 \quad (9)$$

consistent with the mechanistic interpretation that the C_6-pool is depleted by the reaction of MO on protons (or a secondary site, L_2; Scheme 2) saturated with acetone and mediated by transition states that do not require H_2O.

This assessment of the acetone pressure dependence of MO pressure (Eq. 9), in combination with Equation 1, provides mechanistic interpretation of the acetone pressure dependence of the C_4/MO molar ratio shown in Figure 2:

$$\frac{(C_4)}{(MO)} = \frac{\frac{1}{2}X(Ac)}{\frac{k_{cond}K_{Ac}}{k_{\beta,MO}K_{MO}}(Ac)^2} = \frac{1}{2}\frac{k_{\beta,MO}K_{MO}}{k_{cond}K_{Ac}}\frac{X}{(Ac)} \quad (10)$$

where X is the fractional acetone conversion and the ½-term represents the stoichiometry of the reaction converting acetone to isobutene; this representation of C_4 pressure reflects the first-order acetone pressure dependence of condensation (Eq. 1) and is sufficient when β-scission products are the major products ($\geq$ 90% carbon selectivity). Measured C_4/MO molar ratios collapse to a single linear dependence (Fig. 5) when plotted as a function of acetone conversion divided by acetone pressure (χ):

$$\chi \equiv \frac{X}{(Ac)} \quad (11)$$

consistent with Equation 9. The slope of this dependence allows rigorous comparisons of the collection of kinetic and thermodynamic constants (β_{MO}):

$$\beta_{MO} \equiv \frac{k_{\beta,MO}K_{MO}}{k_{cond}K_{Ac}} \quad (12)$$

for different aluminosilicate samples (subject of Section 3.3.2) without artifacts of acetone conversion and acetone pressure.

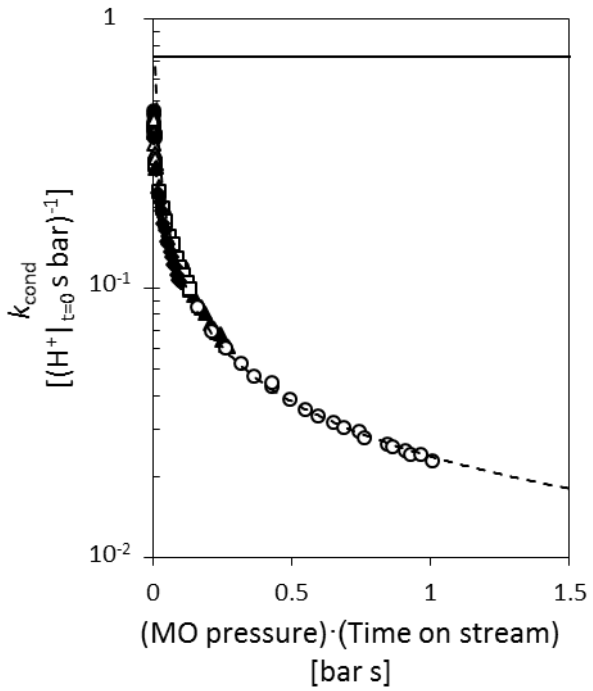

Figure 4: Effective condensation rate constant (per proton loaded) (k_{cond}; Eq 1) as a function of the product of time on stream and MO pressure. Rates were measured on MFI-3 at 0.33 (filled circles), 0.50 (open triangles), 1.02 (filled diamonds), 1.53 (open squares), 1.93 (filled triangles), and 3.75 (open circles) kPa acetone pressures (balance He, 473 K). Horizontal solid line represents first-order condensation rate constant reported previously (Chapter 2) and dashed line is a trend line.

Effective first-order rate constants determined at different acetone pressures (0.33-3.75 kPa acetone) on MFI-3 converged to a single curve when plotted as a function of the product time on stream and MO pressure (Fig. 4). The resulting monotonic dependence of these data (Fig. 4) is consistent with the reaction pathways depicted in Scheme 3, where MO species are precursors to larger products (C_{9+}) that form via subsequent condensations with acetone and block protons resulting in rapid decreases in condensation rates with time on stream (Chapter 2). Deactivation of the condensation rate (r_{cond}; Eq. 1) caused by these reaction pathways (Scheme 3) is described by [35]:

$$r_{\mathrm{cond}}(t) = r_{\mathrm{cond}}(0) \cdot \exp(-k_d(\mathrm{MO})t) \qquad (13)$$

where t is the time on stream and k_d is the deactivation rate constant (derivation of Eq. 13 is provided in Supporting Information, S1). The data plotted in Figure 4 is consistent with the monotonic dependence on the product of MO pressure and time on stream (Eq. 13); the curvature, however, in Figure 4 is not described by Equation 13. Such curvature, similar to Figure 1, indicates that these condensation products, which block protons, are formed at concentrations that decrease with decreasing acetone conversion.

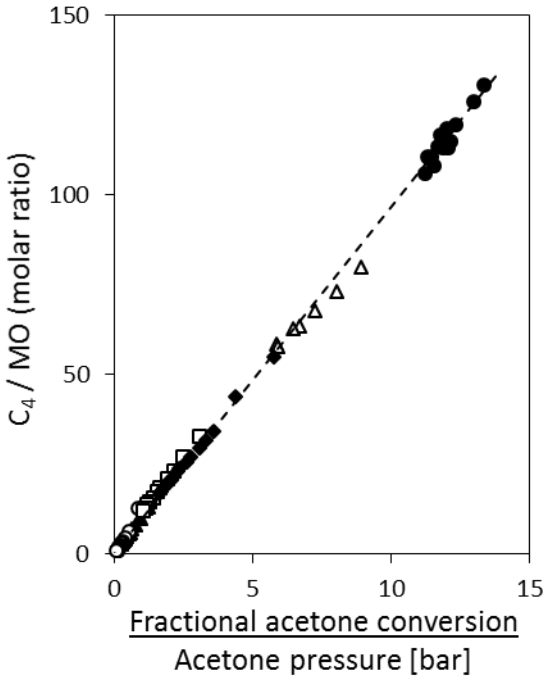

Figure 5: Effect of acetone conversion divided by acetone pressure on C_4/MO molar ratios measured on MFI-3 at 0.33 (filled circles), 0.50 (open triangles), 1.02 (filled diamonds), 1.53 (open squares), 1.93 (filled triangles), and 3.75 (open circles) kPa acetone pressures (balance He, 473 K). Dashed line is a regressed linear fit of the data through the origin.

The concomitant increase in deactivation rates and decrease in C_4 selectivity with increasing acetone pressure (Figs. 1 and 2, respectively) suggests that catalyst deactivation occurs via reaction pathways parallel to β-scission of MO (Eq. 7) and increasing selectivity toward β-scission inhibits catalyst deactivation by depleting the concentration of the C_6-pool. This mechanistic analysis, which rigorously accounts for acetone conversion and acetone pressure and provides methods to decrease deactivation rates, allows the comparison of β_{MO} values for aluminosilicates of different void environments (Section 3.3.2) that have been shown to catalyze acetone condensation through similar mechanisms (Chapter 2).

3.3.2 Consequences of void environment on product selectivity

C_4/MO molar ratios (C_4 selectivity) increased proportionally with increasing χ-values (Fig. 6) on all aluminosilicates (MFI-3, BEA, TON, FER, MCM-41) at various acetone pressures (0.1-4 kPa acetone); such trends suggest that the reaction pathway and chemical interpretations presented for MFI-3 (Eq. 10) are similar on these aluminosilicates. β-scission products and MO species were the only products measured on MFI-3, TON, and FER samples, consistent with the larger C_{9+} products having difficulty egressing through the channels present in these frameworks ($d_{PLD} \leq 0.57$ nm; Table 1). The large pore microporous and mesoporous samples (BEA (d_{PLD} = 0.67 nm) and MCM-41 (d_{PLD} = 2.5 nm); Table 1) produce 1,3,5-trimethylbenzene (C_9), in addition to MO species and β-scission products. C_9/MO molar ratios measured on BEA and MCM-41 also increased proportionally with increasing χ-values (Fig. 6b), consistent with the formation of these C_9 products via subsequent reactions of C_6 species (discussed in Section 3.3.1). The parallel

reaction pathways that convert C_6 species into C_4 and C_9 products (Scheme 3) suggest similar proportional dependences of C_4/MO and C_9/MO molar ratios with χ-values as shown in Figures 6a and 6b, respectively.

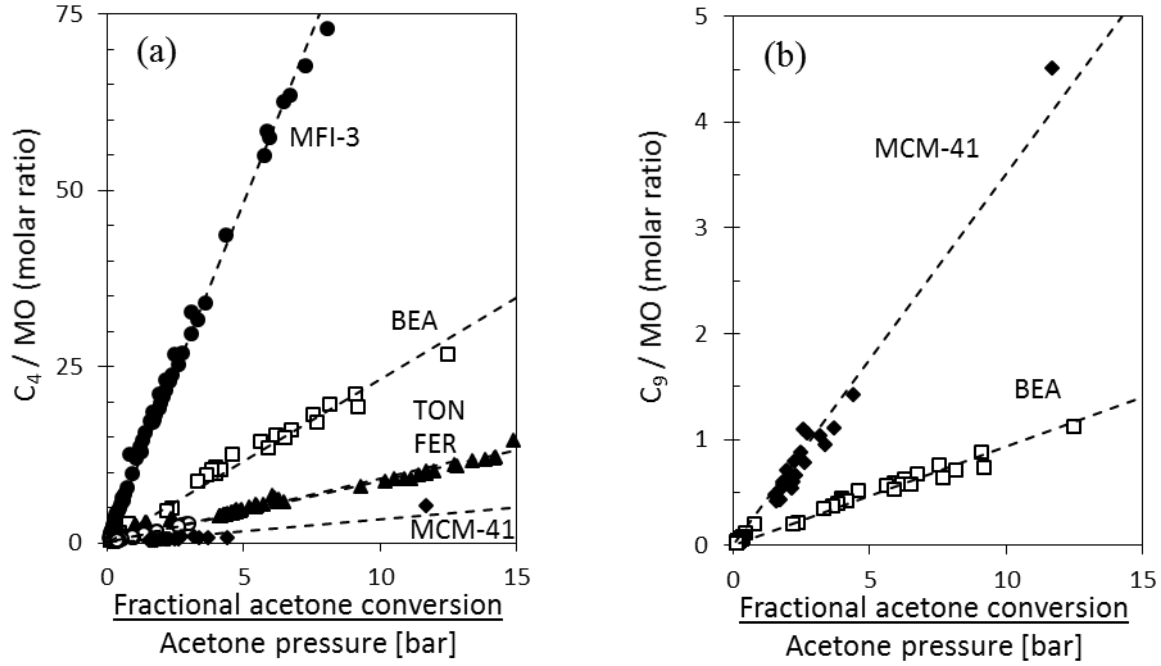

Figure 6: (a) C_4/MO and (b) C_9/MO molar ratios as functions of acetone conversion divided by acetone pressure (χ, Eq. 8) on aluminosilicates: MFI-3 (filled circles), BEA (open squares), TON (filled triangles), FER (open circles), and MCM-41 (filled diamonds); at 473 K, 0.1-4 kPa acetone. C_9 products were not measured on MFI-3, TON, or FER samples at these conditions. Dashed lines are regressed linear fits to the form of Equation 7.

Comparisons of β_{MO} values for aluminosilicates of different void environments, represented by the slopes of the linear dependences in Figure 6a and listed in Table 2, show that MFI-3 has the highest C_4 selectivity of these samples. The sharp increase in C_4 selectivity on MFI compared to the other aluminosilicates is presumably due to the preferential stabilization of β-scission transition states through van der Waals contacts with the surrounding void of MFI. The increased C_4 selectivity on MFI compared to the other aluminosilicates has led to many previous reports [6-8, 10, 36] and patents [37, 38] that focus on MFI for converting acetone into C_4, and here we use MFI as an example for developing a mechanistic understanding these conversions.

3.3.3 Effect of H_2O pressure on catalyst deactivation and product selectivity

Condensation reactions form unstable β-ketol species that readily undergo dehydration reactions (Scheme 2) forming alkanones and H_2O—species that have been implicated to increase or decrease rate of catalyst deactivation and affect selectivity toward C_4 species [7, 17]. We have shown previously that H_2O/acetone molar ratios must exceed 10 for a greater than 10% decrease in condensation rate (473 K, 0.1-10 kPa acetone) caused by H_2O binding to protons (Chapter 2);

thus, at the ratios we show here (H_2O/acetone molar ratios $\leq$ 3), added H_2O results in a negligible decrease in condensation rate (per proton).

The addition of gaseous H_2O into the reactant stream flowing over MFI-3 decreased deactivation rates and increased C_4/MO molar ratios compared to those measured without added H_2O (Figs.7 and 8, respectively). These data are consistent with the mechanistic interpretation presented in Section 3.3.1, which suggests increased H_2O pressure affects condensation selectivity and catalyst stability by shifting the equilibrium between β-ketol species and alkenones toward the β-ketol species (Scheme 2). The increase in C_4 selectivity with the addition of H_2O indicates the relevance of a second reaction pathway, the β-scission of DA (represented by the first term in Eq. 7), that depletes the C_6-pool (Scheme 1). These C_6 species undergo subsequent condensations (Section 3.3.1), and therefore decreases in C_6 concentration leads to decreases in deactivation rates.

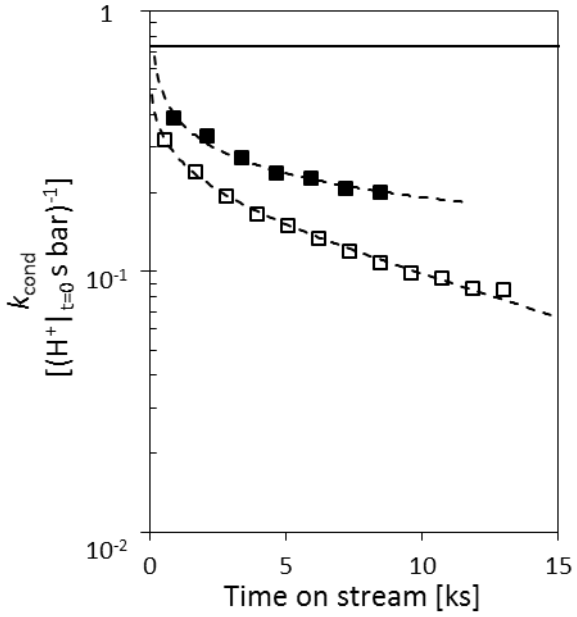

Figure 7: Effective condensation rate constant (k_{cond}; Eq 1) as a function of time on stream. Rates were measured on MFI-3 at 1.53 kPa acetone and 0 kPa H_2O added (open symbols), 1.56 kPa acetone 1.50 kPa H_2O (closed symbols) (balance He, 473 K). Horizontal solid line represents first-order condensation rate constant reported previously (Chapter 2) and dashed lines are trend lines.

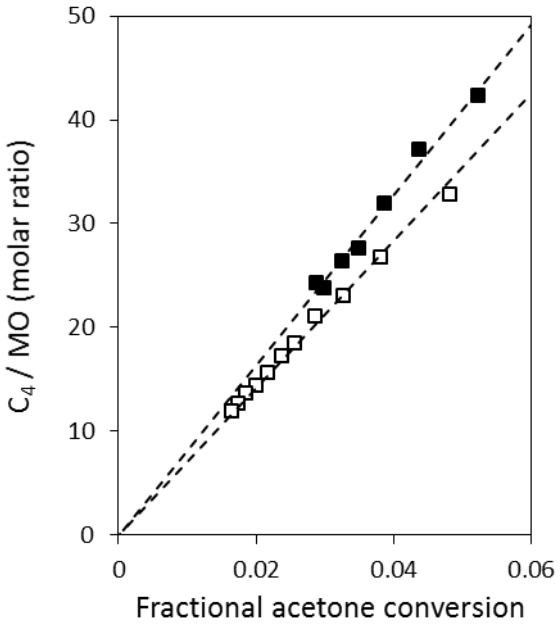

Figure 8: Effects of acetone conversion on C_4/MO molar ratios measured on MFI-3 at 1.53 kPa acetone and 0 kPa H_2O added (open symbols), 1.56 kPa acetone 1.50 kPa H_2O (closed symbols) (balance He, 473 K). Dashed lines are regressed linear fits of the data through the origin.

Gaseous H_2O added, in the reactant stream, at partial pressures much greater than those formed in the reactor (< 5 Pa H_2O formed during condensation) results in a constant H_2O pressure over the catalyst bed and requires reevaluation of the pseudo-steady state concentration of MO (Eq. 9):

$$(\mathrm{MO}) = \frac{k_{cond} K_{Ac} (\mathrm{Ac})^2}{\frac{k_{\beta,DA} K_{MO}}{K_{C_6}} (\mathrm{H_2O}) + k_{\beta,MO} K_{MO}} \tag{14}$$

Linearization of the H_2O pressure dependence of Equation 14 yields:

$$\frac{(\mathrm{Ac})^2}{(\mathrm{MO})} = \frac{k_{\beta,DA} K_{MO}}{k_{cond} K_{Ac} K_{C_6}} (\mathrm{H_2O}) + \frac{k_{\beta,MO} K_{MO}}{k_{cond} K_{Ac}} \tag{15}$$

which has two lumped parameters containing kinetic constants and thermodynamic constants (k_X and K_X, respectively; defined in Scheme 3). The $(\mathrm{Ac})^2/(\mathrm{MO})$ value at zero H_2O pressure (Eq. 15) is β_{MO} (Eq. 12) and each of the kinetic rate constants present in β_{MO} is related to a free energy barrier $(\Delta \mathrm{G}_X)$ under the formalism of transition-state theory [39, 40]:

$$k_X = \frac{k_B T}{h} \exp\left(-\frac{\Delta \mathrm{G}_X}{k_B T}\right) \tag{16}$$

where h is Planck's constant, k_B is the Boltzmann constant, and T is temperature (K). Equation 16 and 3 can be substituted into Equation 12 for each of the kinetic and thermodynamic constants to yield:

$$\beta_{MO} = \frac{\frac{k_B T}{h} \exp\left(-\frac{G^{\ddagger}_{\beta,MO} - G_{MO*}}{k_B T}\right) \exp\left(-\frac{G_{MO*} - (G_{MO} + G_{H^+})}{k_B T}\right)}{\frac{k_B T}{h} \exp\left(-\frac{G^{\ddagger}_{cond} - (G_{Ac} + G_{Ac*})}{k_B T}\right) \exp\left(-\frac{G_{Ac*} - (G_{Ac} + G_{H^+})}{k_B T}\right)} \quad (17)$$

Here, the $G_i^{\ddagger}$-terms represent the free energy of the transition state (i = *β*,*MO* and *cond* denoting, respectively, β-scission of MO and acetone condensation), G_j-terms represent the free energy of gaseous species (j = *MO* and *Ac* denoting MO and acetone, respectively), and G_{H^+} represents the free energy of the bare Brønsted acid site (all elementary steps are shown in Scheme 3). This equation can be simplified by combining exponents to give:

$$\beta_{MO} = \exp\left(-\frac{\Delta\Delta G_{\beta,MO}}{k_B T}\right) \quad (18)$$

where $\Delta\Delta G_{\beta,MO}$ is the difference in free energy barrier and is given by:

$$\Delta\Delta G_{\beta,MO} = \left(G^{\ddagger}_{\beta,MO} - (G_{MO} + G_{H^+})\right) - \left(G^{\ddagger}_{cond} - (2G_{Ac} + G_{H^+})\right) \quad (19)$$

Similarly, the lumped parameter describing the β-scission of DA (β_{DA}) also reflects a difference in free energy barriers ($\Delta\Delta G_{\beta,DA}$):

$$\beta_{DA} \equiv \frac{k_{\beta,DA} K_{MO}}{k_{cond} K_{Ac} K_{C_6}} = \exp\left(-\frac{\Delta\Delta G_{\beta,DA}}{k_B T}\right) \quad (20)$$

and $\Delta\Delta G_{\beta,DA}$ is given by:

$$\Delta\Delta G_{\beta,DA} = \left(G^{\ddagger}_{\beta,DA} - \left(G_{MO} + G_{H_2O} + G_{H^+}\right)\right) - \left(G^{\ddagger}_{cond} - (2G_{Ac} + G_{H^+})\right) \quad (21)$$

where the elementary steps that are represented by the rate constants (Eq. 20) and free energies (Eq, 21) are shown in Scheme 3. The notable difference between Equations 19 and 21 is the free energy of gaseous H_2O (G_{H_2O}; present in Eq. 21) representing that H_2O is required for the DA β-scission. Here, we also explicitly include the free energy of the bare site (G_{H^+}) for the reactions because in the current interpretation the proton is the only active site (Scheme 3) but other possible active sites will be discussed in Sections 3.3.4 and 3.3.5. These representations of the relevant energies also show that the identity of the reactive species can only be described as the quasi-equilibrated pool of C_6-species; the only conclusion is the involvement of H_2O in the β-scission species.

Measured $(Ac)^2/(MO)$ values increased linearly with increasing H_2O pressure on MFI-3 and BEA (Fig. 9), consistent with the derived pseudo-steady state MO pressure dependence (Eq. 15). Regressed linear fits of these data to the form of Equation 15 result in β_{DA} values (slope) of 260 $\pm$ 20 and 190 $\pm$ 40 for MFI-3 and BEA, respectively, and β_{MO} values (intercept) of 24.5 $\pm$ 0.4 bar and 8.2 $\pm$ 0.9 bar for MFI-3 and BEA, respectively (Table 2). These β_{MO} values, which are significantly greater than zero, are consistent with isobutene formation during acetone condensation without added H_2O presented in Section 3.3.1 occurring via β-scission of a MO species (Eq. 9). The increased production of isobutene from MO (denoted by lighter gray shading (Dry); Fig. 9) compared to DA (denoted by darker gray shading (Wet); Fig. 9) at low H_2O pressures reflects the low equilibrium concentrations of DA compared to mesityl oxide and H_2O, which is consistent with coupled cluster (CCSD, AUG-cc-pVDZ, 473 K) estimations of the free energies of these gaseous species (ΔG = 41 kJ mol^{-1}; Scheme 1).

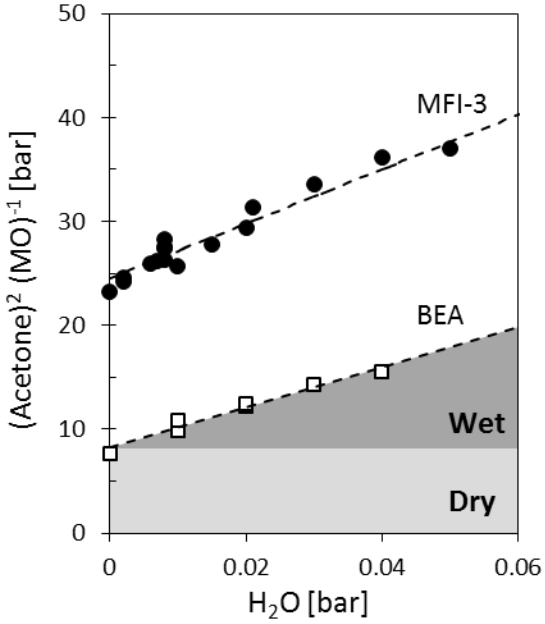

Figure 9: $(Ac)^2/(MO)$ values as a function of H_2O pressure on MFI-3 and BEA (473K, 0.5-2 kPa acetone, 0-6 kPa H_2O). Dashed lines represent regressed linear fits of data to the form of Eq. 15, and the lighter and darker shaded regions denote contributions of the MO β-scission (Dry) and DA β-scission (Wet), respectively, to the measured $(Ac)^2/(MO)$ values.

Table 2: Acetone condensation rate constants (k_{cond}; Eq. 1) and β-terms describing MO (β_{MO}; Eq. 9) and DA (β_{DA}; Eq. 20) β-scission pathways [a]

Zeolite	k_{cond} [b]	$\boldsymbol{\beta_{MO}}$		$\boldsymbol{\beta_{DA}}$ [d]
	$(H^+ \text{ s bar})^{-1}$	bar	bar	unitless
MFI-1	0.34 ± 0.06	2.2 ± 0.8 [c]	3 ± 1 [d]	240 ± 30
MFI-2	0.37 ± 0.02	7 ± 1 [c]	--	--
MFI-3	0.36 ± 0.04	10.0 ± 0.5 [c]	12.3 ± 0.2 [d]	260 ± 20
MFI-4	0.38 ± 0.02	37 ± 2 [c]	35 ± 3 [d]	280 ± 70
BEA	1.14 ± 0.04	6 ± 1 [c]	8.2 ± 0.9 [d]	190 ± 40
FER	0.013 ± 0.003	1.8 ± 0.3 [c]	--	--
TON	0.04 ± 0.02	1.8 ± 0.4 [c]	--	--
MCM-41	0.16 ± 0.01	0.50 ± 0.08 [c]	--	--

[a] Uncertainties represent 95% confidence interval of the fitted values.
[b] First-order acetone condensation rate constant reported previously (Chapter 2).
[c] Parameter determined by regressed linear fit of data to the form of Eq. 10 (data shown in Figs. 5, 6a, and 10).
[d] Parameters determined by regressed linear fit of data to the form of Eq. 15 (data shown in Figs. 9 and 11).

The mechanistic analysis presented here shows that C_4 formation from acetone occurs via subsequent reactions of C_6 condensation products and that there are two distinct pathways: MO β-scission of MO (MO species shown in Scheme 1) and DA β-scission (possibly in the form of DA, but these are not distinguishable from any pathway involving MO and H_2O as shown in Eq. 21). We also found that the addition of gaseous H_2O (H_2O/acetone molar ratios ≤ 3) at these reaction conditions (473 K) decreased deactivation rates by increasing C_4 selectivity. Further mechanistic details and plausible implications of unstable intermediates require an understanding of the possibility of intracrystal C_6 concentration gradients affecting product selectivity, where the proton density and crystal size of the aluminosilicate dictate the ability of these species to diffuse to and from active sites. Here, we have shown results for one MFI sample of a certain crystal size and proton density (Table 1), but in the next section we will extend this analysis to MFI samples of different proton densities.

3.3.4 Effect of proton density on isobutene selectivity

Measured C_4/MO molar ratios increased proportionally with increasing χ -values (Fig. 10) measured over a range of acetone pressure (0.2-4 kPa) on MFI samples of different proton densities (0.070 - 0.62 mmol $H^+/g_{zeolite}$; Table 1); such dependencies are consistent with the mechanistic interpretations used in the derivation of Equation 10. The apparent increase in the slopes (β_{MO}; Table 2) of these linear dependencies with decreasing proton density (Fig. 10) is unexpected given the mechanism shown in Scheme 3, where protons are the active site for condensation and β-scission reactions. Such a mechanism (Scheme 3) would be consistent with β_{MO} values that are independent of proton densities or that increase with increasing proton density due to diffusion-enhanced secondary reactions of MO. Our previous study of these samples showed that gradients

in acetone or MO concentrations do not exist at these conditions (Chapter 2). Similar measured condensation rate constants (per proton; k_{cond}, Table 2) on these MFI samples reflected similar acetone concentrations at all proton locations (Chapter 2), and nearly complete selectivity toward the saturated C_6-alkanone (methyl isobutyl ketone) when extracrystalline Pt/SiO_2 was present suggested that MO diffuses out of MFI crystals without undergoing subsequent reactions (Chapter 2). Here, differences in β_{MO} values among MFI samples reflect changes in the pseudo steady-state pressure of MO because condensation turnover rates are constant among these MFI samples (Table 2). Changes in the pseudo-steady state pressure of MO due to proton densities of MFI samples requires changes in the pressure of acetone or H_2O (Eq. 14), which contradicts our previous findings referred to above, assuming H_2O diffuses more rapidly than MO.

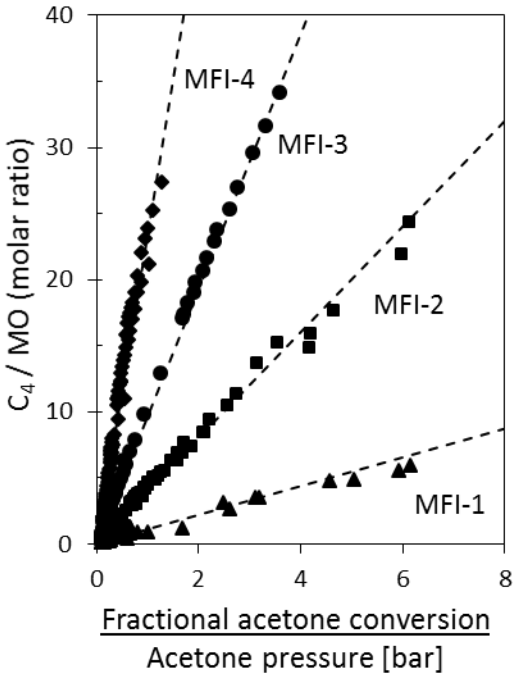

Figure 10: C_4/MO molar ratios as a function of acetone conversion divided by acetone pressure (χ, Eq. 11) on MFI-1 (triangles), MFI-2 (squares), MFI-3 (circles), and MFI-4 (diamonds) with H^+/g values of 0.62, 0.42, 0.38, and 0.07, respectively (Table 1). (473 K, 0.2-4 kPa acetone). Dashed lines are regressed linear fits of the data to the form of Eq. 10.

$(Ac)^2/(MO)$ values measured on MFI samples of different proton density (MFI-1, MFI-3, MFI-4) increased linearly with increasing H_2O pressures (Fig. 11) consistent with Equation 15. β_{DA} values (Eq. 17), the slopes of these linear dependencies, were similar (Table 2), which, taken together with the similar condensation rate constants among these MFI samples (k_{cond}; Table 2), are consistent with the DA β-scission pathway occurring exclusively on protons. The similarity of β_{DA} values also suggests that all protons in these MFI samples experience a similar concentrations of the relevant species for DA β-scission. β_{MO} values increased with decreasing proton densities of MFI samples (Table 2) reflecting the same dependence shown by the slopes of the curves in Figure 10. The similar magnitudes of β_{MO} values determined from data in Figures 10 and 11 suggests that acetone condensation measurements without co-fed H_2O accurately assess β_{MO}, verifying the conclusions of Section 3.3.1 (Eq. 12).

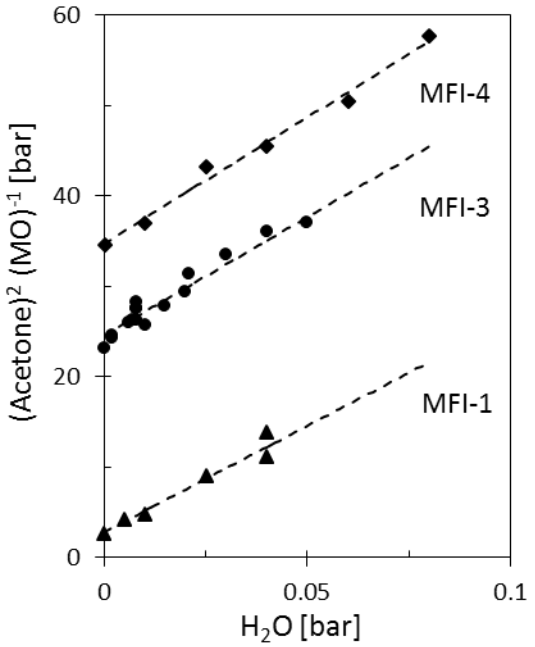

Figure 11: $(Ac)^2/(MO)$ values as a function of H_2O pressure on MFI-1, MFI-3, and MFI-4 (473K, 0.5-2 kPa acetone, 0-7.5 kPa H_2O). Dashed lines represent regressed linear fits of data to the form of Eq. 15.

β_{MO} values reflect free energies of transition states that mediate acetone condensation and MO β-scission, gaseous precursors, and the bare sites that catalyze these reactions (Eq. 19). Measured condensation rate constants are similar among these MFI samples (k_{cond}, Table 2); thus, differences in β_{MO} values are attributed to differences in free energies of MO β-scission transition states or differences in the sites responsible for condensation and β-scission. The latter suggests that the rate constants for MO β-scission are not properly normalized by the number of active sites present in each MFI sample in the analysis above; such normalizations yields:

$$\beta_{MO} = \frac{k_{\beta,MO} K_{MO}}{k_{cond} K_{Ac}} \left(\frac{H^+}{L_2}\right) \tag{22}$$

The temperature dependence of the β_{MO} values measured on these MFI samples of different proton densities could provide insight into the mechanism for this β-scission pathway and plausible active sites in these samples. β_{MO} values depend on reaction temperature as shown in Equation 18. The difference in free energy barriers (ΔΔG) in Equation 16 can be expressed in terms of enthalpic (ΔΔH) and entropic (ΔΔS) contributions [39, 40]:

$$\beta_{MO} = \left(\frac{H^+}{L_2}\right) \exp\left(-\frac{\Delta\Delta H_{\beta,MO} - T\Delta\Delta S_{\beta,MO}}{k_B T}\right) \tag{23}$$

Linearization of Equation 23 as a function of (T)-1 yields:

$$\ln(\beta_{MO}) = \frac{-\Delta\Delta H_{\beta,MO}}{k_B}\frac{1}{T} + \frac{\Delta\Delta S_{\beta,MO}}{k_B} + \ln\left(\frac{H^+}{L_2}\right) \tag{24}$$

The dependencies of β_{MO} values measured over a range of reaction temperatures on MFI samples (453-483 K; MFI-2, MFI-3, MFI-4; Fig. 12) are consistent with the form of Equation 24. Regressions of these data show that the enthalpic terms among MFI samples are similar (Table 3) suggesting similar MO β-scission pathways and a similar site responsible in each of these samples. Thus, differences in β_{MO} values on these samples with different proton density are attributed to an active site different than the protons.

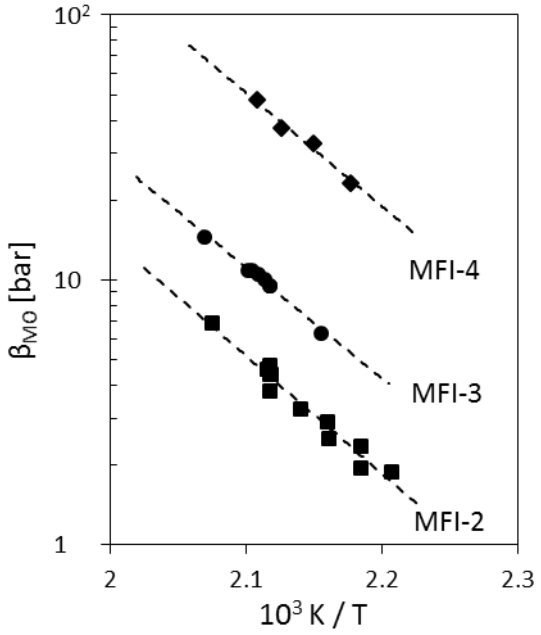

Figure 12: Effect of reaction temperature on β_{MO}-values measured on MFI-2 (squares), MFI-3 (circles), and MFI-4 (diamonds) (453-483 K, 0.3-0.6 kPa acetone). Dashed lines are regressed linear fits of the data to the form of Eq. 24.

Table 3: Enthalpic terms (ΔΔH; Eq. 17) for MFI samples

Zeolite	ΔΔH* (kJ mol^{-1})
MFI-2	88 ± 12
MFI-3	76 ± 11
MFI-4	81 ± 15

*Uncertainty denotes the 95% confidence interval from regressed fits of the data in Figure 12 to the form of Eq. 24.

The effects of H_2O pressure and reaction temperature on C_4 selectivities of MFI samples of varying proton densities suggest that C_4 formation occurs via two distinct reaction pathways on these aluminosilicates. The primary pathway for C_4 formation at dry conditions (0 kPa H_2O added) occurs on a site that depends on acetone pressure (similar to protons) and deactivates at rates similar to protons during acetone condensation. β_{MO} values for MFI samples of varying proton densities are not consistent with reactions occurring on protons, non-framework Al sites (Table 1),

silanols, or active sites present after the catalyst bed (SI, Section 3.6.2), but instead these β_{MO} values suggest that β-scission of MO is proportional microporous volume as shown from β_{MO} values multiplied by proton density that are constant across all MFI samples (Fig. 13).

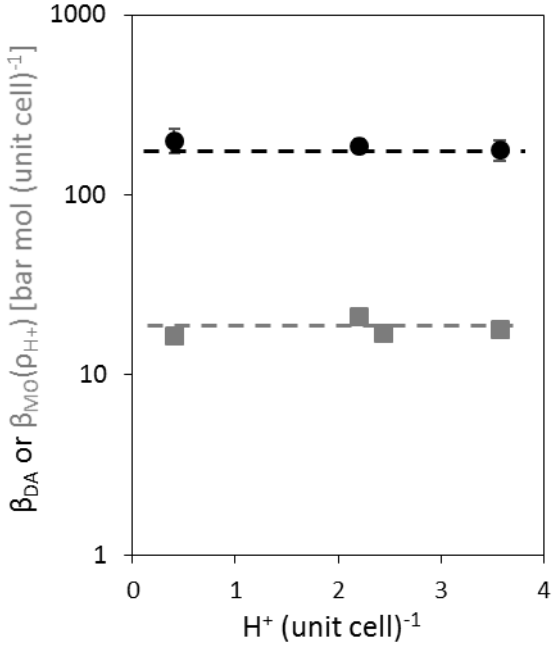

Figure 13: Collections of rate constants for DA β-scission (β_{DA}, black circles; Eq. 20) and the product of MO β-scission rate constants and proton density ($\beta_{MO}\rho_{H+}$, gray squares; Eq. 12) as a function of proton density measured on MFI-[1-4] samples (473K, 0.5-2 kPa acetone, 0-7.5 kPa H_2O). Dashed horizontal lines represent the average values for the data sets.

The addition of microporous volume, in the form of silicate MFI crystals (SIL-1), mixed with MFI-2 crystals, however, did not have a significant effect on the condensation selectivity (Fig. 14; β_{MO} = 7.1-7.6 bar). These data are also consistent with the requirement that the site responsible for MO β-scission must be proximate (within the same crystal) to protons, which was discussed in Section 3.3.1. This requirement of the immediate proximity of protons and the sites catalyzing MO β-scission implicates the formation of very reactive intermediates on protons that undergo β-scission before egressing from the MFI crystal, and thus, precluding the β-scission of MO-species that are present in measurable amounts (mesityl oxide and isomesityl oxide; Scheme 1). Such requirements are consistent with a MO-enol species (Scheme 1) as the MO intermediate as a precursor for β-scission reactions.

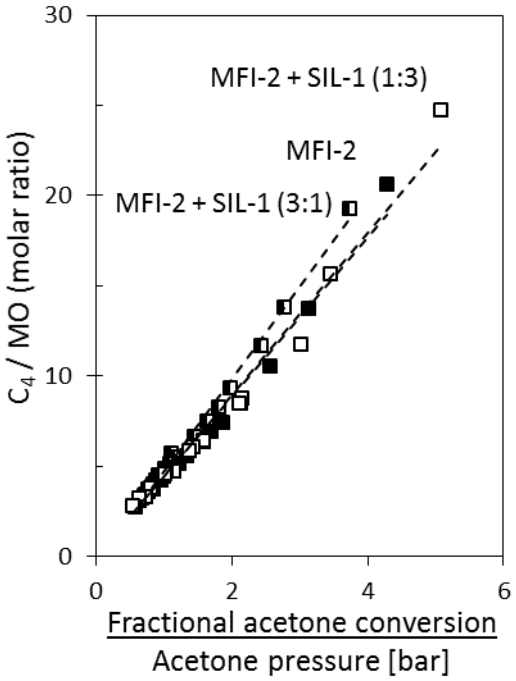

Figure 14: Effect of acetone conversion divided by acetone pressure (χ, Eq. 11) on C_4/MO molar ratio measured on MFI-2 (filled squares), MFI-2 + SIL-1 (1:3 mass ratio; open squares), and MFI-2 + SIL-1 (3:1 mass ratio; half-filled squares). (473 K, 1.0 kPa acetone). Dashed lines are regressed linear fits of the data to the form of Eq. 10.

These data, collected on MFI samples of different proton densities, require that MO β-scission, the dominant reaction pathway leading to C_4 formation at dry conditions (0 kPa H_2O added), occurs on a site present in the MFI crystals that is proportional to both the mass of the zeolite and the number of protons (Fig. 13). Such a dependence cannot be explained by bifunctional mechanisms and is indicative of free-radical reaction pathways, where initiation and propagation occur on separate sites, and the resulting rate is proportional to the product of the two sites. Free-radical reaction pathways and the plausibility of their participation in MO β-scission are the subjects of Section 3.3.5.

3.3.5 Implications of free radical β-scission of C6-alkenone intermediates within confining voids

C_4 selectivity increasing with decreasing zeolite proton density (increasing Si/Al ratio) has been reported previously during acetone condensation on FAU [18] and MFI [7, 8]; these studies, however, do not present mechanistic explanations for this counterintuitive C_4 selectivity trend. The mechanistic details concluded from the rate and selectivity data, presented in Sections 3.3.1-3.3.4, preclude non-framework Al sites, silanols (Si-OH), and active sites outside of the catalyst bed from contributing to C_4 formation. The conclusions from these data, however, are consistent with the rate of MO β-scission occurring on active sites that are present at amounts proportional to the volume (or mass) of the zeolite present (Fig. 13) and are within crystals where protons are present (Fig. 14). These assessments narrow the plausible mechanistic explanations to a radical-catalyzed mechanism, where protons facilitate the formation of unstable MO intermediates that either

decompose (initiation; Scheme 4) or react with a radical (propagation; Scheme 5) in the confining environment; such mechanisms would depend on both the protons and the confining void.

Scheme 4: Decomposition of C_6-alkenone (initiation of radical pathways)* [41, 42]

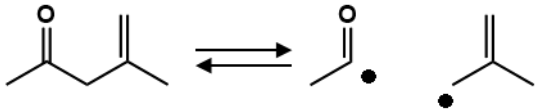

$$\Delta G = 188 \text{ kJ mol}^{-1}$$

* Difference in Gibbs free energy of gaseous species in forward direction (473 K, CCSD, AUG-cc-pVDZ; discussed in Section 3.2.3). Location of the unpaired electron is denoted with a black circle.

Radical decomposition of alkanones occur via homolytic cleavage of the C-C bond between the carbonyl-C and α-C [41, 42] as shown for isomesityl oxide in Scheme 4. The coupled cluster (CCSD) estimate of the difference in free energy between gaseous isomesityl oxide and gaseous radical species (isobutene and acyl radicals) is provided in Scheme 4 (ΔG = 188 kJ mol^{-1}; CCSD, AUG-cc-pVDZ); this CCSD-estimate, taken together with DFT-estimates of the activation barrier (Chapter 2), suggests that gas-phase decomposition of isomesityl oxide would pose a barrier of at least 290 kJ mol^{-1} (barrier from H-bonded acetone and gaseous acetone). This barrier is 170 kJ mol^{-1} greater than the estimated kinetically-relevant barrier for acetone condensation (120 kJ mol^{-1}; Chapter 2); the large barrier for decomposition would be attenuated by the additional stabilization of the radical species via van der Waals stabilization interactions with the walls of the confining voids, which were signification in determining the barrier for condensation (Chapter 2). The barrier for decomposition of isomesityl oxide is extremely large, suggesting that the decomposition of another species is responsible for initiating the radical chain, an event that occurs infrequently compared to the occurrence of propagation during radical chain reactions. Thus, radical propagation requires a reactive C_6 species formed on protons.

The radicals formed in the initiation steps can propagate the radical chain-reaction by abstracting a H-atom from a C_6-alkenone or C_6-alkenol, which results in the formation of a C_6-radical. Relative stabilities of gaseous C_6-radicals and the H-atom abstraction pathways to form these radicals are shown in Scheme 5 (473 K, CCSD, AUG-cc-pVDZ). Once formed, these radicals can undergo β-scission reactions (Scheme 6), which cleave C-C bonds at the β-position to the radical forming an unsaturated molecule and a new radical. β-scission reactions of C_6 radicals with the unpaired electron at the acyl C-atom form ketene, which can react with H_2O to form acetic acid (a measured product), and a C_4 radical.

Scheme 5: Relative stabilities of C_6 radicals and H-atom abstraction events that forms C_6 radicals*

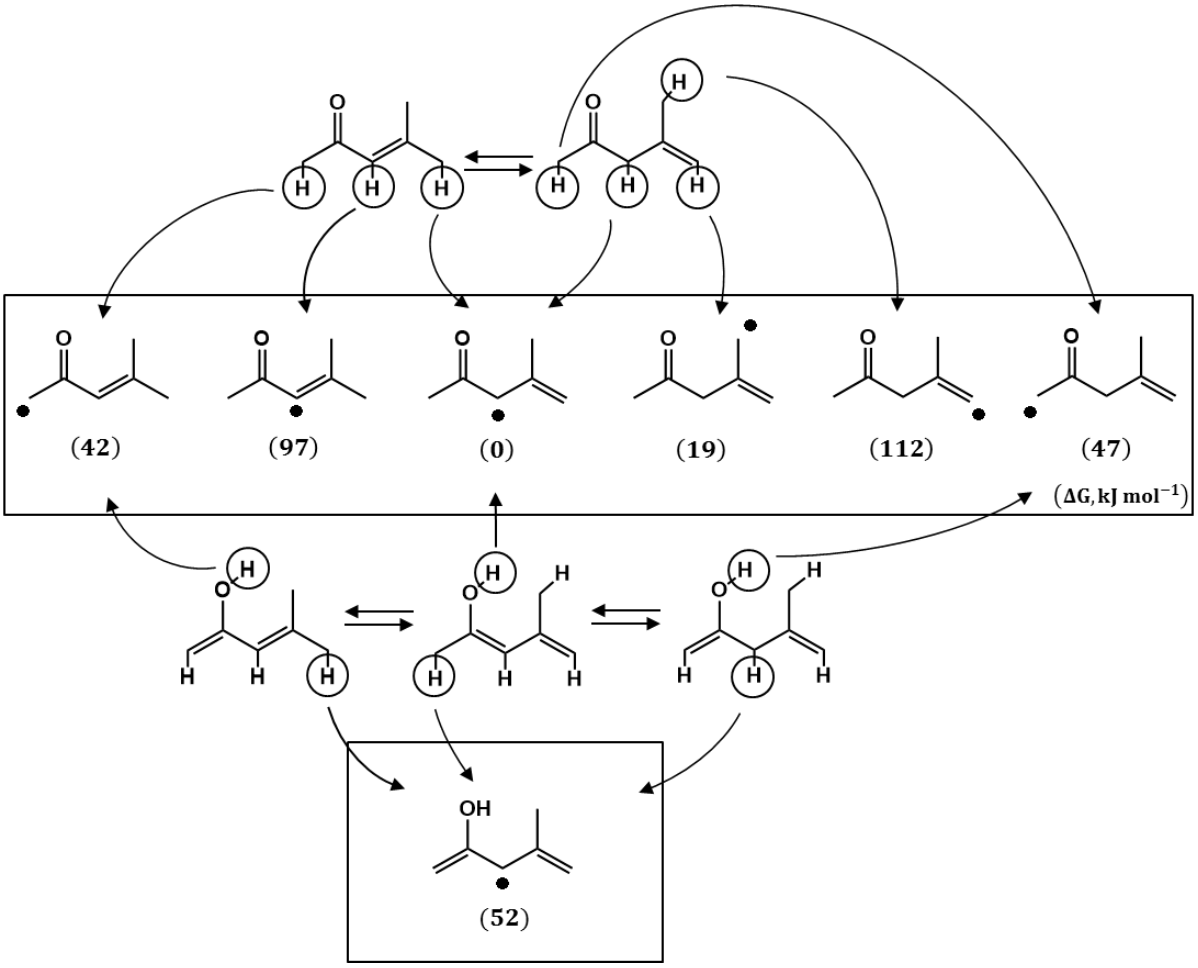

*Gibbs free energy differences between gaseous species and most stable radical are provided in parenthesis (473 K, CCSD, AUG-cc-pVDZ; discussed in Section 3.2.3). Location of the unpaired electron is denoted with a black circle. Open circles and arrows indicate with H-atom is abstracted from the C_6 species to form each radical. Only distinct H-atoms of each C_6 molecule are explicitly shown.

Scheme 6: β-scission of radical species (propagation of radical pathways)* [43]

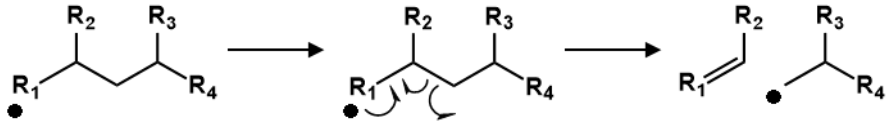

* Location of the unpaired electron is denoted with a black circle. Curved arrows indicate movement of each electron involved in β-scission.

The radical chain reaction mechanism proposed here (Scheme 7) is initiated by the radical decomposition of an unidentified species which abstracts a H-atom from a C_6-enol. The C_6 enol radical has the unpaired electron at the C-atom of the acyl moiety and undergoes β-scission forming a C_4 radical. C_6 and C_4 radicals continue to propagate the radical chain consuming C_6

species and forming C4 and acetic acid, as shown in Scheme 7. The C_6 enol species involved in propagation are formed on protons, and the proximate presences of protons replenishes this reactive C_6 enol intermediate explaining the requirement of protons at a close proximity. Radical termination occurs when two radicals collided and form a C-C bond (similar to the reverse reaction in Scheme 4), which occurs infrequently in the limit of the long-chain approximation [44]. This reaction pathway is reminiscent of the classic Rice-Herzfeld radical mechanism [45].

Similar proposals to Scheme 7 have been reported for the thermal decomposition of mesityl oxide at elevated temperatures (685-763 K) [19], consistent with the ability of oxygenates to form free radical species [41, 42, 46]. These thermal decomposition pathways require temperatures much higher than those used in this study (453-483 K), however, this can be explained by: (i) the presence of protons, which convert mesityl oxide into more reactive MO isomers (Scheme 1), and (ii) the confining voids, which provide van der Waals contacts stabilizing transition states that mediate free radical decomposition and propagation steps. Confining voids, without the presence of protons, have also been show to catalyze reactions at temperatures much lower than those required for the analogous gas-phase reaction by stabilizing transition states similar in size and shape to the confining void [21].

Scheme 7: Plausible elementary steps for the formation of isobutene and acetic acid from MO via acid-catalyzed and free radical reactions*

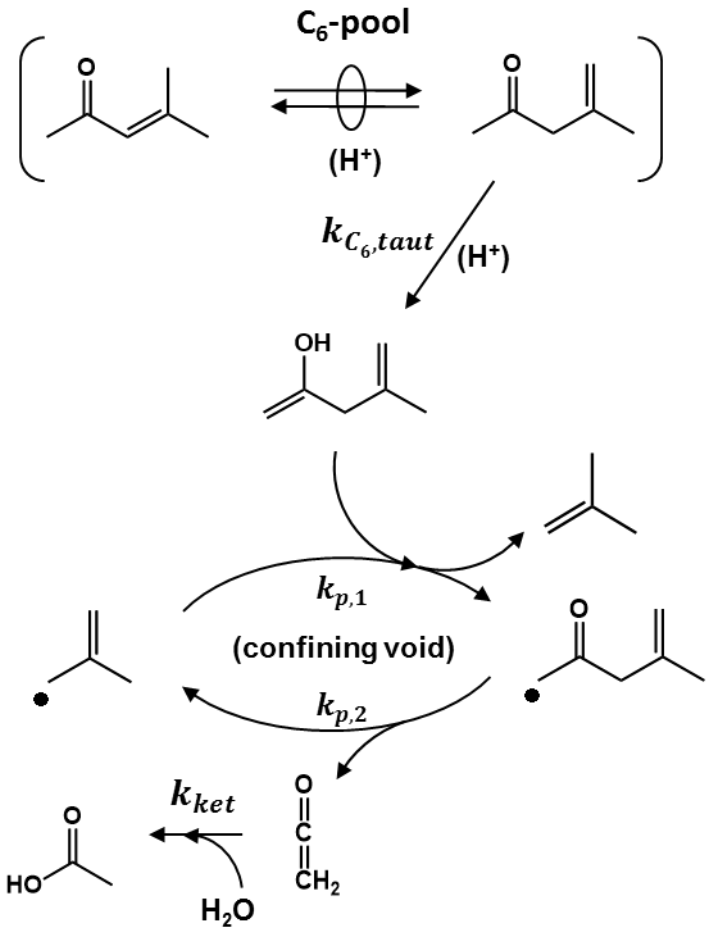

k_X denotes kinetic constants for forward steps. Quasi-equilibrated steps are indicated by a circle over the double arrows. Equilibrated double-bond isomers (Scheme 1) are indicated by dotted lines for double bonds (MO). Location of the unpaired electron is denoted with a black circle.

Such radical propagation pathways are shown on a reaction coordinate diagram (Fig. 15), where each state is represented by the free energies of the species present (473 K, CCSD, Gaussian 09, AUG-cc-pVDZ). Figure 15 does not provide the energies of the transition states that mediate radical propagation; although radical pathways generally have negligible activation barriers beyond the difference in thermodynamic stability between the reactant and product states (these energy difference are shown in Fig. 15). The theoretical treatments presented here are consistent with the formation of an unstable C_6 species, which is incorporated into radical propagation ultimately forming isobutene and acetic acid. The relative free energy barrier for propagation compared to condensation (Chapter 2) is 23 kJ mol^{-1} (Fig. 15), which could be compensated by the van der Waals interactions with the confining framework that where not incorporated in these calculations for the radical propagation.

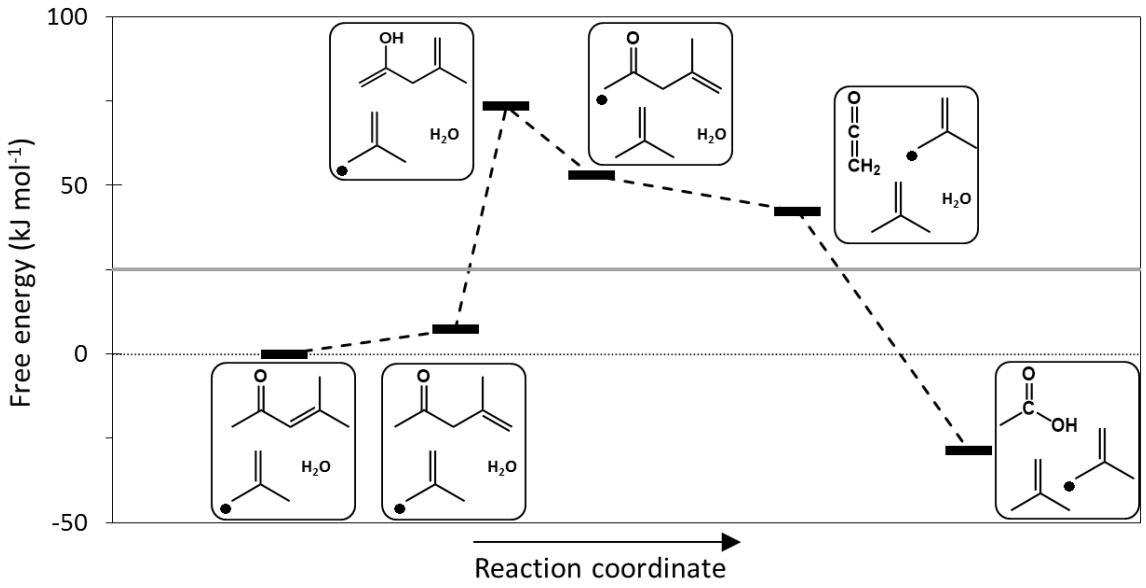

Figure 15: Gibbs free energy diagram for gaseous radical propagation at 473 K and standard pressure (1 bar) for all gaseous species calculated by CCSD, Gaussian 09, AUG-cc-pVDZ (methods are described in Section 3.2.3). Location of the unpaired electron is denoted with a black circle. Horizontal gray line represents the free energy barrier required for acetone condensation relative to the species in the left-most box.

3.4 Conclusions

In this study, the elementary steps for acetone conversions into isobutene (C_4) and acetic acid on solid Brønsted acid catalysts were identified by the combination of detailed kinetic measurements, rigorous mechanistic interpretations of rates and selectivities on a series of aluminosilicates, and theoretical calculations of reactive intermediates and radical species. These mechanistic assessments provided insights that C_6 species are present at pseudo steady state concentrations during catalysis at these conditions; such conclusions allow rigorous comparisons of C_4 selectivities, as C_4/MO molar ratios, on a range of aluminosilicates accounting for the effects of acetone conversion and acetone pressure. Here, we also show that C_4 species are derived from the β-scission of C_6-species, present as a quasi-equilibrated pool; these reaction pathways form equimolar amounts of C_4 and acetic acid. We also investigated catalyst selectivity toward further condensation pathways, which form precursors of catalyst deactivation also derived from the C_6-pool. The addition of gaseous H_2O to the reactant stream for condensation decreases catalyst deactivation by decreasing the concentration of the C_6-pool and also reveals two β-scission pathways from the C_6-pool that are distinguishable by H_2O dependence, which establishes the equilibrium concentrations of ketol and alkenone species. One pathway is the β-scission of the ketol species catalyzed exclusively by protons. The other β-scission pathway, however, is the predominate reaction pathway in dry conditions (0 kPa H_2O added), and somewhat unexpectedly C_4 selectivity (subsequent product) increased with decreasing proton density (active site) due to this pathway. The dependence of C_4 selectivities on proton density, H_2O pressure, and reaction temperature can only be explained by free-radical β-scission reactions of C_6-species, where a

nearby acid site catalyzes the formation of reactive C_6 species that undergo radical propagation steps within the microporous void environment of the framework. This proposed radical propagation pathway is supported by previous reports of radical oxygenate species and theoretical calculations (CCSD) described here.

3.5 Acknowledgements

The authors acknowledge the financial support of BP, p.l.c. for this work as part of the BP Conversion Consortium (BP-XC^2); the technical discussions with Drs. John Shabaker and Glenn Sunley (BP, p.l.c.) and Dr. Shuai Wang and Michele Sarazen (University of California, Berkeley); and Dr. Raul Lobo (University of Delaware) and Drs. Nancy Artioli and Xiaoqin Zou (University of California, Berkeley) for the synthesis of the SIL-1 samples used. Computational facilities were provided by the Extreme Science and Engineering Discovery Environment (XSEDE), which is supported by the National Science Foundation (grant number: CHE-140066).

3.6 Supporting Information

3.6.1 Derivation of expression for catalyst deactivation during acetone condensation

Deactivation is interpreted as the blocking of active sites by large, unsaturated species, which renders these sites catalytically-inactive. Here, we operate at low acetone conversions ($\leq$ 10%) suggesting that large products are formed via subsequent condensation reactions of products. Condensation rates of MO and acetone (r_{C9}) are described by the rate expression (Eq. 7):

$$\frac{r_{C_9}}{[H^+]} = \frac{k_{cond,C_9}(\mathrm{Ac})K_{MO}(\mathrm{MO})}{K_{Ac}(\mathrm{Ac})} \tag{S1}$$

where the kinetic and thermodynamic constants (k_x and K_X, respectively) are defined in Scheme 3.

Equation S1 describes the formation rate of species implicated as precursors of deactivation and thus can be defined as the change of active protons with time on stream:

$$\frac{r_{C_9}}{[H^+]} = -\alpha \frac{1}{H^+}\frac{d(H^+)}{dt} \tag{S2}$$

where α is a collection of kinetic and thermodynamic constants representing the elementary steps required for C_9-species to block protons.

Substituting Equation S1 into Equation S2 yields:

$$\frac{k_{cond,C_9}K_{MO}}{K_{Ac}}(\mathrm{MO}) = -\alpha \frac{1}{H^+}\frac{d(H^+)}{dt} \tag{S3}$$

MO is present at pseudo steady-state during reaction conditions, and therefore the concentration of MO is constant with time. Integration of Equation of S3 results in the expression for the fraction of active protons are remaining at time t:

$$\frac{(H^+)|_{t=t}}{(H^+)|_{t=0}} = \exp\left(-\frac{k_{cond,C_9}K_{MO}}{\alpha K_{Ac}}(\mathrm{MO})t\right) \tag{S3}$$

The fraction of active protons remaining is reflected by the time dependence of the measured condensation rate (r_{cond}).

$$\frac{r_{\mathrm{cond}}(t)}{r_{\mathrm{cond}}(0)} = \exp(-k_d(\mathrm{MO})t) \tag{S3}$$

where k_d represents the rate constant for deactivation present in Equation 12.

3.6.2 Plausible active sites that catalyze β-scission of MO

Here, we investigate plausible active sites in zeolite crystals for the β-scission of MO with the requirement that the number of the specified active site is proportional to catalyst mass (as shown in Section 3.3.4).

1) Non-framework Al

Non-framework Al-atoms are Lewis acid centers and have been implicated as active sites for aldol condensation in zeolites (Chapter 2). The number of these sites present in each sample is determined by the difference of the number of protons from the total number of Al in each sample (Table 1). The MFI samples with different proton densities have non-framework Al contents of 0.33, 0.13, 0, and 0.03 mmol non-framework Al/$g_{zeolite}$ for MFI-1, MFI-2, MFI-3, and MFI-4, respectively. Thus, non-framework Al content also decreases with decreasing proton density and therefore also cannot be the active site for the β-scission of MO. Also, the non-framework Al content for MFI-3 is zero, which is not consistent with non-framework Al sites producing the measured C_4 selectivities on this sample.

2) Silanol sites

Experiments were performed where mesityl oxide and H_2O where fed over SIL-1 (Si-MFI) samples with silanol defects and C_4 products were not measured (473 K, 0.1 kPa mesityl oxide, 0.1 kPa H_2O). This suggests that either silanols present are not able to catalyze the β-scission of MO or these reaction pathways require protons to form intermediates that undergo β-scission reactions.

3) Potential active sites present after the catalyst bed

Experiments were performed with a stacked bed where Pt/SiO_2 (2% wt Pt; ~0.030 mg) was loaded first, then amorphous SiO_2 (~0.060 mg), followed by MFI-2 (~0.030 mg) creating a stacked bed. This stacked bed allowed measurements reaction rates and selectivities on the MFI-2, where products were hydrogenated (27 kPa H_2) immediately after the catalyst bed, forming stable saturated products. Rates and C_4 selectivities were similar with and without Pt present after the catalyst bed, precluding significant C_4 formation in the transfer lines (316 stainless steel, ~423 K) or analysis equipment (Agilent GC 6890).

3.7 References

1. Kubička, D. and O. Kikhtyanin, *Opportunities for zeolites in biomass upgrading-Lessons from the refining and petrochemical industry.* Catalysis Today, 2015. **243**: p. 10-22.
2. Sun, J. and Y. Wang, *Recent Advances in Catalytic Conversion of Ethanol to Chemicals.* ACS Catalysis, 2014. **4**(4): p. 369-453.
3. Sheldon, R.A., *Green and sustainable manufacture of chemicals from biomass: state of the art.* Green Chemistry, 2014. **16**(3): p. 950-963.
4. Demorest, M., D. Mooberry, and J.D. Danforth, *Decomposition of Ketones and Fatty Acids by Silica-Alumina Composites.* Industrial & Engineering Chemistry Research, 1951. **43**(11): p. 2569-2572.
5. Shuikin, A.N., et al., *Conversion of Acetone to Isobutylene on a Silica-Tungsten Catalyst.* Petroleum Chemistry U.S.S.R., 1977. **17**(3): p. 173-180.
6. Hutchings, G., et al., *Acetone conversion to isobutene in high selectivity using zeolite β catalyst.* Catalysis letters, 1993. **21**(1-2): p. 49-53.
7. Kubelková, L., et al., *Acetone Conversion and Deactivation of Zeolites*, in *Studies in Surface Science and Catalysis*, P.A. Jacobs and R.A.v. Santen, Editors. 1989, Elsevier. p. 1203-1212.
8. Cejka, J. and J. Pavel, *Influence of water on activity, selectivity and deactivation of zeolites in acetone transformation.* Collection of Czechoslovak Chemical Communications, 1989. **54**(11): p. 2998-3002.
9. Tago, T., et al., *Selective production of isobutylene from acetone over alkali metal ion-exchanged BEA zeolites.* Catalysis Today, 2011. **164**(1): p. 158-162.
10. Tago, T., et al., *Selective synthesis for light olefins from acetone over ZSM-5 zeolites with nano- and macro-crystal sizes.* Applied Catalysis A: General, 2011. **403**(1-2): p. 183-191.
11. Sarazen, M. and E. Iglesia, *unpublished results*. 2016.
12. Gumidyala, A., T. Sooknoi, and S. Crossley, *Selective ketonization of acetic acid over HZSM-5 : The importance of acyl species and the influence of water.* Journal of Catalysis, 2016. **340**: p. 76-84.
13. Panov, A. and J.J. Fripiat, *An infrared spectroscopic study of acetone and mesityl oxide adsorption on acid catalyst.* Langmuir, 1998. **14**(14): p. 3788-3796.
14. Salvapati, G.S., K.V. Ramanamurty, and M. Janardanarao, *Selective catalytic self-condensation of acetone.* Journal of Molecular Catalysis, 1989. **54**(1): p. 9-30.
15. Chang, C.D. and A.J. Silvestri, *The Conversion of Methanol and Other O-Compounds to Hydrocarbons over Zeolite Catalysts.* Journal of Catalysis, 1977. **259**(47): p. 249-259.
16. McAllister, S., W. Bailey, and C. Bouton, *The Catalyzed Cleavage of Diacetone Alcohol and Other Ketols and Unsaturated Ketones.* Journal of the American Chemical Society, 1940. **62**(11): p. 3210-3215.
17. Panov, A. and J. Fripiat, *Poisoning of aldol condensation reaction with H2O on acid catalysts.* Catalysis letters, 1999. **57**(1-2): p. 25-32.
18. Veloso, C.O., J.L.F. Monteiro, and E.F. Sousa-Aguiar, *Aldol condensation of acetone over alkali cation exchanged zeolites.* Studies in Surface Science and Catalysis, 1994. **84**: p. 1913-1920.
19. Daly, N.J. and M.F. Gilligan, *Thermal Reactions of Mesityl Oxide.* Australian Journal of Chemistry, 1971. **24**(5): p. 955-960.

20. Boekfa, B., et al., *Adsorption and Tautomerization Reaction of Acetone on Acidic Zeolites: The Confinement Effect in Different Types of Zeolites.* The Journal of Physical Chemistry C, 2010. **114**(35): p. 15061-15067.
21. Artioli, N., R.F. Lobo, and E. Iglesia, *Catalysis by confinement: Enthalpic stabilization of NO oxidation transition states by microporororous and mesoporous siliceous materials.* Journal of Physical Chemistry C, 2013. **117**(40): p. 20666-20674.
22. First, E.L., et al., *Computational characterization of zeolite porous networks: an automated approach.* Physical chemistry chemical physics : PCCP, 2011. **13**(38): p. 17339-58.
23. Jones, A.J., et al., *Acid strength and solvation in catalysis by MFI zeolites and effects of the identity, concentration and location of framework heteroatoms.* Journal of Catalysis, 2014. **312**: p. 58-68.
24. Baerlocher, C. and L.B. McCusker. *Database of Zeolite Structures*. February 6, 2016]; Available from: http://www.iza-structure.org/databases/.
25. Cížek, J., *Advances in Chemical Physics*, ed. P.C. Hariharan. Vol. 14. 1969, New York: Wiley Interscience.
26. Purvis, G.D.I. and R.J. Bartlett, *A full coupled-cluster singles and doubles model - the inclusion of disconnected triples.* The Journal of Chemical Physics, 1982. **76**: p. 1910-1918.
27. Scuseria, G.E., C.L. Janssen, and H.F. Schaefer III, *An efficient reformulation of the closed-shell coupled cluster single and double excitation (CCSD) equations.* The Journal of Chemical Physics, 1988. **89**: p. 7382-7387.
28. Scuseria, G.E. and H.F. Schaefer III, *Is coupled cluster singles and doubles (CCSD) more computationally intensive than quadratic configuration-interaction (QCISD)?* The Journal of Chemical Physics, 1989. **90**: p. 3700-3703.
29. Kendall, R.A., T.H. Dunning Jr., and R.J. Harrison, *Electron affinities of the first-row atoms revisited. Systematic basis sets and wave functions.* The Journal of Chemical Physics, 1992. **96**: p. 6796-6806.
30. Dunning Jr., T.H., *Gaussian basis sets for use in correlated molecular calculations. I. The atoms boron through neon and hydrogen.* The Journal of Chemical Physics, 1989. **90**: p. 1007-1023.
31. Woon, D.E. and T.H. Dunning Jr., *Gaussian-basis sets for use in correlated molecular calculations. 3. The atoms aluminum through argon.* The Journal of Chemical Physics, 1993. **98**: p. 1358-1371.
32. Frisch, M.J., et al., *Gaussian 09, Revision D.01*. 2009, Gaussian, Inc.: Wallingford, CT, USA.
33. Zecchina, A., et al., *IR spectroscopy of neutral and ionic hydrogen-bonded complexes formed upon interaction of CH3OH, C2H5OH, (CH3)2O, (C2H5)2O and C4H8O with H-Y, H-ZSM-5 and H-mordenite: comparison with analogous adducts formed on the H-Nafion superacidic membrane.* Journal of the Chemical Society, Faraday Transactions, 1996. **92**(23): p. 4863-4875.
34. Pazé, C., et al., *Acidic properties of H-β zeolite as probed by bases with proton affinity in the 118-204 kcal mol-1 range: A FTIR investigation.* The Journal of Physical Chemistry B, 1997. **101**(24): p. 4740-4751.
35. Levenspiel, O., *Experimental Search for a Simple Rate Equation to Describe Deactivating Porous Catalyst Particles.* Journal of Catalysis, 1972. **25**: p. 265-272.

36. Konno, H., et al., *Characterization and catalytic performance of modified nano-scale ZSM-5 for the acetone-to-olefins reaction.* Applied Catalysis A: General, 2014. **475**: p. 127-133.
37. Masuda, T., et al., *Process for producing isobutylene from acetone*. 2010, Google Patents.
38. Jiru, P., *Catalytic zeolite for acetone conversion to isobutene*. 1986, JIRU P (JIRU-Individual).
39. Eyring, H., *The Activated Complex in Chemical Reactions.* The Journal of Chemical Physics, 1935. **3**(2): p. 107-115.
40. Evans, M.G. and M. Polanyi, *Some applications of the transition state method to the calculation of reaction velocities, especially in solution.* Transactions of the Faraday Society, 1935. **31**: p. 875-894.
41. Gibian, M.J. and R.C. Corley, *Organic Radical-Radical Reactions, Disproportionation vs. Combination.* Chemical Reviews, 1973. **73**(5): p. 441-454.
42. Fischer, H. and H. Paul, *Rate constants for some prototype radical reactions in liquids by kinetic electron spin resonance.* Accounts of Chemical Research, 1987. **20**(5): p. 200-206.
43. Gilbert, K.E. and J.J. Gajewski, *Coal liquefaction model studies: free radical chain decomposition of diphenylpropane, dibenzyl ether, and phenethyl phenyl ether via β-scission reactions.* The Journal of Organic Chemistry, 1982. **47**(25): p. 4899-4902.
44. Gavalas, G.R., *The long chain approximation in free radical reaction systems.* Chemical Engineering Science, 1966. **3**(21): p. 133-141.
45. Rice, F.O. and K.F. Herzfeld, *Thermal decomposition of organic compounds from the standpoint of free radicals. VI. The mechanism of some chain reactions.* Journal of the American Chemical Society, 1934. **56**(4): p. 285-289.
46. Diaz, E., M.E. Sad, and E. Iglesia, *Homogeneous Oxidation Reactions of Propanediols at Low Temperatures.* ChemSusChem, 2010. **3**(9): p. 1063-1070.